

Structural Design and CFD Modelling of a New Type of
Hydrogen Fuel Injector for Internal Combustion Engine
Applications

Elizabeth Overend

Degree of Doctor of Philosophy (PhD)

The University of Edinburgh

2004



This thesis has been composed by the candidate, Elizabeth Overend.

This work is the candidate's own.

This work has not been submitted for any other degree or professional qualification.

Elizabeth Overend

Abstract

Hydrogen gas is known to offer great potential as an alternative IC engine fuel because of its special properties. These same properties, however, lead to challenging engineering problems to achieve safe and effective handling of this fuel. Many researchers have safely operated engines using hydrogen fuel. A critical investigation of their experiences using various fuel induction methods has been made and published performance results of single-cylinder hydrogen research engines have been normalised and presented. It has been shown that the direct injection (DI) method of fuel induction demonstrates consistently higher IMEP than other fuel induction methods. Key problems that these researchers have faced is durability of injector components when metering hydrogen gas, and providing adequate mass flow rate in the short time available for direct injection.

An original approach to hydrogen direct injector design has been taken, combining features of two existing injectors to create a new model to address this shortfall in the state-of-the-art. The design incorporates a steel, annular diaphragm as the open/close device. This design avoids sliding contact between components and exhibits low wear when metering hydrogen fuel. Further, calculated supply pressure, spring force, stress, fatigue and deflection modelling provide a theoretical proof of concept that the design offers a functional solution to the challenge of hydrogen direct injection. Further concept validation has been provided by comprehensively investigating the flow characteristics of the design in relation to published empirical data and compressible flow theory.

Investigation of the possibility of incorporating a pump in the injector unit to provide elevated pressure shows that a minimum of 3.4% of the fuel energy supplied would be required to power hydrogen compression, corresponding to 0.5 bar MEP. Structural analysis of the clamped diaphragm component shows that bending stress would be at least 236 MPa when sufficient deflection is achieved. Material such as spring steel, with a high yield strength and fatigue endurance limit, would need to be used to avoid failure.

CFD analysis of compressible flow models of two commercial injectors shows agreement with published data, indicating the expected linear relationship of mass flow rate to supply pressure in the super-sonic range. A model of a commercial annular plate injector on which the new design is based indicates mass flow rate up to 50% lower than published data, and the model indicates a discharge coefficient of 22%. This is the result of key differences between actual and modelled injector geometries. Good agreement between results of a CFD model of the diaphragm injector geometry and compressible flow theory is obtained. These results show agreement in the relationship between back pressure and shock wave formation, and sub- and super-sonic mass flow rate-pressure relationship. The model suggests that 66 bar supply pressure would be required to achieve the highest design mass flow rate of 23 g/s, and that the discharge coefficient of the new injector design would be 90% under these conditions.

Contents

NOMENCLATURE	iv
1 INTRODUCTION	1
1.1 Project Background and Motivation	1
1.2 Project Objectives and Report Structure	3
2 LITERATURE REVIEW	7
2.1 Carburetion	8
2.1.1 Fuel Carburetion Equipment	8
2.1.2 Engine Performance	9
2.2 Manifold Injection	15
2.2.1 Inlet Manifold Fuel Injection Equipment	15
2.2.2 Engine Performance	22
2.3 Port Injection	29
2.3.1 Inlet Port Injection Equipment	29
2.3.2 Engine Performance	32
2.4 Direct Injection	35
2.4.1 Direct Cylinder Injection Equipment	35
2.4.2 Engine Performance	42
2.5 Induction Method Performance Comparison	48
2.6 Summary and Discussion	52

2.6.1	Hydrogen Fuel Induction Methods	52
2.6.2	Hydrogen Engine Performance	54
3	INJECTOR DESIGN	58
3.1	Design Strategy	59
3.1.1	New Design Approach	59
3.1.2	Hydrogen Compression	63
3.1.3	Injector Flow Area - Pressure Relationship	65
3.2	Design Calculations	68
3.2.1	Diaphragm Deflection and Stress	68
3.2.2	Fatigue	71
3.2.3	Stress Under Pressure - Hoop Stress	73
3.2.4	Stress and Deflection Modelling	73
3.3	Discussion	79
4	CFD MODEL DEVELOPMENT	84
4.1	Model Geometry and Mesh	84
4.1.1	Conical-Seat Injector	85
4.1.2	Annular Plate Injector	87
4.1.3	Diaphragm Injector	89
4.2	Model Parameters	91
4.3	Obtaining a Converged Solution	93
4.4	Discussion	94
5	CFD MODEL ANALYSIS	97
5.1	Compressible Flow Model Validation	98
5.1.1	Published Data	98
5.1.2	Results Analysis	100
5.2	Annular Plate Injector Model and Validation	106

5.2.1	Published Data	106
5.2.2	Results Analysis	109
5.3	New Injector Design and Validation Against Theory	115
5.3.1	Compressible Flow Theory	115
5.3.2	Results Analysis	119
5.4	Discussion	129
5.4.1	Compressible Flow Model Validation	130
5.4.2	Annular Plate Injector Model	131
5.4.3	Diaphragm Injector Model	133
6	CONCLUSIONS	137
6.1	The State of the Art	138
6.2	New Diaphragm Injector Design	140
6.3	Development of CFD Models	143
6.4	CFD Modelling Results	145
6.5	Recommendations for Continued Work	150
	BIBLIOGRAPHY	152
	APPENDICES	157
	A INJECTOR MASS FLOW REQUIREMENT FOR DI	157
	B ANNULAR PLATE DEFLECTION AND STRESS	161
	C DIAPHRAGM INJECTOR DESIGN DRAWINGS	164

Nomenclature

Abbreviations

abs. Absolute

BMEP Brake Mean Effective Pressure (Pa)

BTDC Before Top Dead Centre

BTE Brake Thermal Efficiency

°CA Crank Angle Degrees (°)

CFD Computational Fluid Dynamics

CR Compression Ratio (-)

DI Direct Injection

DPA Delayed Port Admission

EGR Exhaust Gas Recirculation

FEA Finite Element Analysis

FMEP Friction Mean Effective Pressure (Pa)

HP High Pressure

HUCR Highest Useful Compression Ratio

IMEP	Indicated Mean Effective Pressure (Pa)
IVC	Inlet Valve Close
IVO	Inlet Valve Open
LP	Low Pressure
MBT	Maximum Brake Torque
MI	Manifold Injection
NTP	Normal Temperature and Pressure
PI	Port Injection
pred.	Predicted
PWM	Pulse Width Modulation
RNG	Renormalisation Group
TDC	Top Dead Centre
TMI	Timed Manifold Injection
UTS	Ultimate Tensile Strength (Pa)
WOT	Wide Open Throttle

Greek Characters

γ	Ratio of Specific Heats (-)
η	Efficiency (-)
θ	Change in Slope (radians)
λ	Thermal Conductivity (W/m.K)

μ	Viscosity (kg/m.s)
ρ	Density (kg/m ³)
σ	Fuel-Air Ratio (-), Bending Stress (Pa)
ν	Poisson's Ratio (-)
ϕ	Equivalence Ratio (-)

Symbols

a	Outer Radius (m)
A	Area (m ²)
b	Inner Radius (m)
c	Specific Heat (J/kg.K), Sonic Velocity (m/s)
C	Coefficient (%), Plate Constant
D	Plate Constant
E	Modulus of Elasticity (N/m ²)
G	Modulus of Rigidity (N/m ²)
h	Height (m)
L	Load Constant
m	Mass (kg)
\dot{m}	Mass Flow Rate (kg/s)
\tilde{m}	Molecular Weight (kg/kmol)
M	Bending Moment (Nm)

Ma	Mach Number (-)
n	Polytropic Index of Compression (-)
N	Engine Speed (RPM)
p	Pressure (Pa) (gauge unless otherwise stated)
dp/dX	Pressure Gradient (Pa/m)
Q	Heating Value (J/kg), Shear Force (N)
r	Radius (m), Critical Pressure Ratio (-)
R	Gas Constant (J/kg.K)
t	Thickness (m)
T	Temperature (K)
v	Velocity (m/s)
V	Volume (m ³)
w	Uniform Line Load (N/m)
W	Line Force Magnitude (N)
y	Vertical Deflection (m)

Subscripts

b	Back
d	Discharge
ds	Downstream
e	Effective, Exit

g	Geometric
LHV	Lower Heating Value
r	Radial
R	Reference
s	Swept
T	Throat
vol	Volume

Chapter 1

INTRODUCTION

1.1 Project Background and Motivation

It is well known that hydrogen fuel offers significant advantages over conventional fuels for IC engine operation. Predominantly, this is because hydrogen has the potential to offer a sustainable resource, for example by powering electrolysis of water by wind or geothermal power. This would offer a sustainable process because the products of end use of hydrogen would be water only. This concept is illustrated in Figure 1.1. Currently, hydrogen is mostly produced by reforming natural gas, although Iceland has recently built its first refuelling station providing hydrogen produced by electrolysis on a main highway near Reykjavik [1].

Since hydrogen is carbonless and sulphurless, emissions of CO, CO₂, and SO_x are eliminated in the products of combustion. Some HC can be present from burning oil deposits but the levels are negligible compared with HC emissions from conventionally-fuelled engines (see Section 2.2.2). The principal product of hydrogen-air combustion is water, although NO_x emissions remain a concern.

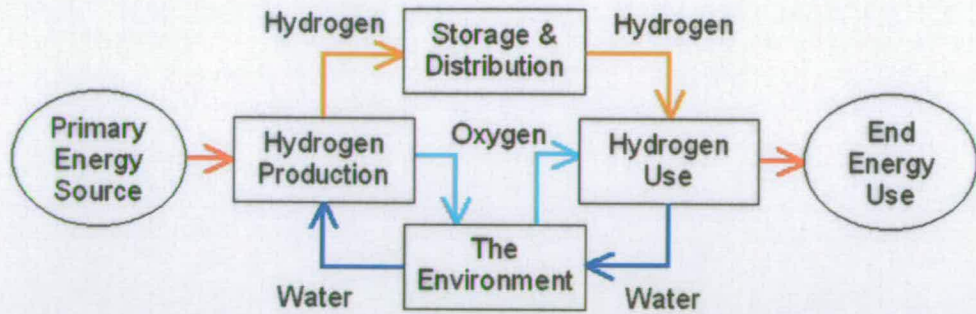


Figure 1.1: Potential of a Sustainable Production-End Use Cycle of Hydrogen

It is clear from these characteristics that hydrogen shows great potential as an alternative fuel for IC engine applications. In the first of two previous studies by the author [2], state-of-the-art research into the surrounding issues facing hydrogen fuel of production and storage has been investigated, along with how the unique properties of hydrogen gas need special attention to achieve optimum engine performance. A second study [3] looked at how these same properties lead to concerns with the safe handling of hydrogen fuel. The same study outlined a design of a safe hydrogen engine testing facility and detailed extensive benchmark tests of a single-cylinder research engine run on petrol fuel for future comparison to hydrogen performance.

Over the past few decades, several research groups have successfully operated IC engines on hydrogen fuel. Broadly, this report builds on the previous work by examining the fuel induction methods employed by previous researchers, and describing their advantages and disadvantages to engine operation. As this study will show, the direct injection fuel induction has the potential to improve engine performance compared to other methods. However, the need to supply high pressure for sufficient fuel delivery and issues of durability of injector components have hampered the efforts of previous researchers.

To address this shortfall in the current state-of-the-art, the general thesis proposed is that a new design of fuel injector, incorporating a steel annular diaphragm as the open/close device, would by its nature of avoiding sliding contact between components exhibit low wear when metering hydrogen fuel. Further, it can be shown by computer simulation that the injector can be designed to withstand cyclic stresses and deliver hydrogen fuel at a rate suitable for direct injection to the cylinder of an IC engine. Section 1.2 outlines the specific objectives in more detail.

1.2 Project Objectives and Report Structure

The initial aim of the report is to set the current work in context with other work in the field. First, a comprehensive and critical review of the published accounts of researchers' experiences with hydrogen fuel induction is given in Chapter 2. Carburetion, manifold injection (MI), port injection (PI) and direct injection (DI) fuel induction methods are examined in turn. The equipment used to induct the fuel is described, highlighting particular design considerations, including the general operating principle and what supply pressure is required to achieve sufficient fuel mass flow rate to the cylinder. Wear of injector components characteristic of particular types of fuel injector will also be discussed.

Published performance results will then be compared, paying close attention to methods of avoiding pre-ignition and backfire that are characteristic of hydrogen-fuelled engines. The effect of the choice of fuel induction technique on volumetric efficiency, pumping losses and thermal efficiency will be described. Fuel mixing plays a vital role in these performance results, and the report will describe the differences in this process between the various induction techniques. Published NO_x emissions are also given for each fuel

induction method and compared to those of petrol and diesel fuel. Published data of the performance of several single-cylinder engines operated by various hydrogen fuel induction methods have been collated and the report will summarise these.

Drawing on the experience of past researchers, Chapter 3 outlines a new design of diaphragm-type injector capable of metering high pressure hydrogen fuel, that addresses the problem of wear of contacting parts. An investigation was first carried out into the possibility of incorporating a pump in the injector unit, and although this was not investigated further, the report outlines key energy considerations for this feature.

The new injector design is based on features of a commercially available injector, designed for manifold injection of natural gas, and a further experimental injector designed for a direct injected hydrogen engine. Key design features will be described, including the operating principle and flow rate characteristics. Design calculations are described that assess the effect of the load and support environment on the diaphragm stress and deflection. The effect of elevated supply pressure on other injector components is also considered. The diaphragm stress and deflection calculations are compared with a Finite Element Analysis (FEA) model of the diaphragm component, and a more complex model of the environment is described that more accurately represents the loads applied to this key injector part.

Three injector models have been translated into geometry for Computational Fluid Dynamics (CFD) analysis of compressible hydrogen flow. Chapter 4 describes the development of the geometry of the three models in the Gambit environment. The actual geometry the models were based on is described, highlighting key differences between the real and the modelled flow paths. Features of the mesh scheme developed in the Gambit environment are also described.

The Fluent CFD package was used to carry out compressible flow analysis using the three developed geometry cases. Chapter 4 also describes parameter settings universal to all the models investigated, including gas properties and the type of solver used. The process involved in obtaining a stable, converged solution is also outlined, including consideration of the computation time required for each model.

Chapter 5 outlines the results of CFD modelling of the geometry described in Chapter 4. Of the three models developed, the approximated geometry of a Bosch poppet-valve injector was first used to critically assess the effectiveness of CFD in modelling compressible hydrogen flows. A specific aim of this analysis was to compare the sonic-flow mass flow rate-supply pressure relationship between published and modelled results. The analysis also makes a comparison between published and modelled results of the relationship between effective flow area and supply pressure. Further, by comparing the modelled effective flow area with the geometric minimum flow area, an estimate of the discharge coefficient of this injector is made.

Further validation of the CFD compressible flow modelling described in Chapter 5 is provided by comparing published and model results of hydrogen flow through an annular plate injector which in part forms the basis of the new design. In particular, a comparison is made between sonic-flow mass flow rate of published and modelled results, and of the effective flow area-supply pressure relationship. Critical assessment of the geometry model is made, based on comparison of the mass flow rate results. The discharge coefficient of the injector is also estimated.

Finally, the geometry of the new diaphragm injector design is modelled. This analysis first outlines theoretical sonic-flow mass flow rate and the effect of the back pressure on the flow field, according to compressible flow theory. The model critical pressure ratio for sonic flow is compared with theory, along

with sub- and super-sonic mass flow rate pressure relationships. Shock wave formation at the nozzle exit is modelled for low-pressure flows and compared to expected flow patterns. An estimate of the discharge coefficient is also made by comparing theoretical and modelled mass flow rate results. The supply pressure required to achieve the highest design mass flow rate is also estimated.

Chapter 2

LITERATURE REVIEW

This chapter gives an examination of state of the art gaseous hydrogen fuel induction techniques, introducing some properties of hydrogen that need careful consideration to optimise performance. Four distinct induction methods - carburetion, manifold injection, port injection and direct injection - are discussed in turn, highlighting particular design characteristics and implications of these features to engine operation.

Typical engine performance characteristics for each induction method are described, including volumetric and thermal efficiency, propensity to backfire and NO_x emissions. Finally, performance results of single-cylinder hydrogen-fuelled engines, using the carburetion, manifold injection and direct injection induction methods, have been collated from the literature and normalised using a friction model. The results are presented in this chapter to give a comparison of expected performance from these induction methods.

2.1 Carburetion

2.1.1 Fuel Carburetion Equipment

It was the invention of the carburettor that originally secured the prominence of liquid fuels over gaseous fuels for IC engines, because it offered a simple method of fuel metering and mixing. Using a carburettor, the fuel flow rate of liquid fuels remains approximately proportional to the air flow rate. In this way carburetion of liquid fuels gives a means of quantity control - the total quantity of fuel-air mix delivered to the engine is controlled by throttling the mixture flow. Carburetion of gases can be undertaken in a somewhat different manner.

An important property of hydrogen is its lean flammability limit. In terms of equivalence ratio, ϕ (the ratio of actual to stoichiometric fuel-to-air mass quotients - equation 2.1),

$$\phi = \left(\frac{m_{fuel}}{m_{air}} \right)_{actual} / \left(\frac{m_{fuel}}{m_{air}} \right)_{stoich.} \quad (2.1)$$

the lean flammability limit of hydrogen in air has been found experimentally to be around $\phi = 0.1$ [4]. By comparison, the lean flammability limit of petrol vapour in air is $\phi = 0.7$. This means that for hydrogen a wider range of fuel mixtures is available compared with petrol, with which to control engine load. To take advantage of this capability, hydrogen IC engine researchers most often adopt a method of “quality control”; maintaining a wide open throttle (WOT) and controlling engine load by varying the fuel-air ratio, rather than the total quantity of fuel-air mix inducted. The benefits of this to engine performance are discussed further in Section 2.1.2.

For hydrogen and other gaseous fuels, carburetion can offer an advantage over port or direct injection (see Sections 2.2.1 and 2.4.1). Since the density

of gaseous fuels is much lower than for liquids, a higher volume flow rate is needed to induct sufficient fuel mass for the cycle. If there is a long time available for fuel induction, a relatively low supply pressure can be employed to achieve the required mass flow rate. In turn, the design of the fuel supply and induction equipment is relatively simple. This also implies that the available pressure in the storage tank can be used to deliver hydrogen until the tank is nearly empty without the need of a pump.

Several examples of carburetted hydrogen engine operation have been published. Typically, researchers use a gas carburettor, or 'gas mixer', with hydrogen continually supplied into the air stream. The fuel-air ratio is controlled by adjusting the hydrogen gas supply pressure, ranging from atmospheric pressure [5] to 1.5 bar gauge [6].

2.1.2 Engine Performance

Carburetion can be categorised as a 'pre-mixed', or 'external mixture formation' method of fuel induction. Particularly for hydrogen fuel, this leads to a significant drawback since pre-mixing of the fuel and air in the inlet manifold leads to conditions highly conducive to backfire. The minimum energy required to ignite a stoichiometric hydrogen-air mix is low at 0.02 mJ compared with 0.24 mJ for petrol and air [4]. This is the minimum spark discharge energy required to initiate a local, propagating flame kernel in a fuel-air mixture, and is dependent on fuel-air mixture ratio [7]. Also, as discussed in Section 2.1.1, the flammability limits are much wider for a hydrogen-air mix compared with petrol and air; 5-75% by volume compared with 1.0-7.6% for petrol [4]. These two properties of hydrogen mean that hot residual exhaust gases or hot points in the cylinder at spark plug electrodes or carbon deposits can easily ignite the inducted charge before the scheduled spark. If unsched-

uled ignition, or pre-ignition, occurs at a point when the inlet valve is open the flame can propagate past the valve into the manifold, resulting in backfire. Sierens and Rosseel [8] have experienced 'run-away' pre-ignition with their carburetted hydrogen engine, where unscheduled ignition occurred progressively earlier in the cycle until backfire occurred before inlet valve close (IVC).

Several methods have been adopted to avoid pre-ignition and backfire in carburetted hydrogen engines. Jing-Ding *et al.* [9] reason that increasing the compression ratio (CR) reduces the amount of residual exhaust gases in the cylinder at gas exchange after the exhaust stroke, and that this can control backfire by preventing pre-ignition from contact with the hot gases. However, while increasing the compression ratio increases the thermal efficiency, it is limited by the onset of end-gas pre-ignition (discussed later in this section) during the compression stroke [7]. Jing-Ding *et al.* have published performance results of their carburetted hydrogen engine (Figure 2.1), showing the increased thermal efficiency at elevated compression ratios.

These researchers also adopted charge cooling prior to intake to reduce the risk of backfire. Injecting a spray of water into the fuel-air stream to cool the cylinder environment has also been used to successfully eliminate backfire [5,10]. However, water vapour can seep past the piston rings and mix with the oil, reducing its lubricating properties. Exhaust gas recirculation (EGR) has also been proven to reduce backfire [10], again by cooling the cylinder environment. This also has the effect of reducing NO_x emissions. Some researchers have reported that tying the spark plug cables together can lead to induction effects that cause ignition in one cylinder when a scheduled spark occurs in another [5,11]. Sierens and Rosseel [8] report that limiting the equivalence ratio to $\phi = 0.5$ prevents backfire occurring, but power output is compromised as a result.

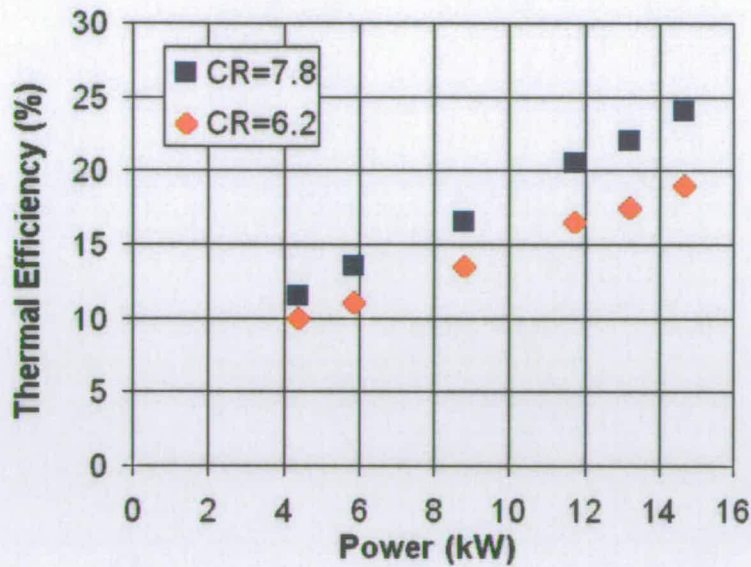


Figure 2.1: Thermal Efficiency vs Power of a Carburetted Hydrogen Engine at Different Compression Ratios [9]

External mixture formation of hydrogen and air can offer an advantage to engine operation over direct injection (Section 2.4.1), since the time available for induction and complete mixing of the fuel and air is maximised. This is a particular advantage for liquid fuels, since evaporation of the fuel and complete mixing must occur before combustion.

A homogeneous mix of hydrogen and air burns much more rapidly than petrol vapour and air, with a maximum laminar flame speed of 2.91 m/s in air compared with 0.37 m/s for petrol [4]. This has one advantage in that combustion more closely approximates the Otto ideal cycle with constant volume combustion, and thus the indicated thermal efficiency is improved [12]. One effect of the rapid combustion of hydrogen is that the spark timing must be retarded compared with petrol fuel, to achieve optimum torque. Figure 2.2 shows published data by Mathur and Khajuria of maximum brake torque (MBT) timing for a carburetted hydrogen engine as a function of equivalence ratio. At stoichiometry ($\phi = 1$), the spark advance is much closer to

top dead centre (TDC) than petrol, which typically has an optimum spark timing between 40-20°CA BTDC (crank angle degrees before top dead centre) [7]. Figure 2.2 shows that as the hydrogen-air mixture becomes leaner, or a lower compression is used, the spark must be advanced.

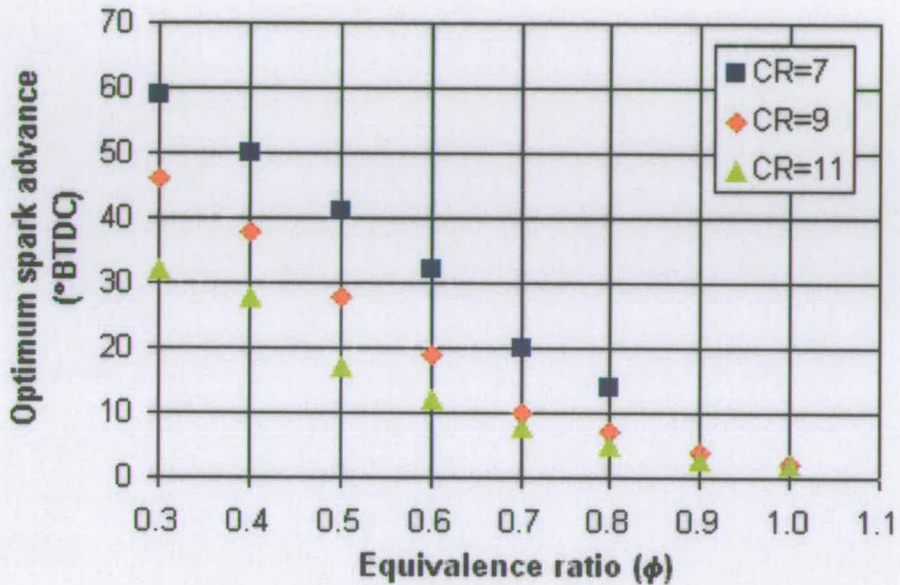


Figure 2.2: MBT Timing vs Equivalence Ratio for a Carburetted Hydrogen Engine [12]

In practice, the very rapid pressure rise that occurs with hydrogen combustion can easily lead to end-gas ignition and knock. Very high peak pressures are experienced during knocking combustion and this leads to a risk of engine damage. This can also create high peak temperatures, and high NO_x formation as a result.

As discussed in Section 2.1.1, carburetion offers a very simple method of fuel induction for both liquid and gaseous fuels. A drawback, however, is that the fuel vapour displaces some of the air drawn into the cylinder, reducing the volumetric efficiency, η_{vol} . For gaseous fuels the displacement of air is more significant, since the volume fraction occupied by the fuel is much higher than with liquid vapour at the same equivalence ratios. For instance,

the petrol vapour volume fraction in air at stoichiometry is 1.7%, whereas for hydrogen it is 29.6% [13].

For throttled operation, pumping losses are also incurred due to the low manifold pressure. For hydrogen, since load control can be achieved by quality governing rather than throttled quantity control (see Section 2.1.1), most researchers keep a wide open throttle during tests, so pumping losses are less significant. Figure 2.3 shows results of throttled and unthrottled carburetted hydrogen brake thermal efficiency (BTE), both compared with throttled petrol operation on the same engine. The figure clearly shows the gain in BTE for unthrottled operation due to reduced pumping losses. For the throttled case, thermal efficiencies similar to those of the petrol equivalent are achieved. This may imply that any volumetric efficiency losses due to the displacement of air by hydrogen are balanced by higher efficiency, constant volume combustion of the homogeneous blend. The figure also shows, however, that the maximum power developed by the engine was severely limited by the occurrence of backfire. This is shown in Figure 2.3 by the absence of available data at BMEP higher than approximately 4-5 bar. These researchers cite hot deposits in the cylinder as being the primary cause of the backfire.

It has also been shown that the indicated thermal efficiency can be significantly increased with quality governing with a lean charge. The results of Mathur and Khajuria [8] shown in Figure 2.4 again show that efficiency is improved by using higher compression ratios, but also show improved efficiency with leaner charge mixtures. As the mixture strength approaches the lean flammability limit the efficiency drops.

Corresponding specific NO_x emissions for the throttled and unthrottled cases of Figure 2.3, published by Swain *et al.*, are shown in Figure 2.5. The results show that for quality governed, unthrottled hydrogen carburetion,

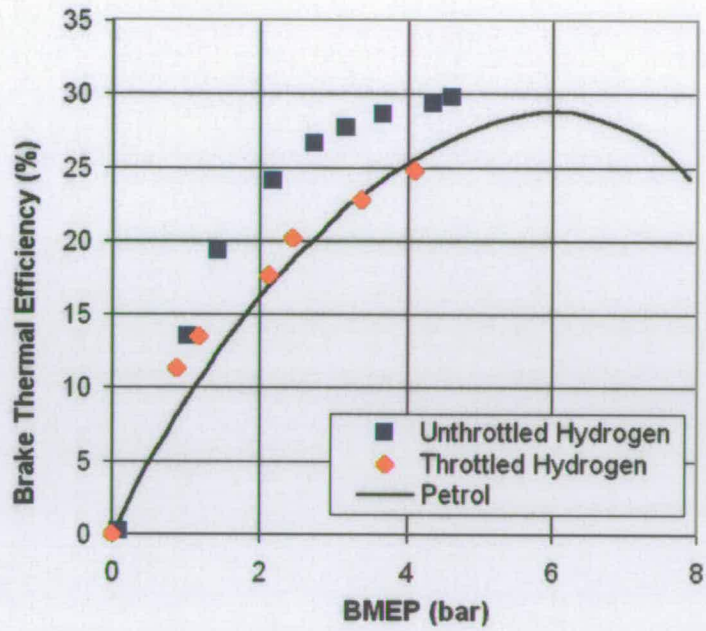


Figure 2.3: Comparison of Throttled and Unthrottled Carburetted Hydrogen and Carburetted Petrol Engine BTE [10]

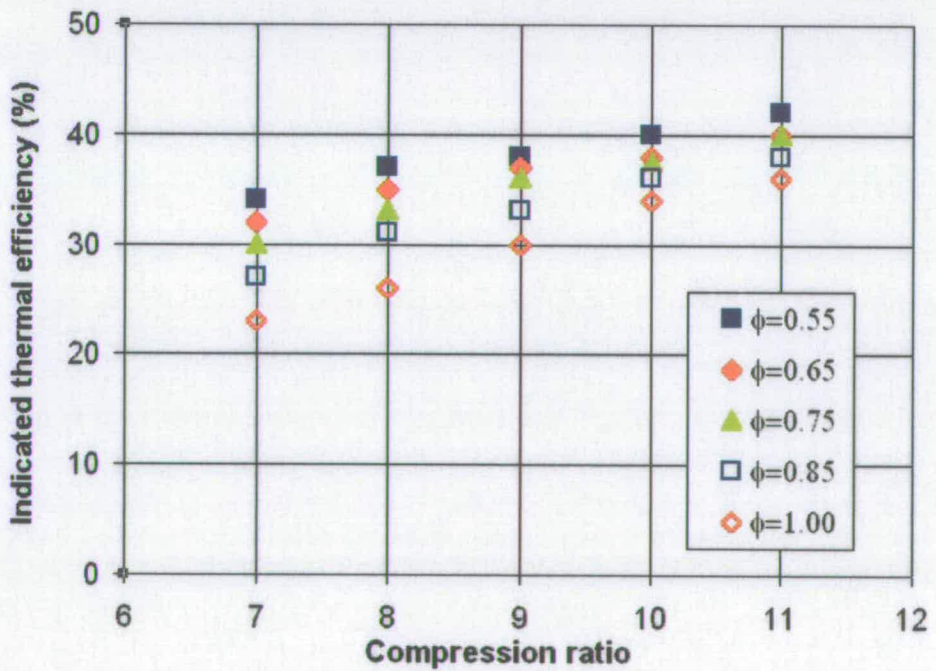


Figure 2.4: ITE vs CR; Effect of Equivalence Ratio in a Carburetted Engine [8]

much lower NO_x emission levels can be achieved than with a throttled petrol engine. For the throttled hydrogen case, the high NO_x formation could be due to more turbulent intake flow, leading to a more rapid pressure rise on combustion and high peak temperatures developed in the cylinder.

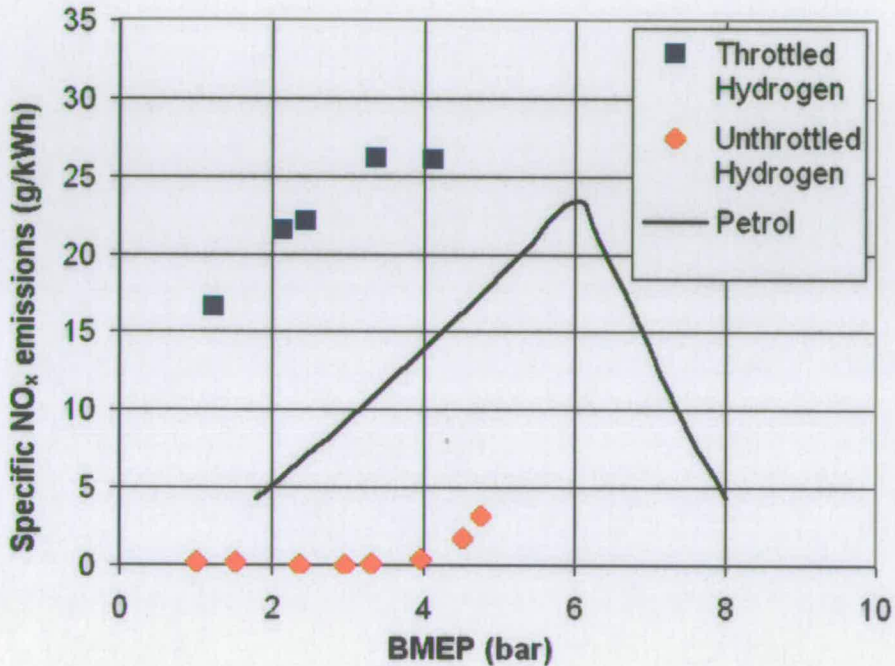


Figure 2.5: Comparison of Throttled and Unthrottled Carburetted Hydrogen and Carburetted Petrol Engine Specific NO_x Emissions [10]

2.2 Manifold Injection

2.2.1 Inlet Manifold Fuel Injection Equipment

In attempts to avoid conditions leading to backfire in a hydrogen engine, many researchers have adopted the manifold injection method of fuel induction in preference to carburetion. Rather than continually supplying hydrogen into the air stream as with gaseous carburetion, an injection of gas into the intake manifold can be timed to finish before the inlet valve closes. In

this way it is possible to ensure that there is no combustible hydrogen-air mix in the inlet manifold at a time when pre-ignition and backfire can occur. This method of avoiding backfire is discussed further in Section 2.2.2. MI also offers a precise means of quality governing as opposed to throttled quantity control (see Section 2.1.1).

As with carburetion, MI can be categorised as pre-mixed charge formation. Since there is ample time available for mixing of the gases, the supply pressure can be kept low by comparison with direct injection to induct the required mass of fuel (see Section 2.4.1). This somewhat simplifies the design of the fuel induction equipment for MI as compared with DI.

An illustration of the position of a manifold hydrogen injector is shown in Figure 2.6. This 12-litre bus engine was developed by MAN to run on either petrol or hydrogen, as the availability of the latter may not always have been available [14]. For this engine, the injection pressure was 3.5 bar gauge, and pressures ranging from this to 5.4 bar gauge [15] are typically used to achieve the required mass flow rate during the inlet valve open (IVO) period (see Appendix A).

Fuel flow rate, and in turn fuel-air ratio, can be controlled by either varying the injection pressure while keeping the injection duration constant (pressure control), or by varying the injection duration whilst maintaining a constant injection pressure (duration control). Duration control is often more easily achieved than pressure control - for instance by controlling the voltage pulse-width supplied to a solenoid actuator (pulse width modulation, PWM) - and most researchers adopt this method of varying the equivalence ratio [15, 16]. However, Mathur and Das [13] have reasoned that pressure control is preferable, since elevated pressures would increase the velocity of the gas jet and improve charge mixing.

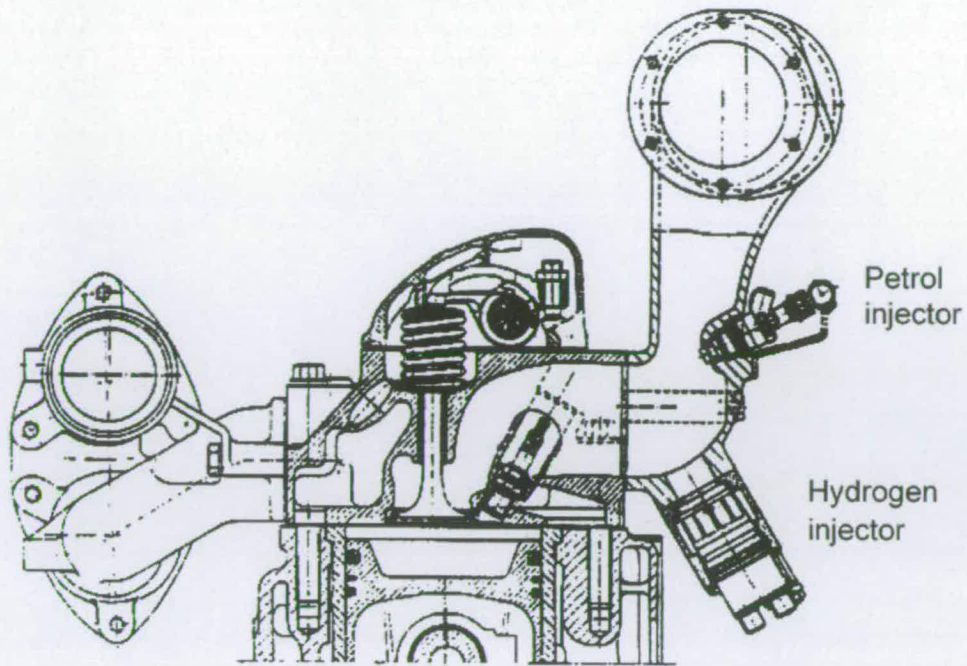


Figure 2.6: Example of the Position of a Manifold Hydrogen Injector [14]

Injector designs typically comprise an electronic or mechanical timing control device, an open / close valve and a valve actuation scheme. Mathur and Das [13] used a cam-actuated scheme in their tests, and timing was controlled by altering the phase shift relative to crank angle. However, most researchers adopt some form of electrical crank angle sensing coupled with electronic timing control and solenoid actuation [14, 16, 17].

A variety of types of open / close valve devices have been employed in manifold injectors. For manifold injection, researchers have used commercial natural gas injectors to meter hydrogen fuel to the inlet manifold [16, 18]. Figure 2.7 shows a BKM Servojet solenoid-actuated ball-poppet injector, designed for use with natural gas. When the solenoid is de-energised, the ball is forced up against the valve seat by the gas supply pressure and spring force. When energised, the ball is forced down against the spring force, and the valve is opened.

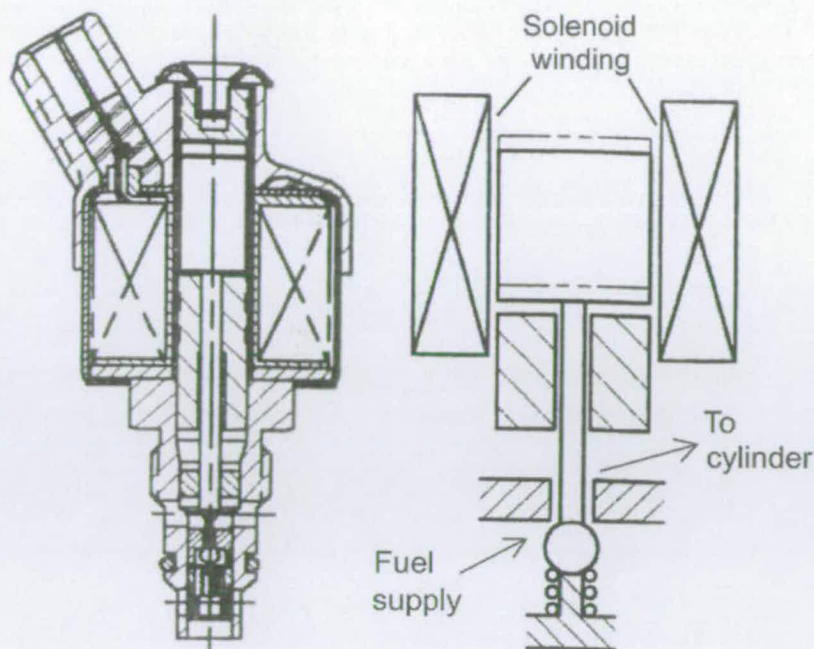


Figure 2.7: BKM Servojet Solenoid-Actuated Ball-Poppet Manifold Injector [19]

Frequently, conical poppet valves are used to provide an open / close mechanism in injectors. An example of this is the Bosch natural gas injector shown in Figure 2.8. In this example, the energised solenoid pulls the pintle away from the valve seat against a return spring to open the valve.

A further design of gaseous fuel injector open / close mechanism is shown in Figure 2.9. This injector is also solenoid actuated, and uses an annular plate solenoid armature and reed spring as the open / close device. When de-energised, the spring force holds the annular plate down, where it seals the flow plate as shown in Figure 2.9. With the solenoid energised, the armature is forced upwards against the spring force and the plate deflects away from the flow annulus. A more detailed diagram of this injector is shown in Figure 4.3.

Injectors designed for use with natural gas or other fuels have been shown in theory to be capable of delivering the required mass of hydrogen fuel in

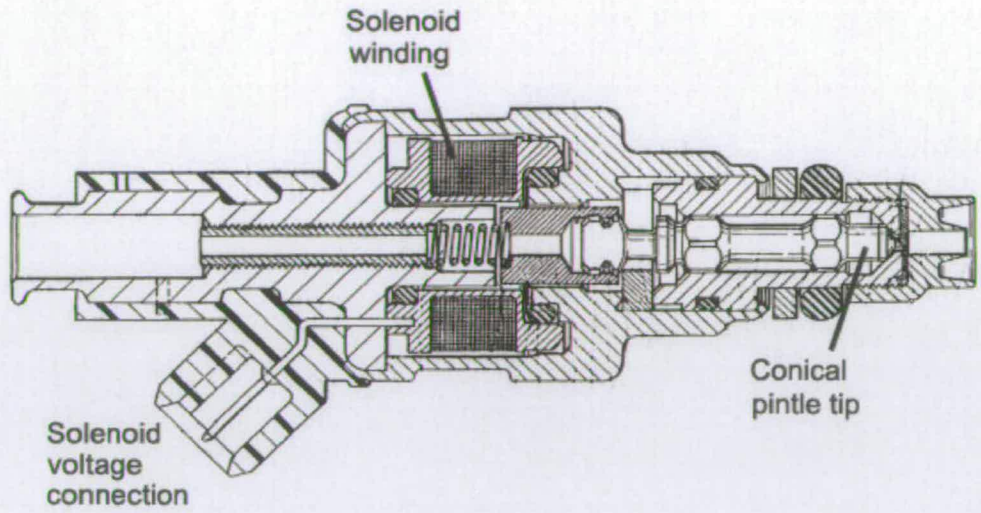


Figure 2.8: Bosch Solenoid-Actuated Conical Tip Injector [20]

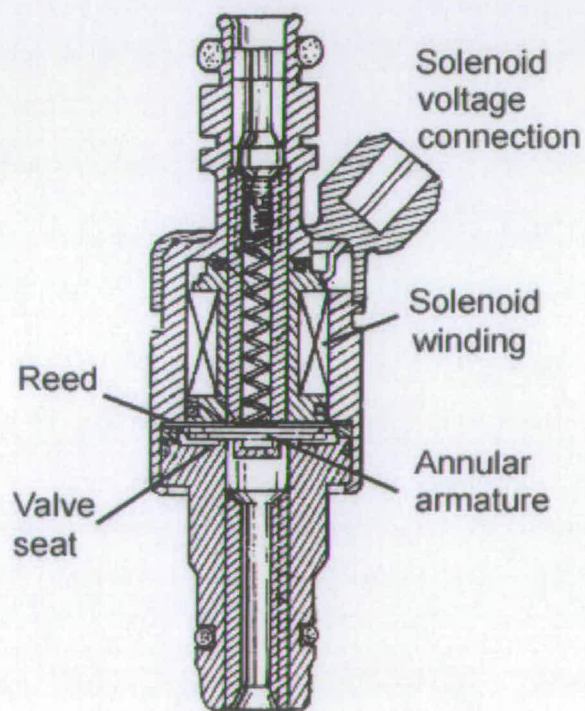


Figure 2.9: Quantum Solenoid-Actuated Reed / Annular Plate Manifold Injector [21]

the time available for manifold injection. Pashley and Stone [22] conducted flow rate tests on a Bosch methanol injector, similar to that shown in Figure 2.8. To determine the effective flow area at the nozzle throat, they measured the flow rates of air, carbon dioxide, CO₂, helium, He, and nitrogen, N₂, under varying supply pressures and compared the results with sonic compressible flow theory (see Section 2.4.2). They then predicted mass flow rates of hydrogen assuming the same flow area and supply pressures. Their results demonstrate the predicted linear relationship between mass flow rate and supply pressure, and a maximum flow rate at 10 bar supply pressure of 1.25 g/s [22].

Kabat and Heffel [20] have measured the flow rate of hydrogen through a Bosch natural gas injector, reporting 0.39 g/s at an injection pressure of 4.2 bar. They report very similar flow rates for the injectors shown in Figures 2.7 and 2.9. These published flow rate data form the basis of CFD model validation in Section 5.1. Appendix A gives calculations of the required mass of hydrogen per injection for a given engine capacity.

These researchers have also conducted extensive durability tests of the natural gas injectors shown in Figures 2.7, 2.8 and 2.9 when metering hydrogen fuel. With liquid fuels, cooling and lubrication of the injector moving parts can be provided by the fuel itself. Natural gas contains particles of compressor oil and this serves as lubrication for natural gas injectors. For hydrogen gas there is very little inherent cooling or lubrication capability and this has considerable durability implications on hydrogen injector design. For the BKM ball-poppet injector, these researchers tested a variety of seating materials to provide improved durability and compared the results with the baseline injector with no added material. The baseline injector failed after 80 hours' continual operation at an equivalent engine speed of 1800 RPM. Inspection of the injector parts showed extreme wear on the drive pin tip.

With improved seating materials, 286 hours' continual operation at equivalent engine speeds of up to 6000 RPM without failure was achieved.

For the Bosch injector shown in Figure 2.8, failure occurred after 80 hours' operation when the pintle seized within the injector bore. Figure 2.10 shows photographs of the internal components of the injector after failure using hydrogen gas (Figure 2.10(a)) and after operation with natural gas (Figure 2.10(b)). The figure shows extreme wear around the injector pintle with hydrogen operation. For the Quantum injector shown in Figure 2.9, no failure and very little wear was displayed after completed rigorous testing and subsequent tear-down inspection, with only $15\ \mu\text{m}$ -deep marks visible where the annular plate contacted the valve seat. The complete durability test comprised the following:

- 500 hours' continual operation at 15 Hz (1800 RPM) under 4 bar supply pressure
- ten 24-hour cycles through 1 hour at 15 Hz, 4 bar pressure, 22 hours at 35 Hz, 3 bar pressure, 1 hour at 50 Hz, 3 bar pressure
- three 24-hour cycles as above, but with 48 hours' shut-down time between 24-hour cycles

Exhibiting a small molecular volume [23] and low viscosity [24], hydrogen will more readily leak through small openings than other gases. Heffel *et al.* [25] have tested four variants of the BKM ball-pintle injector shown in Figure 2.7 with hydrogen fuel and reported the leakage rate under various supply pressures. Their results show the highest leakage rate measured was 3 mg/s under 12 bar supply pressure, and this was thought to be negligible compared with the main injection fuel flow rates. Swain and Swain [26] have

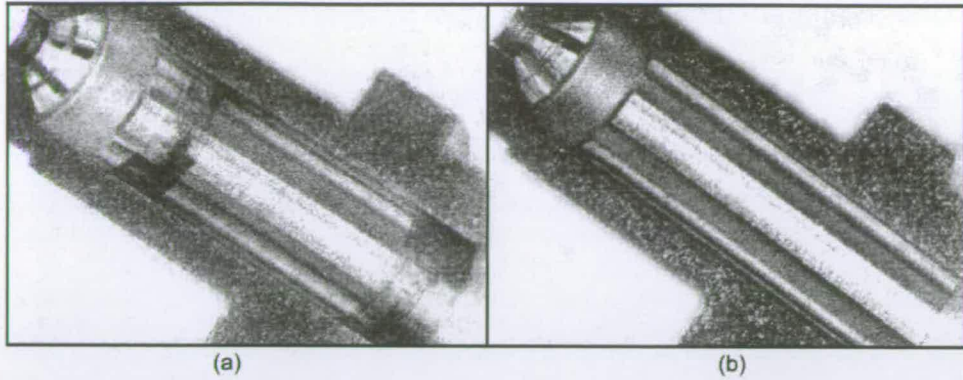


Figure 2.10: Post-Test Inspection of Bosch Injector For Hydrogen (a) and Natural Gas (b) Operation [20]

reported similar leakage rates of a Siemens fuel injector, indicating 0.8 mg/s at 4 bar supply pressure.

2.2.2 Engine Performance

Manifold injection can be categorised with carburetion as pre-mixed fuel induction. This means that, as with carburetion, MI carries a risk of back-firing into the manifold if pre-ignition occurs before the intake valve closes (see Section 2.1.2). However, researchers have been investigating the ability to reduce the risk of backfire by timing the injection period relative to the IVO period. This strategy has been referred to as timed manifold injection, TMI [4].

Before the start of injection, air only is drawn into the cylinder after IVO, cooling the cylinder environment and reducing the risk that the mixture could pre-ignite from hot residual gases or hot points at spark plug electrodes etc. This also has the effect of reducing the peak combustion temperature and reducing NO_x formation [27]. The injection is stopped and more air is drawn into the cylinder before IVC, effectively purging the inlet manifold of hydrogen between cycles [26].

Other methods to reduce the onset of pre-ignition and backfire include limiting the equivalence ratio and the spark timing. Tang *et al.* [28] reported run-away pre-ignition in their MI hydrogen engine at an equivalence ratio of $\phi = 0.73$. Cylinder pressure traces recorded over the event are shown in Figure 2.11. The results show the cylinder pressure oscillations characteristic of knocking combustion occurring. The knock becomes progressively more intense until ignition occurs before the scheduled spark timing. Extremely high peak pressures are recorded for these cycles. The pre-ignition occurs progressively earlier in the cycle until the last recorded cycle where pre-ignition occurs before IVC. Backfire resulted at this cycle and the spark ignition was stopped; Figure 2.11 shows the final cycle with no combustion. The lower compression pressure of this cycle may be due to purge gases being used for fire suppression in the test cell after engine shut-off.

As Figure 2.11 shows, the injection duration for these tests was close to one complete crank revolution. These researchers concluded that they could eliminate pre-ignition by limiting the equivalence ratio to between $\phi = 0.6$ and 0.64, and reducing the injection duration so that the fuel avoids contact with hot residual exhaust gases.

As with carburetted hydrogen induction, manifold injection offers ample time (as compared with direct injection, see Section 2.4.1) for the fuel to form a homogeneous mixture with the inlet air. In a paper by Sierens and Verhelst [29], a project to assess the influence of injection port and air intake configurations on engine power output is documented. The four configurations they compared are illustrated in Figure 2.12.

These researchers found that varying the injection pressure while controlling injection duration to achieve equal air-fuel ratios had little effect on the power output of the engine. This suggests that elevated injection pressure has little effect to improve charge mixing. However, the different fuel induc-

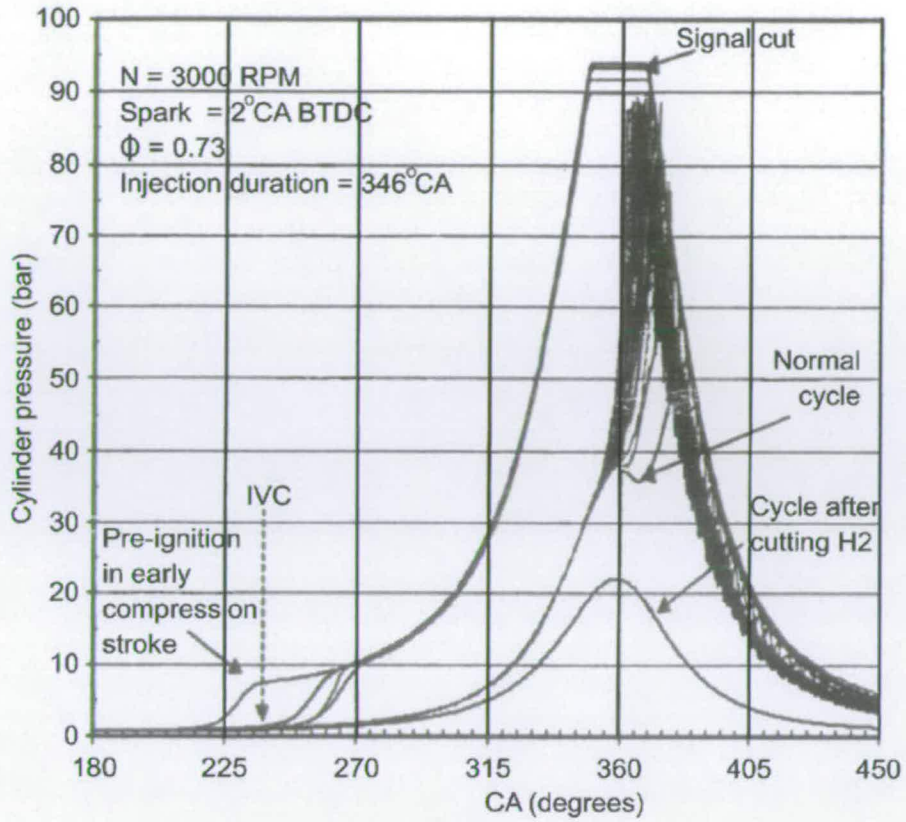


Figure 2.11: Cylinder Pressure Traces During Run-Away Pre-Ignition - MI operation [28]

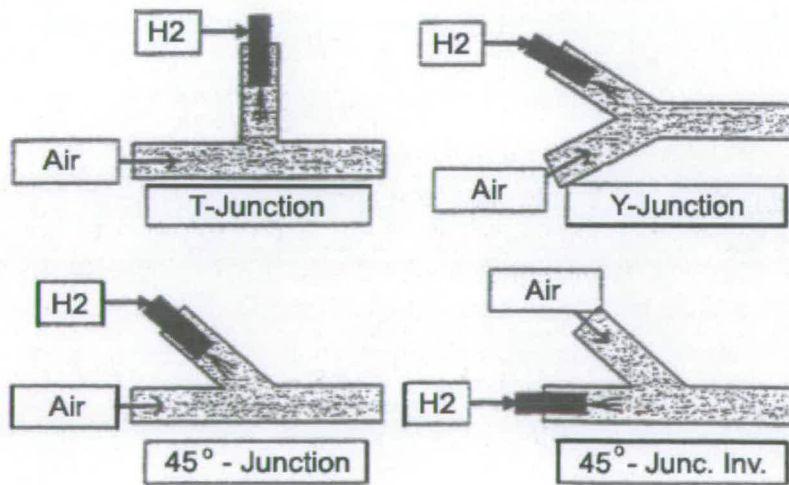


Figure 2.12: Manifold Injection Inlet Configurations for Fuel-Air Mixing Study [29]

tion configurations did have an appreciable effect on the power output, with the Y-junction shape providing the highest power - a 3% increase over the lowest power developed with the 45°-junction inverse shape. However, the fuel conversion efficiency was slightly higher with the 45°-junction than with the Y-junction; up to 0.8 percentage points, or 2.7% higher. A CFD analysis showed that with the 45°-junctions, the fuel would be more uniformly mixed at the same point downstream of the junction. These results suggest that inadequate mixing of the hydrogen-air charge can have a significant effect on engine performance.

Similarly to hydrogen carburetion, the rapid combustion of the homogeneous charge means that more retarded MBT spark timings can be employed than with petrol fuel. Figure 2.13 shows the MBT spark timing of a manifold injected hydrogen engine as a function of equivalence ratio. The results are similar to the carburetted hydrogen results shown in Figure 2.2.

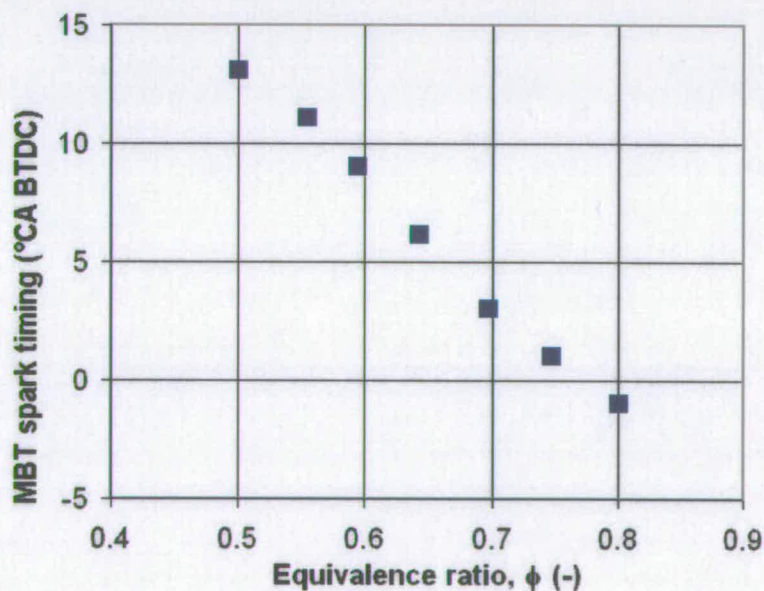


Figure 2.13: MBT Timing vs Equivalence Ratio for a MI Hydrogen Engine [28]

Because fuel mixing occurs in the manifold, volumetric efficiency losses associated with displacement of the inducted air by the fuel are incurred as

with carburetion. As discussed in Section 2.1.2, the volume fraction occupied by hydrogen at stoichiometry in air is 29%. However, it has been suggested that this can be offset by employing an elevated hydrogen supply pressure (1.37 to 5.39 bar, [13]). Volumetric efficiency at stoichiometry has been reported by Swain and Swain [26] for their manifold injected hydrogen engine. At stoichiometry, the volumetric efficiency was around 85%, and rose slightly for leaner mixtures.

Other advantages and disadvantages associated with providing an unthrottled, homogeneous mix to the engine as with hydrogen carburetion are also applicable to the MI method. Near-instantaneous Otto-cycle combustion can occur, resulting in increased thermal efficiency, although there is a risk of knock and increased NO_x formation as a result of a high pressure rise rate and high peak combustion temperatures. Unthrottled, quality governing also has the effect of increasing thermal efficiency over throttled petrol engines because pumping losses are reduced. Das *et al.* [15] have shown this experimentally, and the results are shown in Figure 2.14. Some results for operation on petrol vapour are shown also.

In Figure 2.5, some reported results of the specific NO_x emissions of an unthrottled, carburetted hydrogen engine compared with petrol were given. In a later article, the same researchers reported specific NO_x emissions of an unthrottled, manifold injected engine and the results are shown in Figure 2.15. Comparison of the IMEP (indicated mean effective pressure) results of Figure 2.15 with those of the carburetted hydrogen counterpart shown in Figure 2.5 implies that the power developed by the MI engine was not restricted by the occurrence of backfire, as it was for carburetion.

Many researchers have reported similar results of the strong influence of equivalence ratio on NO_x emissions. Typical results are shown in Figure 2.16.

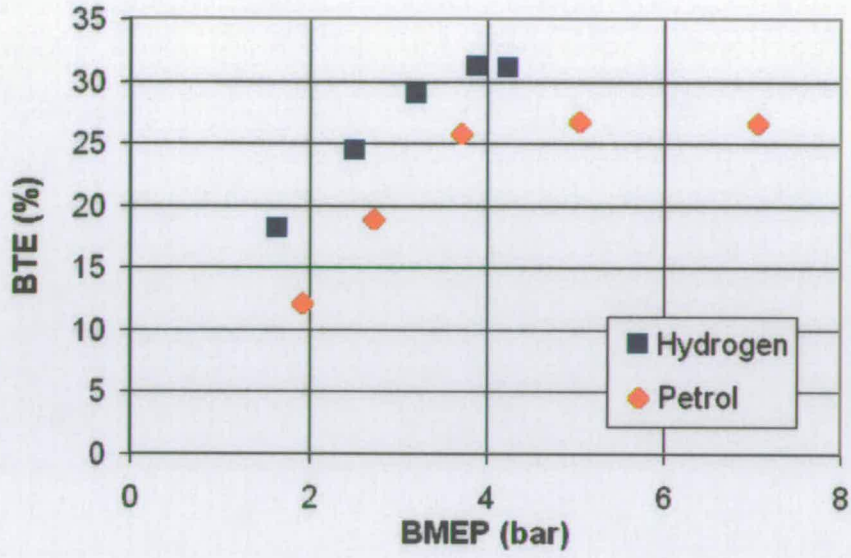


Figure 2.14: BTE; Unthrottled MI Hydrogen vs Throttled Petrol [15]

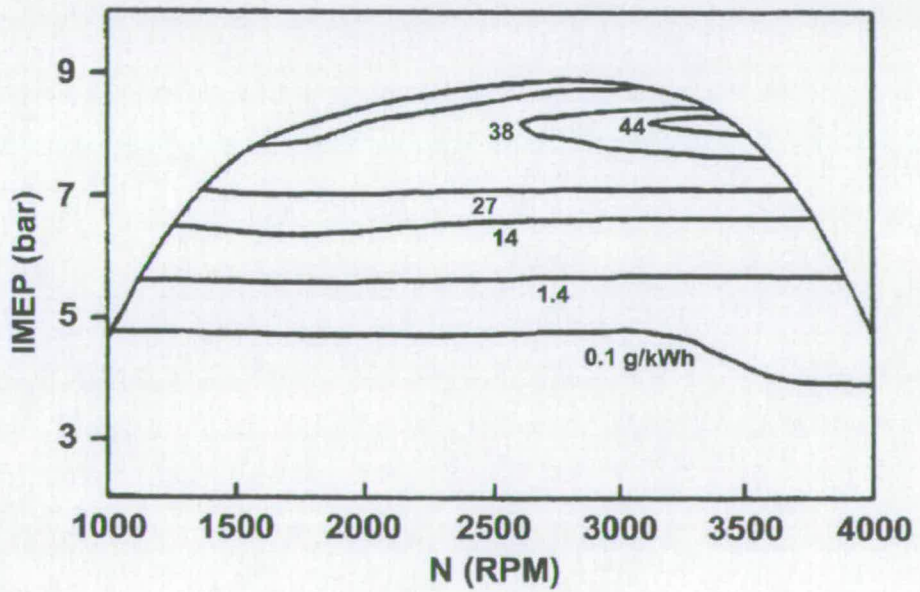


Figure 2.15: Specific NO_x Emission Map Over Load and Speed Range [16]

Generally, peak NO_x emissions occur at equivalence ratios slightly lower than stoichiometric, and decrease significantly as the mixture becomes leaner.

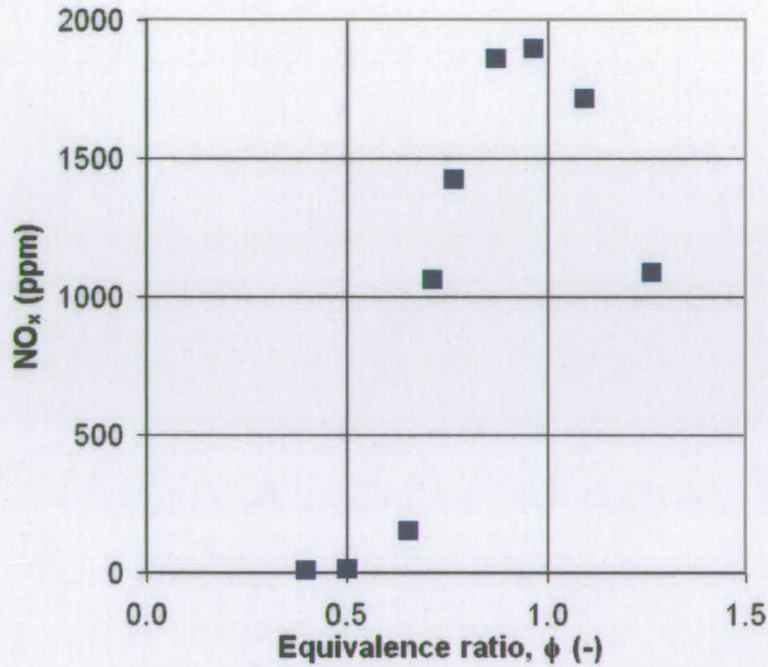


Figure 2.16: NO_x Emissions vs Equivalence Ratio [15]

MAN [14] have published NO_x , CO and unburned hydrocarbon, HC, emission levels for a 12-litre bus, converted to run on either hydrogen or petrol. Their results are shown in Figure 2.17. The figure also shows the EURO2 vehicle emissions standards for comparison. For all the emission types, the levels are much lower than for petrol operation. The CO levels are zero for hydrogen, since there is no carbon involved in the combustion of hydrogen and air. HC emissions from hydrogen engines are accountable to burning oil deposits.

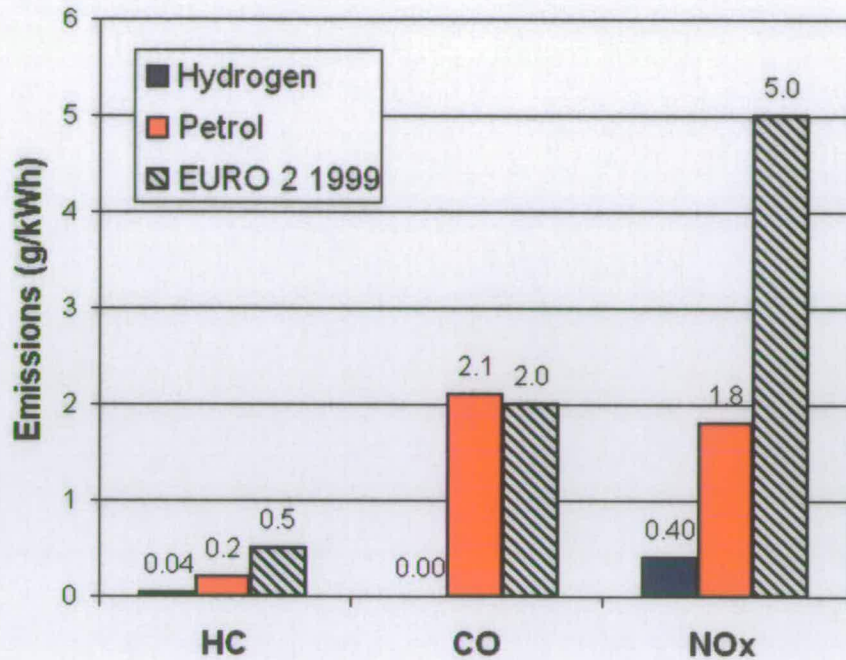


Figure 2.17: HC, CO and NO_x Emissions of a 12-litre Hydrogen / Petrol Bus [14]

2.3 Port Injection

2.3.1 Inlet Port Injection Equipment

To reduce the risk of backfire common in pre-mixed (carburetted or manifold injected) induction engines, researchers have developed the port injection (PI) method of fuel induction. This method is similar to manifold injection (see Section 2.2.1), except that for PI, hydrogen is injected at the intake port, just behind the inlet valve. This has the effect of reducing the presence of a combustible hydrogen-air mixture in the inlet manifold. As with manifold injection, it is possible to allow air only into the cylinder in the first part of the intake stroke to cool the cylinder and reduce the chance of pre-ignition from hot residual exhaust gases. Figure 2.18 shows a diagram of the general principle of PI compared with that of MI or carburetted pre-mixed charge

formation, showing how the presence of hydrogen in the inlet manifold can be avoided.

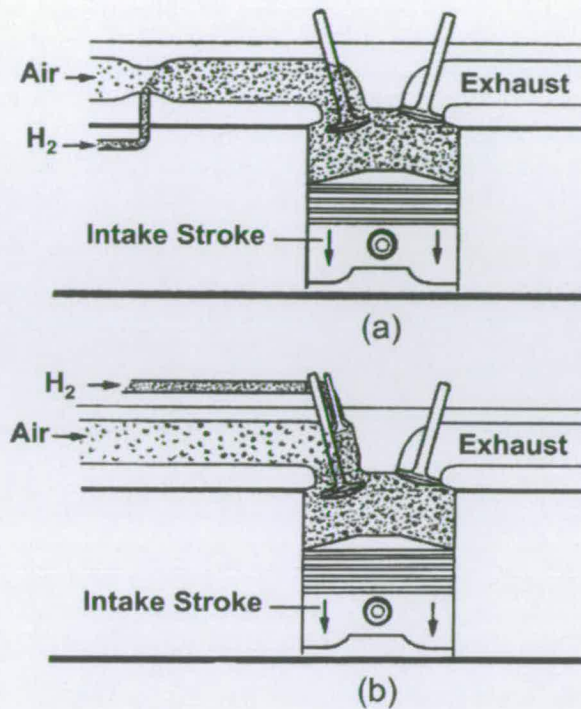


Figure 2.18: General Principles of Carburetted (a) and Port Injected (b) Fuel Induction [30]

Since injection at the inlet port is carried out within the IVO period, as with manifold injection, there is ample time (compared with direct injection, see Section 2.4.1) with which to inject the required mass of fuel per cycle. Thus injection pressures similar to those used for manifold injection can be employed. Typically, PI injection pressures range from 3 bar [27] to 10 bar [31].

Because of the similar flow requirements of PI and MI, injectors that are capable of hydrogen manifold injection can also be used in port injection applications. Lee *et al.* [31] used a BKM ball-poppet injector similar to that shown in Figure 2.7 for their PI hydrogen engine. Modifications to the intake manifold were necessary to accommodate the injector unit behind the

inlet valve. Figure 2.19 shows a PI scheme developed by Watson *et al.* [32] that uses no injector, but a sleeve-valve type inlet in parallel with the air intake. The travel of the intake valve and the dimensions of the sleeve on the valve stem allows hydrogen flow to be delayed relative to IVO, and these researchers refer to this method as delayed port admission, DPA, rather than PI. To provide a good seal when the inlet valve is closed and prevent leakage, ‘Viton’ O-rings and an O-ring backed Teflon slide valve were used.

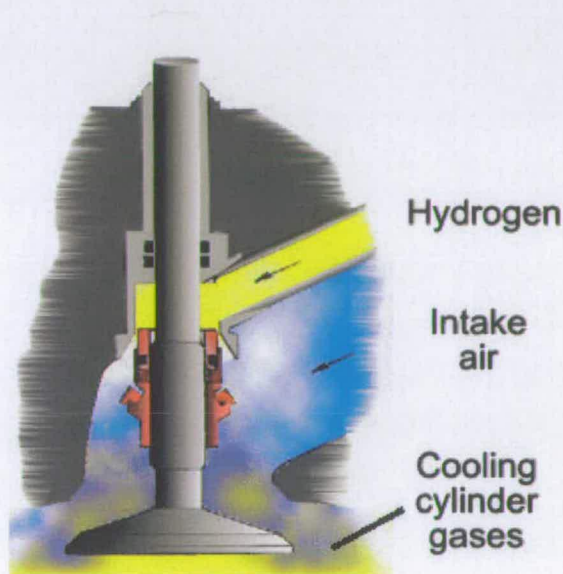


Figure 2.19: Delayed Port Admission Inlet Sleeve Valve [32]

Another variant of this type of scheme was proposed by Lynch [30], who refers to the method as parallel induction. Figure 2.20 shows a photograph of modifications they made to an engine inlet manifold to realise this method. Hydrogen is supplied through a pipe in the inlet, and as with the delayed port admission scheme, a sleeve valve on the inlet valve stem allows delayed admission of the hydrogen relative to IVO.

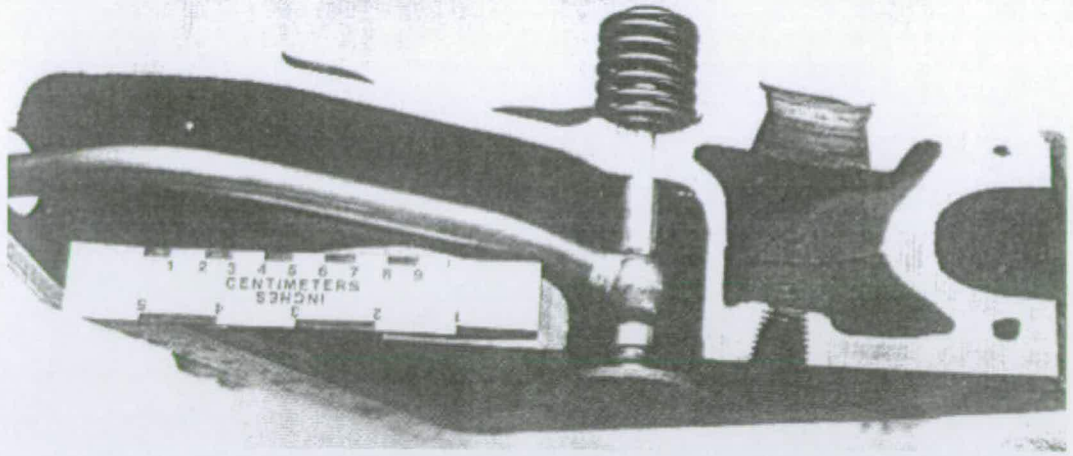


Figure 2.20: Parallel Induction Inlet Sleeve Valve [30]

2.3.2 Engine Performance

As with MI, to avoid pre-ignition caused by the inducted charge coming into contact with hot residual exhaust gases, port injection can be scheduled such that air only is inducted in the first part of the intake stroke. Similarly, injection can be timed to finish just before IVC to purge any remaining hydrogen from the inlet manifold [27].

However, Swain *et al.* [10] report problems with backfire due to hot deposits on the piston crown. Unscheduled ignition at these deposits led to run-away pre-ignition and backfire at high load. These researchers regularly cleared the cylinder of deposits to investigate higher load performance in the absence of pre-ignition. They also compared the performance of PI and carburetted hydrogen operation, and report that because of the reduction in the amount of charge in the intake manifold for PI, any backfire that did occur was much less severe than backfire in the carburetted engine.

Watson *et al.* [32] attempted to avoid the build-up of oil deposits in the combustion chamber by employing four piston rings, including two oil-control rings, and fine-honing the cylinder bore to minimise oil blowby. They also conducted tests with different lubricating oils and found that using synthetic

oil was effective in reducing oil deposits and resultant pre-ignition. These engine modifications and choice of oil improved the maximum load attainable before the onset of backfire. These researchers also tested a method of water injection and this successfully eliminated backfire over the full load range.

Performance results published by Lee *et al.* [31] show that the volumetric efficiency was 59.7% for PI hydrogen and 86.7% for carburetted petrol, both with WOT, stoichiometric operation. Comparison of this result with those of MI fuel induction (Section 2.2.2) implies that PI offers no improvement in volumetric efficiency.

The results of Varde and Frame [27] for indicated thermal efficiency are shown in Figure 2.21, along with results of a carburetted hydrogen engine. The results show improvements for both compared with carburetted petrol. This is due to the faster flame speed of hydrogen allowing combustion closer to the ideal constant volume Otto combustion, and hence improved efficiency. Figure 2.21 also illustrates the low lean limit of flammability for hydrogen compared with petrol. For injected hydrogen, the lean equivalence ratio limit was higher than that for carburetted hydrogen. These researchers reasoned that this was because there was less time for mixing to a uniform blend for PI, and this raised the lean flammability limit.

Swain *et al.* [10] compared results of carburetted and PI hydrogen performance, and carburetted hydrogen results are shown in Figure 2.3. For comparison with the same engine, their results for PI are shown in Figure 2.22. Comparison of Figures 2.3 and 2.22 also show similar improvement in thermal efficiency over petrol fuel with carburetion and PI hydrogen. However, for PI the backfire load limit is extended. As mentioned previously, these researchers extended this limit by clearing the combustion chamber of oil deposits, and their results in this load range are also shown in Figure 2.22.

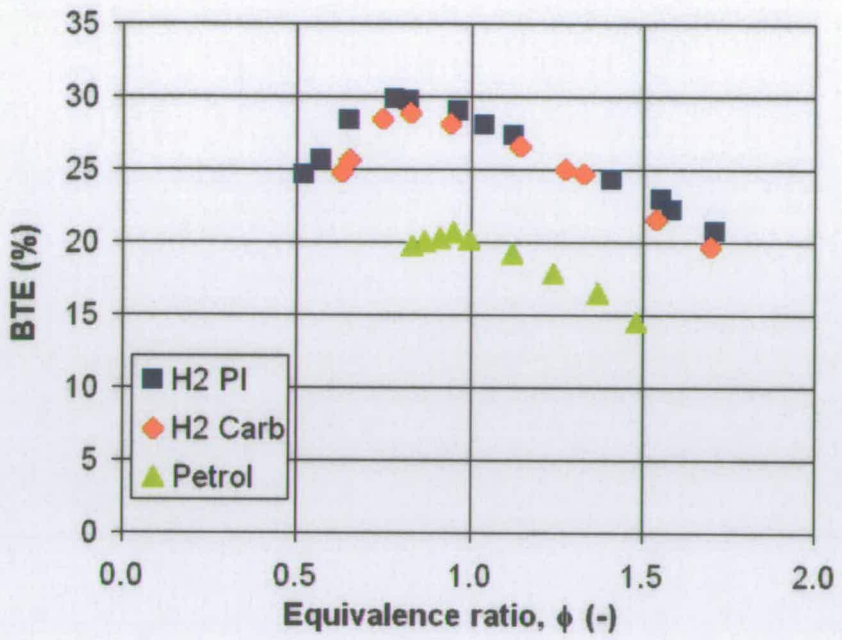


Figure 2.21: BTE vs Equivalence Ratio for PI and Carburetted Hydrogen and Petrol [27]

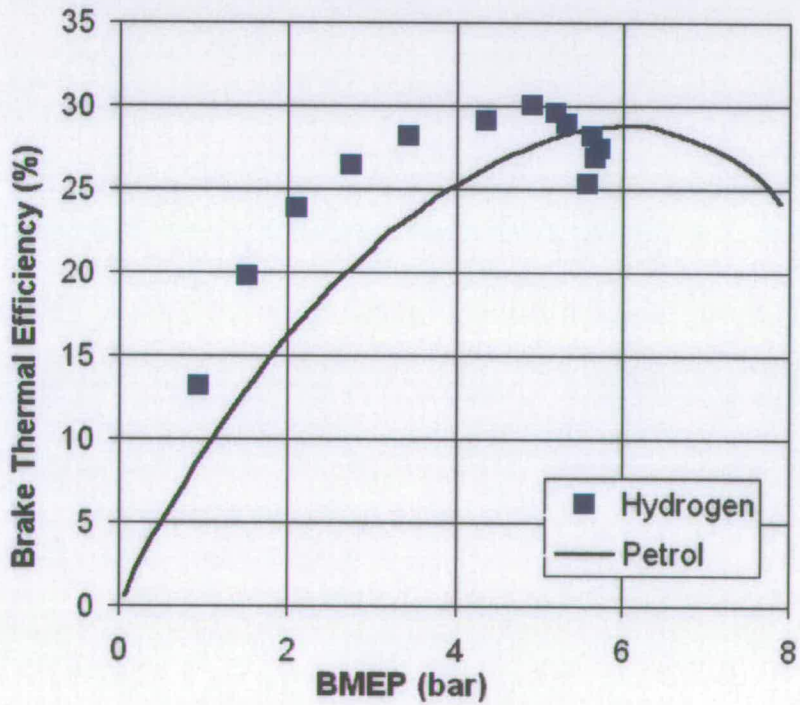


Figure 2.22: Thermal Efficiency vs Load; PI Hydrogen and Carburetted Petrol [10]

Corresponding specific NO_x emissions for the results shown in Figure 2.22 are shown in Figure 2.23. The results are similar to those of the unthrottled carburetted hydrogen engine shown in Figure 2.5, but show that at the higher loads attained by extending the backfire load limit, NO_x emissions increase to a maximum of 60% higher than those of petrol.

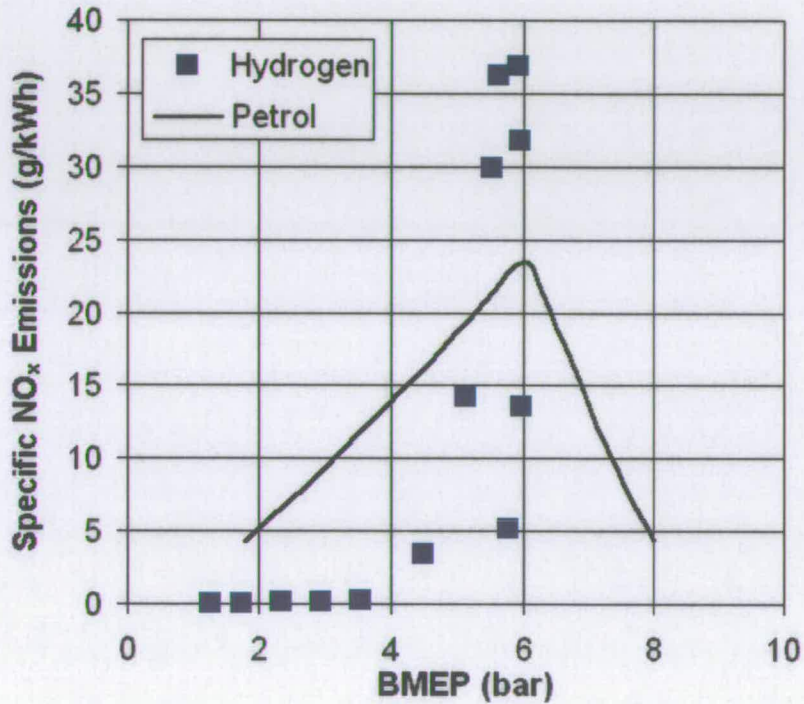


Figure 2.23: Specific NO_x Emissions for PI Operation [10]

2.4 Direct Injection

2.4.1 Direct Cylinder Injection Equipment

A method of avoiding the presence of combustible charge in the intake manifold and therefore eliminating the risk of backfire is to inject fuel directly into the cylinder after IVC. This method has been found by many researchers to successfully eliminate backfire, but early, unscheduled ignition or knocking

combustion have remained a problem. This is discussed further in Section 2.4.2.

Examples of injection directly into the cylinder and injection into a combustion side-chamber are shown in Figure 2.24 to illustrate the general principle. Figure 2.24(a) shows a bowl-in-piston chamber designed to promote charge motion during compression, with the hydrogen sprayed radially outwards in several jets into the bowl to assist charge mixing. For the side-chamber shown in Figure 2.24(b), quartz windows were employed for combustion visualisation, and an additional port was provided for pre-mixed supply for calibration of flow visualisation equipment. This arrangement allows induction of the hydrogen during air intake while containing the fuel in the side chamber, and thus preventing backfire. Further, it promotes charge motion in the side-chamber during compression to aid fuel-air mixing [33].

If no pre-chamber is used, since injection commences after IVC with direct injection there is much less time available for induction compared with carburetion, MI or PI. This means that higher supply pressures must be employed to achieve the required mass flow rate during the injection period. Also, injection must occur against the pressure in the cylinder, whereas for MI or PI, injection occurs against the manifold pressure. Generally one of two methods is adopted - low pressure, LP, injection, early in the compression stroke when the cylinder pressure is lowest, or high pressure, HP, injection in a later stage of the compression stroke. While LP DI implies increased time for induction and somewhat simpler fuel supply and injector design, HP DI late in the compression stroke can assist in avoiding pre-ignition [34]. Typical injection pressures for DI injection range from 2 bar for early DI [35] to 110bar for late DI [36].

Because of the large variation of cylinder pressure during the compression stroke, many researchers aim to provide sonic flow through the injector to

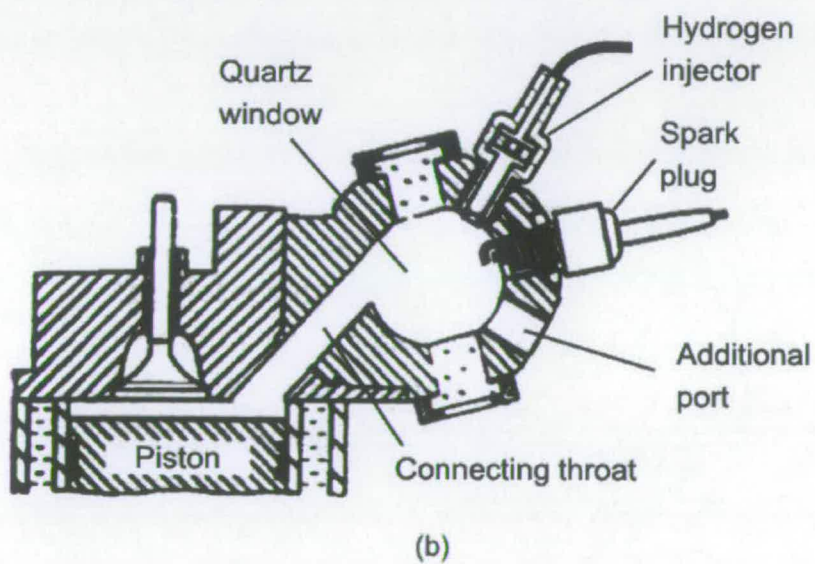
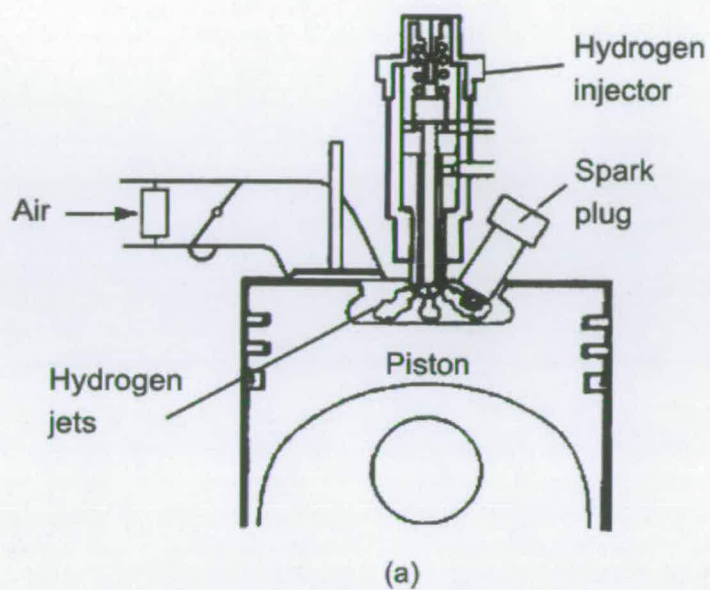


Figure 2.24: Direct Injection to the Cylinder (a) [37] and to a Combustion Pre-Chamber (b) [34]

achieve a steady flow rate during injection. Above a critical differential pressure across the injector nozzle, the flow becomes sonic, and at this condition the mass flow rate is unaffected by changes in the downstream pressure, and increases linearly with supply pressure [19,24]. Green and Glasson [38] have calculated that for their engine a supply pressure of at least 80 bar during injection is required to ensure sonic flow through the injector at all cylinder conditions.

As with MI and PI fuel induction methods, a wide open throttle is commonly used and quality control is employed by varying the mass of fuel injected. Again, as with MI and PI, this can be accomplished by varying the injection pressure control [39] or duration control [40]. Particularly with electronically controlled injectors the latter is often easier to accomplish than varying the supply pressure, and most researchers adopt this method of fuel-air ratio control.

As with manifold injection, injector designs consist of a timing control device, an open / close valve and a valve actuation scheme. However, because of the high pressure and mass flow rate requirements of DI, commercial injectors designed for manifold injection of natural gas or other fuels are not suitable for direct injection applications, and researchers typically fabricate their own units. Calculations of the required mass flow rate of direct injectors are given in Appendix A.

An example of a cam-actuated direct hydrogen injector is shown in Figure 2.25. Timing for this device was controlled by belt connection and phase shift relative to the engine drive shaft. A simple poppet valve was used as the open / close valve. This engine was a two-stroke and the inlet and exhaust ports are shown at the sides of the combustion chamber.

An example of a hydraulically-actuated direct hydrogen injector is shown in Figure 2.26. Hydraulic fluid is pumped in at A and the applied pressure

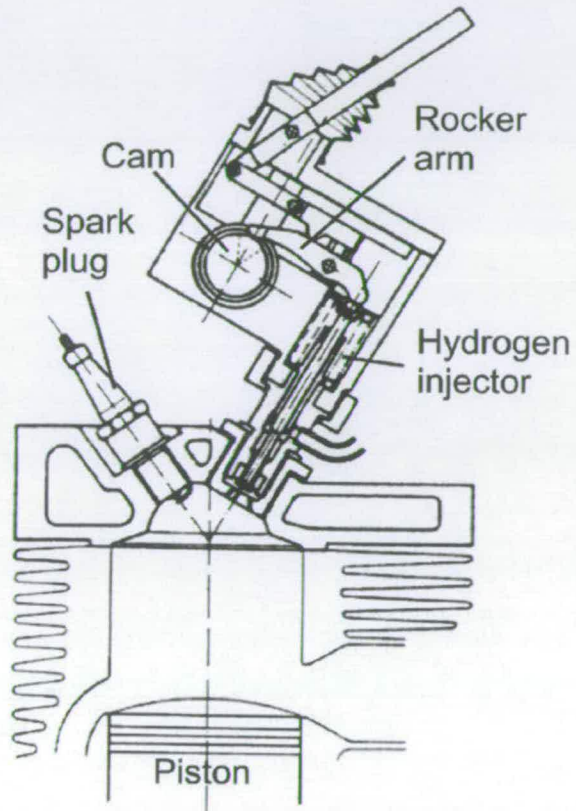


Figure 2.25: Cam-Actuated Direct Hydrogen Injector in a 2-Stroke Engine [41]

pushes the injector needle up off the tip seat against the spring force, opening the valve. Changing the thickness of the compression spacer, R, allows the spring pre-load to be adjusted.

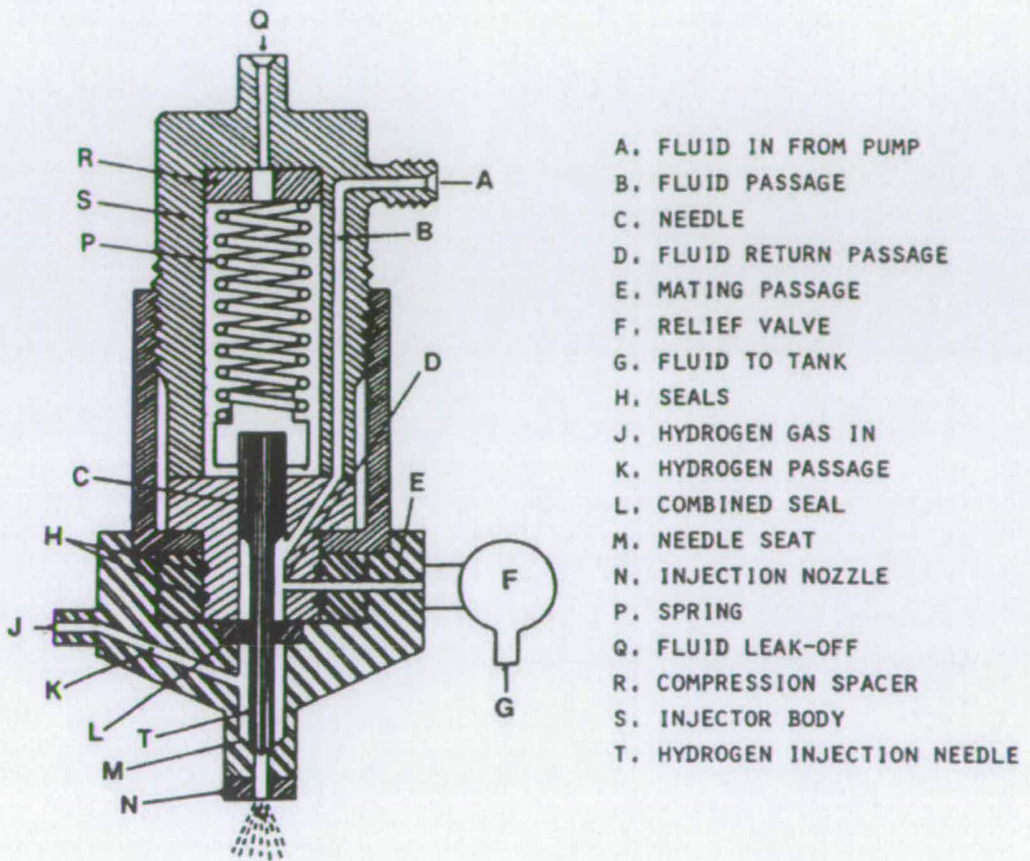


Figure 2.26: Hydraulically-Actuated Direct Hydrogen Injector [43]

A second example of a hydraulically-actuated direct injector was used by Kim *et al.* [42]. These researchers found that under their planned injection pressure of 20 bar, improved gas-tightness was required to prevent leakage from the injector. They used a poppet valve with a 1.5 mm Teflon seat to provide this improved seal. A cooling water jacket was incorporated into the injector design to prevent deformation of the Teflon at elevated temperatures.

As discussed in Section 2.2.1, because hydrogen is a dry gas with very little inherent cooling or lubricating capability, wear of contacting parts can

cause considerable problems for injector design. Figure 2.27 shows a direct hydrogen injector design that is also hydraulically actuated, but instead of using a return spring as in Figure 2.26, this design separates the hydraulic fluid and hydrogen passages with a diaphragm fixed to the poppet valve stem. When the hydraulic fluid pressure exceeds that of the hydrogen supply pressure, the diaphragm deflects and pushes the needle down, opening the valve. The diaphragm and poppet valve are designed so that the diaphragm stress is kept to a minimum while keeping the valve closed under the 100 bar hydrogen supply pressure. This design eliminates sliding parts from the injector, thereby reducing wear. However, these researchers reported that leakage past the poppet valve was a recurring problem. They state that the seal could be improved by employing an elastomeric poppet valve seat.

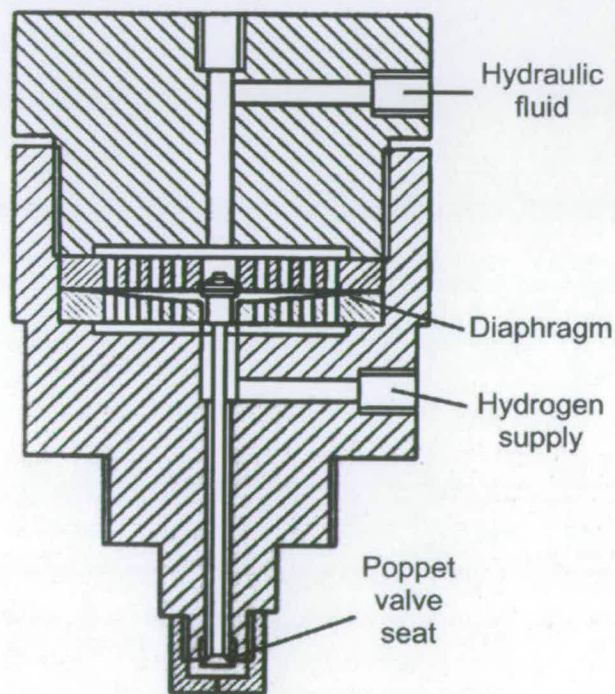


Figure 2.27: Hydraulically-Actuated Diaphragm-Spring DI Hydrogen Injector [44]

2.4.2 Engine Performance

As discussed in Section 2.4.1, direct injection offers a means of completely eliminating the problem of backfire common in pre-mixed and port injected hydrogen engines. This is because injection can be timed to occur after the inlet valve has closed, so no combustible mix is present in the inlet manifold. Pre-ignition remains a problem, however - if injection is timed early, the charge can ignite during the compression stroke ahead of the scheduled spark from hot points in the cylinder. This can lead to undesirable knocking combustion and high NO_x formation.

Furuhama [45] claims that pre-ignition can be avoided in a DI engine if the equivalence ratio does not exceed $\phi = 0.8$, but that limiting the fuel-air ratio in this way would result in power performance similar to that of a carburetted petrol engine. For the manifold injection induction method discussed in Section 2.2.2, researchers have reported that limiting ϕ to around 0.6 eliminated pre-ignition. This may suggest that the limit is extended for the DI approach. Furuhama [45] found that if cold gaseous hydrogen (-30°C , expanded from stored liquid hydrogen) is used, pre-ignition is eliminated in the full equivalence ratio range and this can increase the engine power output by 20%.

To eliminate knocking combustion, Glasson and Green [46] studied the highest useful compression ratio (HUCR) at various air excess ratios. With a compression ratio of 8, they were unable to eliminate knocking combustion for equivalence ratios greater than $\phi = 0.8$. As the mixture became leaner, the highest knock-free compression ratio increased. This suggests a trade-off between using a high compression ratio for increased thermal efficiency, and keeping the fuel-air ratio at a maximum while avoiding knock.

A disadvantage of starting injection during the compression stroke is that there is relatively little time available the fuel and air to form a homogeneous mixture. Various configurations of injector nozzle have been used by researchers to try to improve fuel-air mixing after injection [41,47]. Koyanagi *et al.* [48] captured in-cylinder images over injection and ignition in a DI hydrogen engine with two different nozzle configurations - one with eight, 0.9 mm diameter holes and one with four. The images are shown in Figure 2.28. The position of the injector and spark plug are shown in the lower left image. For the 8-hole nozzle, only one of the eight jets ignites at spark and the flame propagates through the cylinder. The other jets were observed to ignite only by contact with the propagating flame front, rather than by radiation. Similar behaviour is shown for the 4-hole nozzle, but noting the different time scales of the images, flame propagation took considerably longer.

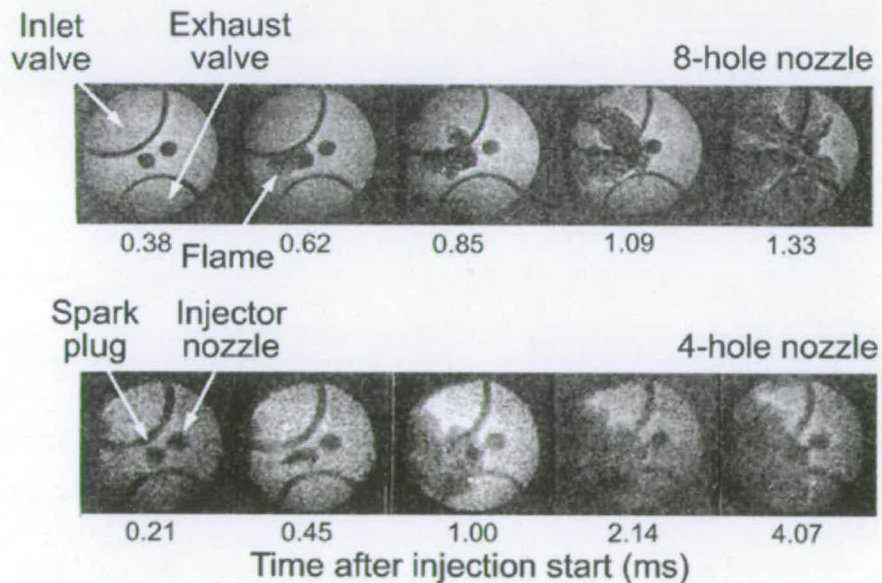


Figure 2.28: In-Cylinder Images of DI Hydrogen and Combustion, 500 RPM [48]

Martorano and Dini [41] have reported performance comparisons with various direct injector nozzle configurations. The four nozzle types are shown

in Figure 2.29, along with the injector position relative to the spark plug. Type 'a' is the standard poppet valve exit of the injector shown in Figure 2.25. Type 'b' has 21 spray tubes of 0.85 mm diameter angled so that all the jets spray outwards from the injector axis as shown. In type 'c', eight 1.2 mm diameter holes are used. Finally, for type 'd' the holes are arranged so that the jets converge as shown.

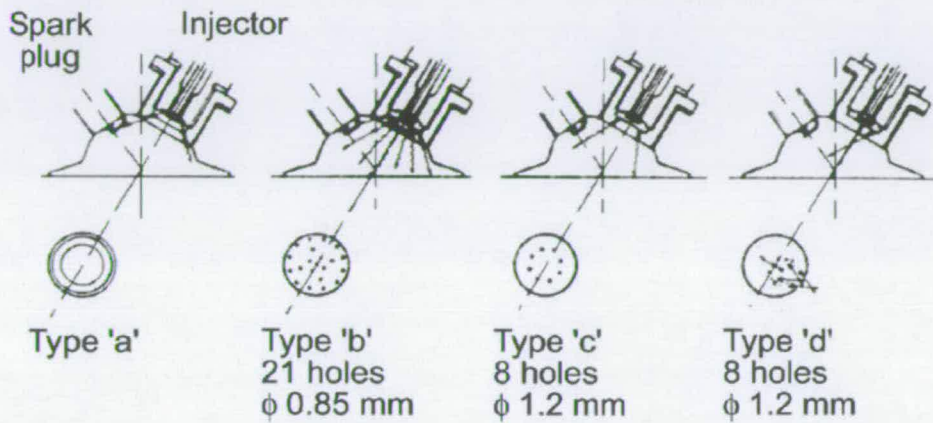


Figure 2.29: Direct Injector Nozzle Configurations [41]

Type 'd' of Figure 2.29 was shown to improve thermal efficiency by up to 20% compared with type 'b'. Results of the thermal efficiency at one engine speed are shown in Figure 2.30 where the benefit of the type 'd' nozzle is shown clearly. Also shown is the influence of the injection timing on thermal efficiency. For both nozzle configurations, as the start of injection is advanced the thermal efficiency improves significantly. This suggests that a more homogeneous fuel-air mixture is achieved with earlier injection, ensuring rapid combustion and improving Otto-cycle efficiency.

As with manifold injection, researchers typically maintain a wide open throttle with DI hydrogen engines, and control the load by varying the fuel-air ratio. Thus pumping losses are reduced and thermal efficiency can be improved compared with throttled petrol engines. Since direct injection is

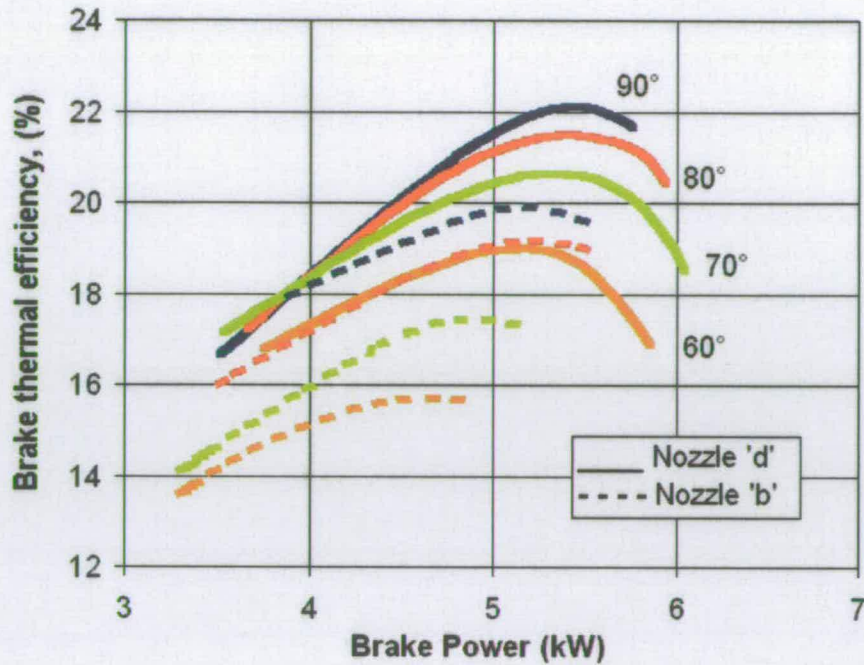


Figure 2.30: Thermal Efficiency vs Brake Power for Type 'b' and 'd' Nozzles and Injection Timing [41]

scheduled to occur after IVC, no fuel displacement of intake air occurs and the full cylinder capacity of air can be drawn in for the cycle. This means that volumetric efficiency remains high at all engine operating conditions. Yi *et al.* [49] have shown this experimentally and compared the results to a hydrogen port-injected engine. The results are shown in Figure 2.31. For the port injected engine, as the mixture becomes richer more volume fraction of fuel is required and this displaces more air. Hence the volumetric efficiency decreases for richer mixtures. For the direct injected case volumetric efficiency remains almost constant as equivalence ratio increases.

The fact that the injected hydrogen is added to the full cylinder capacity of air on injection after IVC means that the total mass of fuel-air charge is greater than manifold or port injected engines. This has been demonstrated in theory by Furuhashi and Fukuma [50], indicating that a stoichiometric

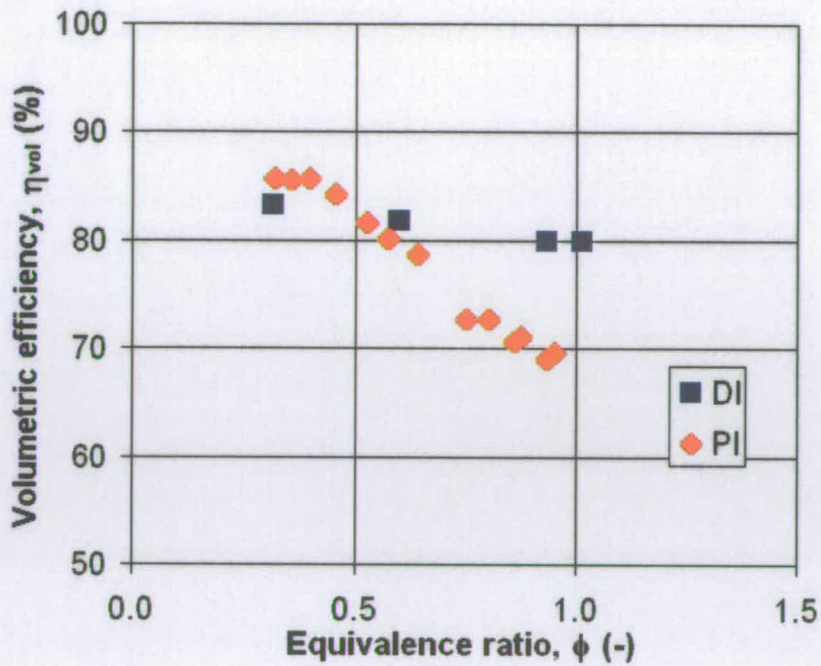


Figure 2.31: Volumetric Efficiency vs Equivalence Ratio, DI and PI Hydrogen [12]

mix of fuel and air for DI has a theoretical 40% higher energy content than carburetted hydrogen.

Several researchers have corroborated these results in practice - Billings [51] has reported that a power loss of 28.6% is typical of carburetted gaseous fuel engines compared with petrol, due to air displacement, while Meier *et al.* [34] claim a 30% increase in engine power for hydrogen direct injection compared with hydrogen external mixture formation.

Results of NO_x emissions of a DI hydrogen engine compared with carburetted petrol operation are shown in Figure 2.32. MBT spark timing is also recorded for the same engine in Figure 2.33, showing that as with MI and carburetted hydrogen operation, the MBT timing is more retarded with hydrogen than with petrol. This implies rapid combustion and pressure rise rates that cause high peak cylinder temperatures and high NO_x formation.

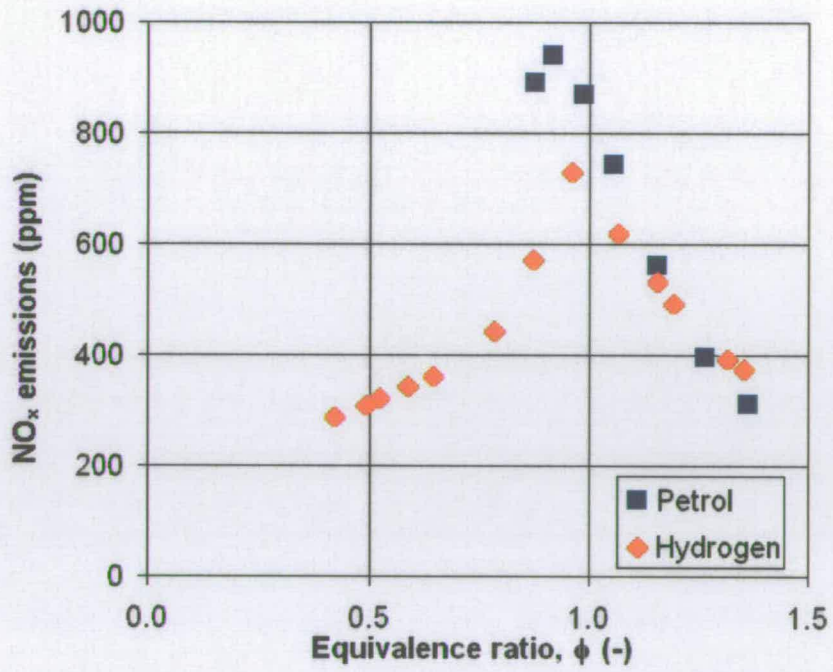


Figure 2.32: NO_x Emissions vs Equivalence Ratio - H₂ / Petrol Comparison (2.5 bar average BMEP, 1500 RPM) [43]

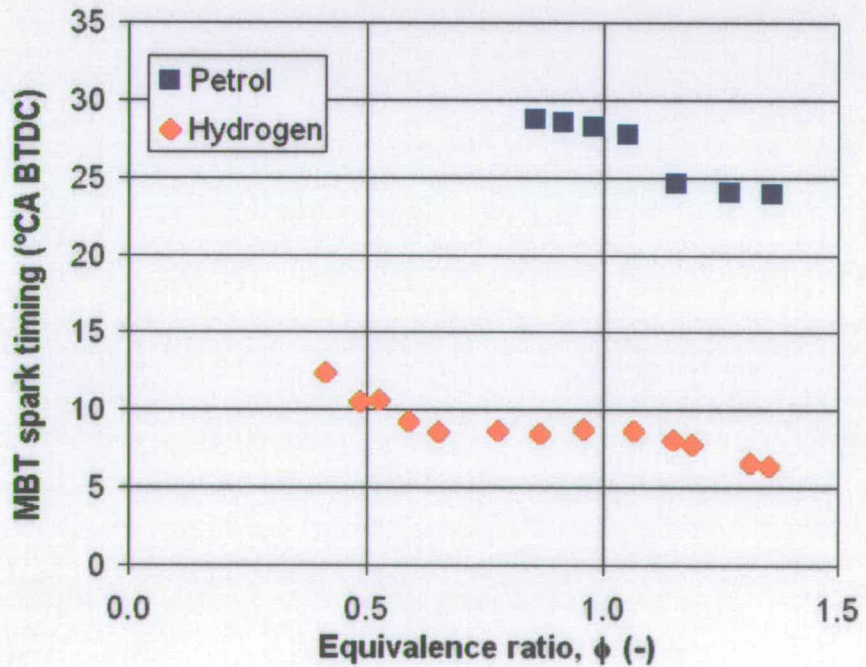


Figure 2.33: MBT vs Equivalence Ratio for a DI Engine - H₂ / Petrol Comparison (2.5 bar average BMEP, 1500 RPM) [43]

In an attempt to reduce the high peak pressures experienced with hydrogen DI, Welch and Wallace [39] have tried to induce diesel-like diffusive combustion. They attempted to emulate the ideal Diesel cycle, with constant pressure combustion as opposed to Otto constant volume combustion. Employing a continually-heated glow-plug ignition system, they injected hydrogen very close to TDC (17 to 6°CA BTDC), and continued injection during the combustion process.

The method showed a drop in thermal efficiency compared with diesel fuel operation as the injection timing was retarded. Reported levels of unburned hydrogen in the exhaust gas confirms that this could be due to incomplete combustion. However NO_x emissions showed significant reduction with later injection timings. These results are shown in Figures 2.34 and 2.35. Similar results show that this method successfully reduced the peak pressure rise rates, reducing the peak combustion temperatures and reducing NO_x formation.

2.5 Induction Method Performance

Comparison

As the previous sections show, the published literature provides many sets of performance data for engines running on pure hydrogen. These data have not previously been normalised and summarised to provide a reasonable and direct comparison between the methods of fuel induction. The following discussion addresses this shortfall and provides an original normalised synopsis of the published data.

The published literature was searched for performance results and the data were collated. Indicated mean effective pressure (IMEP) data are shown

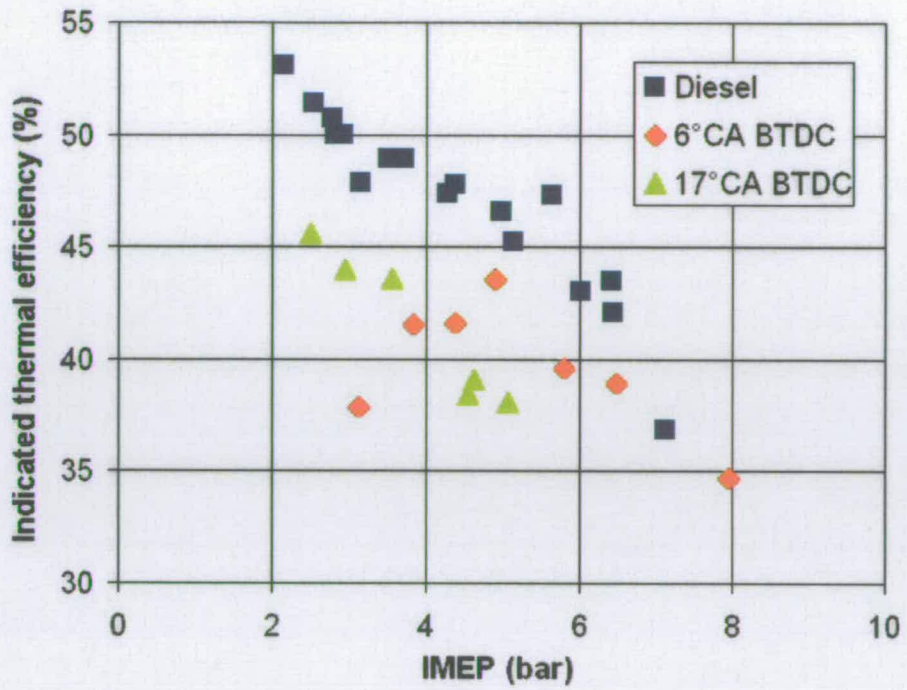


Figure 2.34: ITE vs IMEP Using the Diffusive Combustion Technique, Showing Injection Timing [39]

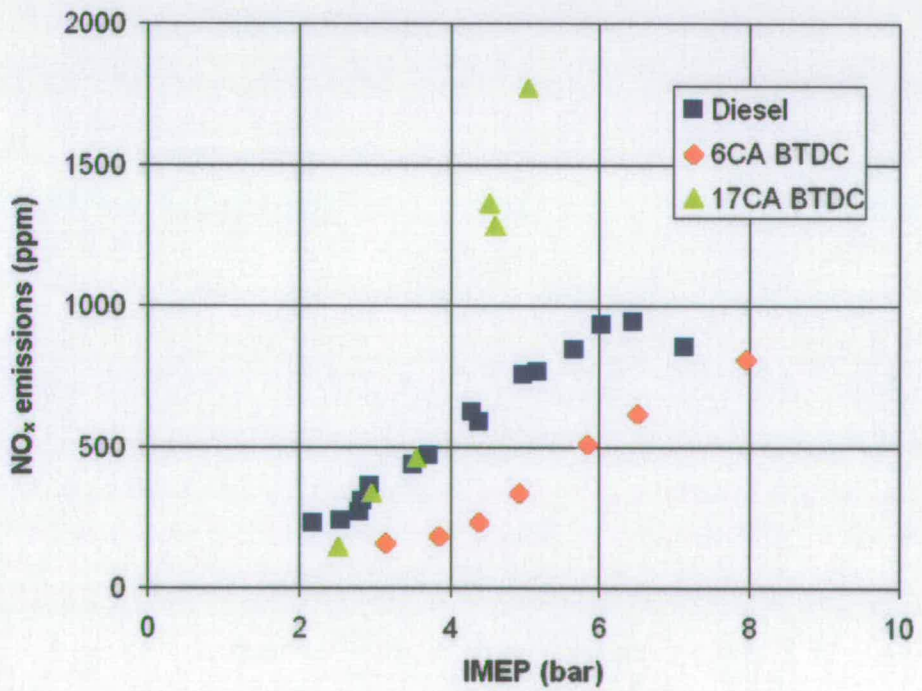


Figure 2.35: NO_x Emissions vs IMEP Using the Diffusive Combustion Technique, Showing Injection Timing [39]

in Figure 2.36. All the data shown are for single-cylinder engines, with engine capacity and compression ratio shown in the legend for each data set. A single data point is shown for a single-cylinder engine using petrol fuel for comparison [3]. Five sets of DI data, two MI and one for a carburetted engine are shown.

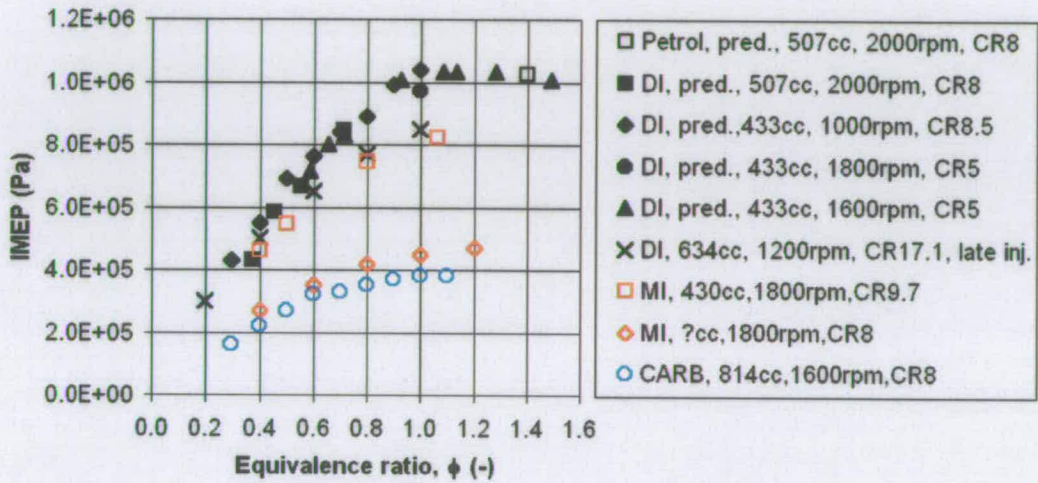


Figure 2.36: Comparison of IMEP for DI, MI and Carburetted Single-Cylinder Hydrogen Engines [3, 12, 13, 16, 39, 42, 46, 49]

For data that was published as brake mean effective pressure (BMEP), an estimate of the relationship between friction mean effective pressure (FMEP) and engine speed has been made, based on data from a similar single-cylinder engine. According to Heywood [7], components of the total FMEP are either independent of engine speed, N , proportional to speed or proportional to speed squared (a more detailed model would include components dependent on the mean piston speed). Thus FMEP can be expressed in terms of engine speed according to equation 2.2.

$$FMEP(Pa) = C_1 + C_2N + C_3N^2 \quad (2.2)$$

Figure 2.37 shows a trend line of sets of published FMEP data for several four-cylinder engines [7]. FMEP data of a single-cylinder engine is also shown [3], with data correlated by equation 2.3.

$$FMEP(kPa) = 190 + 0.1e-3N + 70e-6N^2 \quad (2.3)$$

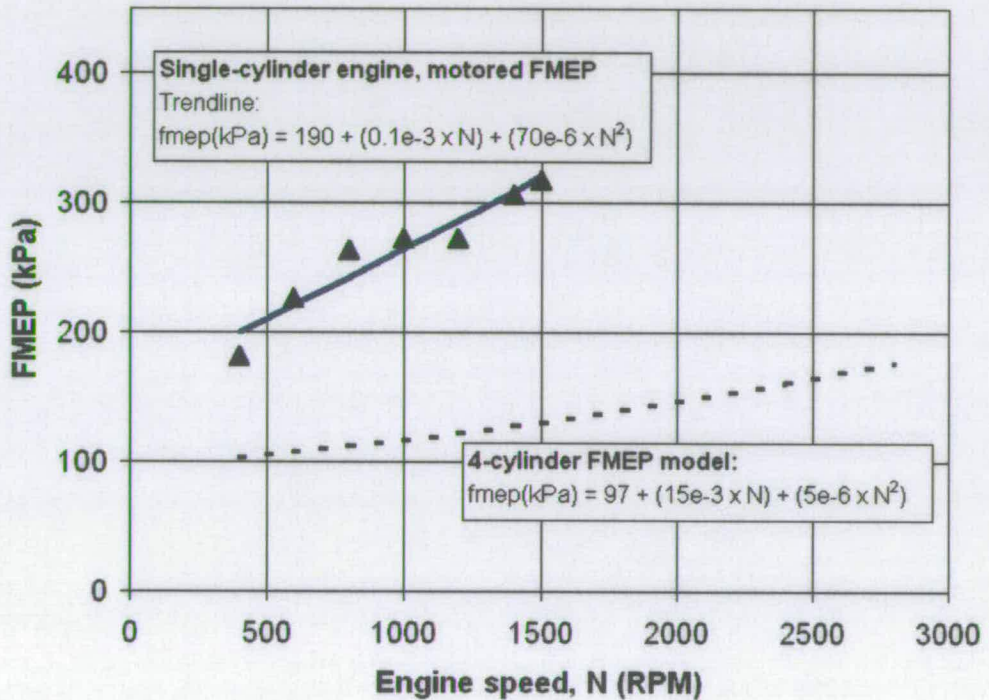


Figure 2.37: Trendline Correlation of FMEP - 4-Cylinder Engine Data and Motored Single-Cylinder Engine Data

Equation 2.3 was used to convert published BMEP data, with IMEP predicted as the sum of BMEP and estimated FMEP. These sets of data are indicated by 'pred.' in the legend in Figure 2.37. Other BMEP data shown in Figure 2.37 were derived from published torque results.

The data collected in Figure 2.36 indicate that IMEP is generally higher for direct-injected than for manifold-injected and carburetted engines. The DI set of results marked 'x' shows the lowest IMEP of the DI group. These data are from experiments with very late injection, with the injection pe-



riod overlapping the combustion period. This was in an attempt to avoid a high pressure rise rate on ignition - emulating a more diesel-like cycle - and associated high NO_x formation.

This increase in IMEP for DI over MI and carburetion is probably mostly attributable to increased volumetric efficiency, with significantly less of the inducted air being displaced by hydrogen.

Further data added to the set, particularly for carburetion, would allow more reasonable comparison of the performance characteristics of each induction method.

2.6 Summary and Discussion

2.6.1 Hydrogen Fuel Induction Methods

For all hydrogen fuel induction methods, because hydrogen-air mixtures will ignite over a wider range of equivalence ratio than petrol vapour-air mixtures, there is an opportunity to use quality engine load control. Rather than throttling the fuel-air mixture for quantity control as with a carburetted petrol engine, the mass of hydrogen inducted per cycle can be controlled to achieve the required engine load while keeping the intake air unthrottled.

For pre-mixed fuel induction, the required mass of fuel can be inducted over a large portion of the cycle; continuous supply for carburetion and during IVO for MI and PI. A drawback of DI fuel induction is that the fuel must be injected over a short portion of the cycle between IVC and TDC of the compression stroke. This leaves very little time for induction and for the fuel and air to mix completely compared with carburetion, MI and PI. Thus, a high supply pressure must be employed to achieve a high mass flow rate and momentum of the gas for adequate mixing in the time available. Researchers

also aim to achieve sonic flow through injectors so that the fuel flow rate is unaffected by changes in the downstream pressure and increases linearly with supply pressure (see Section 5.3.1). For DI, the supply pressure must be high to keep the flow above the critical pressure ratio for sonic flow.

Considering that hydrogen is stored at some initial tank pressure (e.g. 120 bar [6] to 300 bar [36] is the typical range for compressed gaseous hydrogen), this storage pressure will drop as hydrogen is consumed. If a high induction pressure is to be maintained, this implies that a pump would be needed when the storage pressure drops below that of induction. Typical induction pressures are for carburetion atmospheric to 1.5 bar, for MI 3.5 to 5.4 bar, for PI 3 to 10 bar and for DI up to 110 bar. This implies that for carburetion, MI and PI, the storage pressure can be simply deregulated to the required induction pressure over most of the tank range, but this is not the case for many DI applications.

Induction schemes that have been used by hydrogen engine researchers include commercially available natural gas injectors capable of low flow rate MI or PI, specially fabricated injectors for high flow rate DI and modified intake valve arrangements for PI. Each scheme consists of mechanical or electrical timing control (e.g. cam or crank angle sensor), an actuation device (e.g. hydraulic pump or electric solenoid) and an open/close valve (e.g. poppet or reed valve). For these types of induction valve, the use of hydrogen fuel presents a problem of wear of contacting parts. This is because hydrogen gas provides very little inherent cooling or lubrication capability compared with liquid fuels or natural gas. Poppet valve injectors are particularly susceptible to wear because they often have sliding contact between the poppet valve stem and the injector casing. This can be overcome by either using improved materials, or by using a reed valve or diaphragm design with no sliding parts.

Since hydrogen gas has a low viscosity and small molecular size compared with liquid fuels or natural gas, leakage can more easily occur through a closed injector valve. Fuel leakage is a particular problem for DI operation, where high supply pressures are used. A further consideration for DI is that the injector tip must be designed to withstand the high temperatures of the combustion chamber. This can place design constraints when additional valve seat materials are needed to achieve a leak-free seal.

2.6.2 Hydrogen Engine Performance

It has been shown that hydrogen-fuelled IC engines are highly susceptible to unscheduled pre-ignition of the fuel-air mixture. This is because the mixture will ignite over a wider range of equivalence ratio, and with a lower ignition source energy compared with petrol vapour-air mixtures. Pre-ignition is undesirable, since it leads to non-optimal engine performance and the risk of knocking combustion, and the choice of fuel induction technique can play a critical part in controlling its occurrence.

For carburetted, MI and PI operation, the presence of a combustible fuel-air mix in the intake manifold is intrinsic. Thus if pre-ignition occurs before IVC, propagation of the flame into the intake manifold, backfire, can result. These pre-mixed induction methods have been found to be susceptible to 'run-away' pre-ignition, with unscheduled combustion occurring progressively earlier in the cycle, eventually leading to backfire. For DI fuel induction, the presence of fuel in the intake manifold is eliminated and backfire can be completely avoided. Pre-ignition can still occur, however, and knocking combustion remains a risk.

The principal method employed by researchers to avoid pre-ignition has been to limit the equivalence ratio, although EGR, water injection and other

methods have also been tried successfully. For carburetion, it has been found that limiting the equivalence ratio to a maximum of $\phi = 0.5$ can prevent pre-ignition (see Section 2.1.2). Similarly, for MI the limit has been found to be between $\phi = 0.60 - 0.64$ (Section 2.2.2), and for DI, $\phi = 0.8$ (Section 2.4.2) to avoid pre-ignition. However, limiting the equivalence ratio in turn limits engine power performance and these results imply that DI offers the least compromise on performance to ensure smooth operation.

An advantage to engine performance of pre-mixed induction is that there is more time for the fuel and air to form a homogeneous mixture, and this has been shown to improve the fuel conversion efficiency in a MI engine (see Section 2.2.2). For DI operation, researchers have tried inducing swirl in the cylinder and using various injector nozzle configurations to improve charge mixing in the short time period between the start of injection and combustion.

A homogeneous mixture of hydrogen and air combusts much more rapidly than a petrol vapour-air mixture. The consequences of this are that the MBT spark timing is retarded to much closer to TDC than with petrol, and the combustion cycle more closely approximates the ideal Otto cycle, showing improved thermal efficiency as a result. However, higher peak cylinder temperatures can result, and this leads to high NO_x formation.

It was shown in Section 2.4.2 that because there is no displacement of inducted air with DI, the total charge energy can be increased by 40% over pre-mixed hydrogen induction, improving the power output. A further effect of this is that the volumetric efficiency remains high for DI throughout the full range of equivalence ratio. For pre-mixed induction, as the mixture becomes richer, more air is displaced and the volumetric efficiency drops. Since for all induction methods it is possible to apply unthrottled quality load control,

pumping losses are minimised and this improves the thermal efficiency over carburetted petrol engines.

Comparison of the reported results of brake thermal efficiency of unthrottled carburetion and MI (see Figures 2.3 and 2.14) shows that MI offers the highest gain over the same engine operating on petrol fuel. For DI, the results show (see Figures 2.30 and 2.34) that indicated thermal efficiency is lower than that of the same engine operated on diesel fuel for late injection, but that this is improved by injecting earlier and selecting an optimum injector nozzle configuration to improve charge mixing prior to ignition.

Comparison of the results of NO_x emissions of the different fuel induction techniques shows that for lean, unthrottled operation the levels are significantly lower than for petrol engines. NO_x levels show a distinct peak at equivalence ratios around stoichiometric, and for this operating condition the levels are much higher than those of petrol operation. For DI operation, it has been shown that by injecting very late in the compression stroke and continuing injection during the combustion period, more diffusive diesel-like combustion can be achieved. This has the effect of stabilising the rapid pressure rise characteristic of pre-mixed combustion and associated high NO_x levels.

Several sets of performance data of single-cylinder engines operated on hydrogen with DI, MI and carburetted fuel induction have been published. This chapter provides an original normalised summary of these data sets so that comparison of the performance of different induction methods can be reasonably made. The data has been normalised by converting to IMEP and plotted against equivalence ratio. Five sets of data for DI, two for MI and one for carburetion were used. While more data sets would allow better representation of performance, particularly for MI and carburetion, the results show that DI typically offers higher IMEP than MI and carburetion. This is

probably a result of higher volumetric efficiency for DI associated with less displacement of inducted air by the fuel compared with MI and carburetion.

Chapter 3

INJECTOR DESIGN

The discussion of Chapter 2 shows that for improved performance - avoidance of backfire, high BMEP and thermal efficiency and low NO_x emissions - the direct injection fuel induction method appears the most favourable compared with carburetion and manifold or port injection. However, the discussion also shows that high mass flow rate must be achieved, implying a need for high supply pressure. Because of this requirement, the injector open/close device needs careful design to avoid hydrogen leakage. The injector must also be designed for durability since hydrogen provides no lubricating or cooling capability. Sonic flow must also be achieved so that the mass flow rate remains unaffected by changes in cylinder pressure.

This chapter first describes a new design approach for hydrogen direct injectors. The rationale behind the approach adopted is first described in detail. The operating principle of the injector design is then outlined, highlighting particular design features that address the durability issue. An investigation into the power that would be required to actuate a hydrogen pump at the injector unit to provide elevated supply pressure is then discussed. Stress analysis of the key injector components under particular load cases is described in detail, showing simulated results of stress and fatigue.

3.1 Design Strategy

3.1.1 New Design Approach

As discussed in Sections 2.2 and 2.4, of the many injector types that have been described in the literature, two particular types have been found to exhibit low wear with hydrogen injection. Hydrogen has much less inherent cooling and lubricating capability than injected natural gas or liquid petrol, and injector wear and leakage have proved to be recurring problems [20].

As described in Section 2.4.1, one injector that was designed for DI hydrogen induction incorporates a diaphragm separating hydraulic actuation fluid and hydrogen passages, as shown in Figure 2.27. The centre of the diaphragm is fixed to the end of a poppet valve pintle, which deflects and opens the valve when the hydraulic pressure exceeds the hydrogen supply pressure. The benefit of this arrangement is that it has the effect of minimising sliding contact between parts in the injector, although some wear would occur at the poppet seat. These researchers claim that leakage through the poppet valve-type open/close device remained a problem [44] and this could be due to low seating pressure at the poppet valve face.

A further injector design that uses an annular plate was discussed in Section 2.2.1. Figure 3.1 shows a detail of the cross-section of the injector, showing that the annular plate in this case operates as the open/close valve. Actuation is provided by an electric solenoid, with the annular plate itself as the solenoid armature. In the normally closed position (as shown in Figure 3.1), the spring forces the plate down, covering the valve seat. When the solenoid is activated, the annular plate lifts up and away from the valve seat to open the valve. The reed, which is bonded to the upper surface of the plate, acts to prevent the plate rotating within the injector housing.

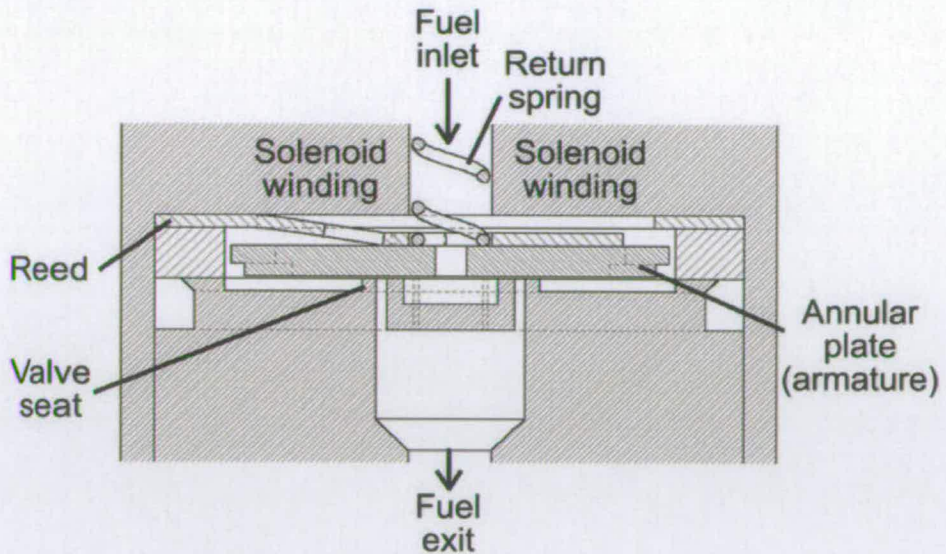


Figure 3.1: Cross-Section of an Annular Plate Injector

As discussed in Section 2.2.1, the injector shown in Figure 3.1 has been extensively tested for wear [20] with hydrogen as the working fluid. The results showed only $15\ \mu\text{m}$ -deep marks where the annular plate contacted the valve seat. Normal contact such as this would involve no sliding surface contact. This is unlike conical seat valves where the cone angle can be selected in part to provide some sliding contact between the surfaces to clear contaminants [52].

To clarify the construction of the injector shown in Figure 3.1, Figure 3.2 shows an exploded view of the injector components. The figure shows the configuration of the valve seat, showing the three arc-shaped flow orifices near the centre. These orifices are sealed by the annular plate at the raised edges of the valve seat when it is held down by the spring force.

This annular plate-type injector is specifically designed for low pressure, low flow rate MI applications and may therefore not be suitable for DI use. The electric solenoid is a ‘clapper’ type, which exhibit high holding force but low pull force on the armature. For DI applications where fast response time

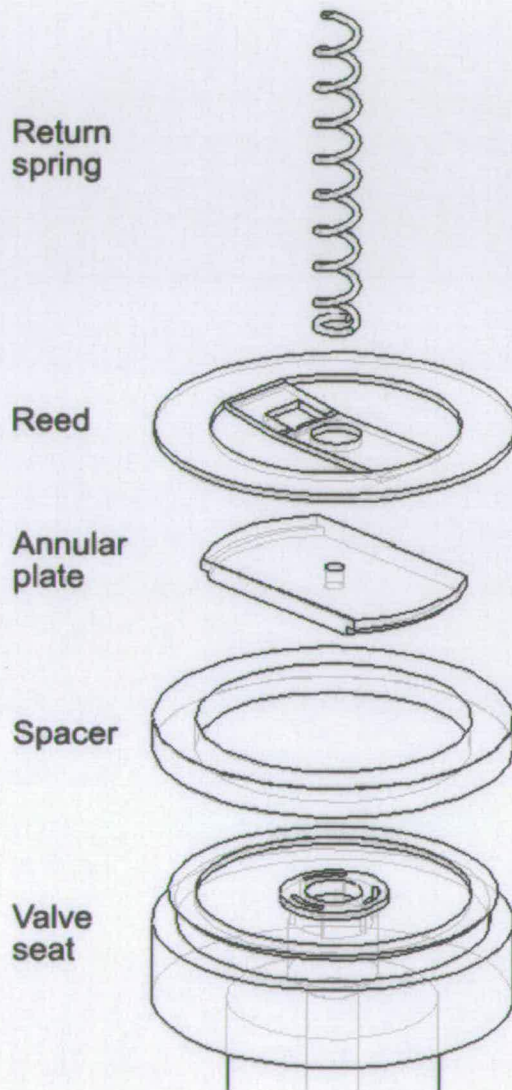


Figure 3.2: Exploded View of Annular Plate Injector Components

is needed, a 'plunger' type solenoid with higher pull force would be required. The mass of the annular plate in this type of injector may further impede the required response time. A further characteristic of this injector is that the return spring is housed within the fuel inlet path. This would lead to the flow being impeded through the inlet, and for high flow rate applications pressure losses such as this would need to be minimised.

Since these injectors - the diaphragm-type and annular plate-type - have been found to exhibit low wear when metering hydrogen fuel, characteristics of each type have been drawn on in the design proposed for this project. The new approach put forward here is to use an annular diaphragm itself as the open/close device. A cross section of the design is shown in Figure 3.3. This new design uses a valve seat arrangement of the type shown in Figure 3.2, with a cylindrical solenoid core bonded to the inner edge of an annular diaphragm, serving as the inlet tube. Figure 3.3 shows the injector in the open position; with the solenoid activated, the core is pulled up against the return spring force, and the diaphragm is deflected away from the valve seat. Fully dimensioned drawings of the injector design are given in Appendix C.

One advantage of this design is that by using a diaphragm rather than an annular plate and reed, less parts are used in the construction. Further, by locating the return spring outside the fuel inlet tube, the flow will not be impeded by its presence as with the annular plate injector. The use of a cylindrical solenoid can provide greater pulling force than a clapper solenoid, leading to fast response time. In the remainder of this chapter, theoretical proof that the injector can be designed to withstand the stress of high fluid pressure and repeated diaphragm deflection is given.

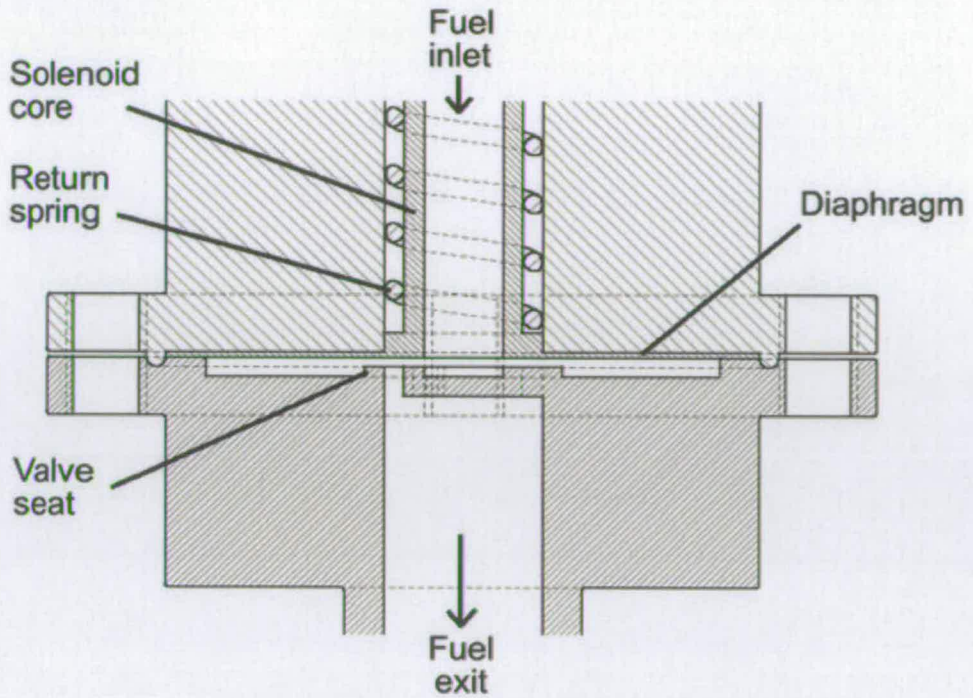


Figure 3.3: Cross Section of Diaphragm Injector Design

3.1.2 Hydrogen Compression

In Section 2.4.1, it was reasoned that for direct injection of hydrogen gas, a high supply pressure must be employed (compared with manifold injected or carburetted hydrogen) to provide adequate mass flow in the time available for injection. A consequence of this is that since the available pressure in a compressed hydrogen gas storage tank drops as hydrogen is consumed, when the storage pressure drops below the hydrogen supply pressure, a pump would be needed to maintain the desired injection supply pressure.

An initial investigation was carried out to explore the feasibility of incorporating a gas pump into an injector unit to provide this elevated pressure throughout the range of the storage tank. One advantage of incorporating the pump at the injector, as opposed to providing a remote pump supplying a number of injectors, is that the fuel supply lines may be kept at low pressure.

This would minimise the risk of leakage and other safety concerns with high pressure systems, and simplify the design of the fuel supply.

A simplified scenario of single-stage, adiabatic compression of hydrogen gas from $p_1 = 10$ bar to $p_2 = 100$ bar can be used to give an indication of the pump work that would be required for this process. The compression is assumed to be reversible and polytropic - i.e. $pV^n = \text{constant}$ where V is the instantaneous volume and n is the polytropic index of compression. The compression work is calculated as the integral of pressure with respect to specific volume, between the initial volume, V_1 , and final volume, V_2 . Using the perfect gas equation, the compression work required can be expressed by equation 3.1 [53].

$$Work = \frac{n}{n-1} mR(T_2 - T_1) \quad (3.1)$$

where m is the mass of fuel, R is the gas constant (4121 J/kg.K for hydrogen), and T_1 and T_2 are the gas temperatures before and after compression respectively. T_2 can be calculated using equation 3.2.

$$T_2 = T_1 \left(\frac{p_2}{p_1} \right)^{\frac{n-1}{n}} \quad (3.2)$$

For compression from 10 to 100 bar, using $n = 1.41$ for hydrogen and taking $T_1 = 300$ K, T_2 would equal 586 K after compression. The highest design mass of hydrogen required per cycle (for stoichiometric operation and cylinder volume $0.507 \times 10^{-3} \text{ m}^3$) has been calculated as 0.019 g (see Appendix A). From equation 3.1, this implies that 77 J of energy would be required to compress this mass according to equation 3.1.

This energy requirement can be expressed as a percentage of the total fuel energy inducted per cycle. Taking the mass of hydrogen inducted per cycle as 0.019 g, and using the lower heating value of hydrogen, $Q_{LHVH_2} = 120 \times 10^6 \text{ J/kg}$

[7], this implies that the fuel energy per cycle would be 2.3 kJ. The 77 J required for compression in a pump-type hydrogen injector would therefore take 3.4% of the total fuel energy inducted per cycle.

Indicated pump power can be calculated using mass flow rate, rather than hydrogen mass in equation 3.1. At an engine speed of 6000 RPM, the corresponding cycle-averaged hydrogen mass flow rate would be 0.32 g/s. Using equation 3.1, this would imply that the average indicated power required of a hydrogen pump unit would be 1.3 kW. This corresponds to 0.5 bar MEP; 5% of the 10 bar shown for typical IMEP at $\phi = 1$ in Figure 2.36 for slower engine speeds of between 1000 and 2000 RPM.

Mechanical, fluid and thermal losses have not been considered in this simplified analysis of gas compression. Also, the temperature at the start of compression is arbitrarily taken as $T_1 = 300$ K, where this could be affected by gas expansion from storage pressure, or conducted heat from the engine head. Depending on the type of device used, the actual power required for compression of hydrogen gas could be considerably higher than 1.3 kW. It is expected that wear of contacting parts would need careful consideration in the design of an injector pump unit. Avoiding hydrogen leakage would also be a challenging design aspect, and would require a complex pump design. Because of these complications, the possibility of incorporating a pump into the injector unit was not investigated further.

3.1.3 Injector Flow Area - Pressure Relationship

As a design strategy, some basic assumptions will be made about the flow requirements of the injector. These assumptions are biased towards designing for a 'worst case' operating condition - capable of providing the highest mass flow rate that may be required, and with the highest cyclic injection

frequency. From compressible flow theory (see Section 5.3.1), a result can be derived that expresses the mass flow, \dot{m} through a convergent-divergent nozzle in terms of the supply conditions, p_0 and T_0 , effective flow area, A_e and gas properties, (equation 3.3) [18, 22].

$$\dot{m} = \frac{A_e p_0}{\sqrt{RT_0}} \sqrt{\gamma} \left(\frac{2}{\gamma + 1} \right)^{\frac{\gamma+1}{2(\gamma-1)}} \quad (3.3)$$

As shown in Appendix A, the flow rate through a direct hydrogen injector, at the 'worst case' engine operating condition (6000 RPM, 30°CA injection duration, stoichiometric fuel-air ratio ($\sigma = 1$) and cylinder volume $0.507 \times 10^{-3} \text{ m}^3$), must be 23 g/s during the injection period. Using this target highest mass flow rate, equation 3.3 can be rearranged to express the required effective flow area, A_e , in terms of the mass flow rate, \dot{m} , supply pressure, p_0 , and temperature, T_0 (300 K), gas constant, R (4121 J/kg.K) and ratio of specific heats, γ (1.41).

Figure 3.4 shows the required effective flow area as a function of supply pressure. The figure shows one relationship assuming a short injection duration of 0.83 ms, corresponding to 30°CA at 6000 RPM. A second relationship with an injection duration of 60°CA over which to inject the required mass of fuel is also shown. Figure 3.4 shows that if the injection duration can be increased - i.e. started earlier in the compression stroke, while avoiding problems of pre-ignition and maintaining the same mass flow rate - the required effective flow area is reduced for the same supply pressure.

A small flow area would be preferable, since the quenching gap of a hydrogen flame has been found to be 0.64 mm. This is small compared with the quenching gap of methane or petrol vapour flames - both approximately 2 mm [4]. If the flow orifice gap is kept smaller than the quenching gap, this would prevent the flame from propagating back into the injector. This leads

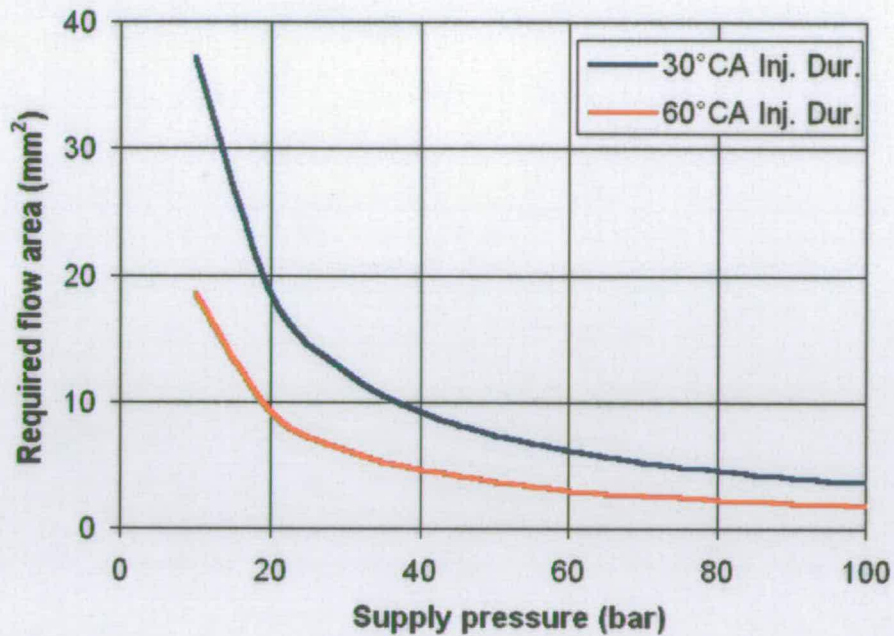


Figure 3.4: Effect of Supply Pressure on Required Effective Flow Area for Two Injection Duration Cases

to a practical maximum flow area, and therefore a minimum supply pressure that must be employed to achieve the required mass flow rate. From the graph shown in Figure 3.4 the supply pressure must be greater than 40 bar if the flow area is to be kept under 10 mm² at the highest design fuel mass flow rate. In reality, a practical maximum flow area would also be imposed by fitting the injector nozzle into the cylinder head between the inlet and exhaust valves and spark plug.

The injector design drawings shown in Appendix C suggest a minimum geometric flow area of 6.28 mm² (see Section 4.1.3). Rearranging equation 3.3 to express the required supply pressure as a function of mass flow rate and minimum flow area, this suggests that 58 bar supply pressure would be required to deliver hydrogen at the highest design mass flow rate (see Appendix A).

This calculated supply pressure directly influences the choice of return spring used in the design. The contact pressure between the diaphragm and valve seat when it is forced shut by the spring would need to be greater than the hydrogen supply pressure to avoid leakage of hydrogen when the injector is closed. The seat area calculated from the dimensions given in Appendix C is 48 mm^2 . This implies that for the contact pressure to exceed 58 bar, the spring should provide a minimum of 280 N force on the diaphragm.

3.2 Design Calculations

3.2.1 Diaphragm Deflection and Stress

Design calculations have been made to assess the effect of forces acting on the diaphragm. The general case of a uniform unit annular line load, w (N/m), acting at radius r_0 from the centre, is illustrated in Figure 3.5. 'a' and 'b' are the outer and inner radii respectively, with subscripted 'a' and 'b' values applying at these points. Q is the unit shear force, M_r is the unit radial bending moment, θ is the change in slope, and y is the vertical plate deflection.

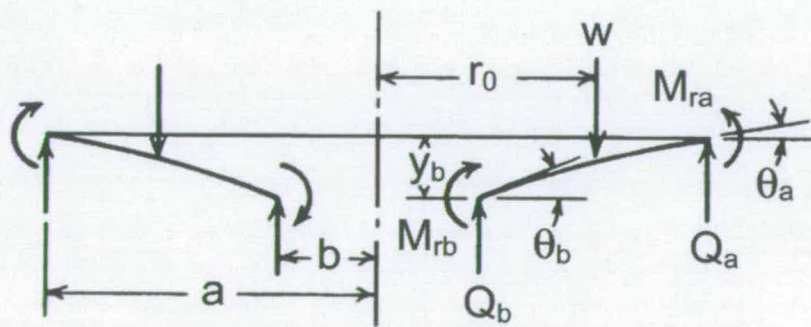


Figure 3.5: General Case of Annular Line Loading on a Plate [54]

Roark [54] provides equations for the radial bending stress and deflection of an annular plate for the case shown in Figure 3.5. For the specific support case of fixed outer edge and free inner edge, the equations are given in Appendix B. The equations have been used to assess the effect of the dimensions of outer radius ‘ a ’ and the diaphragm thickness, ‘ t ’ on the deflection and bending stress under an applied load.

Table 3.1 summarises the parameters used in the analysis. Material properties of moduli of elasticity and rigidity are those of high-strength steel [55].

Parameter and units	Quantity
Inner radius, b	2 mm
Acting radius of annular line force, w, r_0	2 mm
Annular line force magnitude, W	50 N
Modulus of elasticity, E	2e11 N/m ²
Modulus of rigidity, G	7.7e10 N/m ²

Table 3.1: Injector Diaphragm Design Parameters

Figures 3.6 and 3.7 show surface plots of the deflection, y_b , of the diaphragm at the inner radius, and the maximum bending stress, σ , respectively, as functions of the outer radius, ‘ a ’, and the thickness, ‘ t ’. The applied force, w (N/m), used in the calculations was obtained by dividing the line force magnitude, W , by the circumference at the point of application.

The dimensions of the diaphragm shown in Appendix C are outer radius 13 mm (to the edge of the clamp), thickness 0.25 mm and required deflection 0.5 mm to fully closed position.

The data plotted in Figure 3.6 imply that for this geometry, under a 50 N applied force, the deflection would be 0.67 mm. The calculated corresponding radial bending stress is 420 MPa.

The results in Figure 3.7 show that the diaphragm thickness has the most effect on bending stress. Also shown is that there is a trade-off between deflection and stress; stress increases as deflection increases. A practical min-

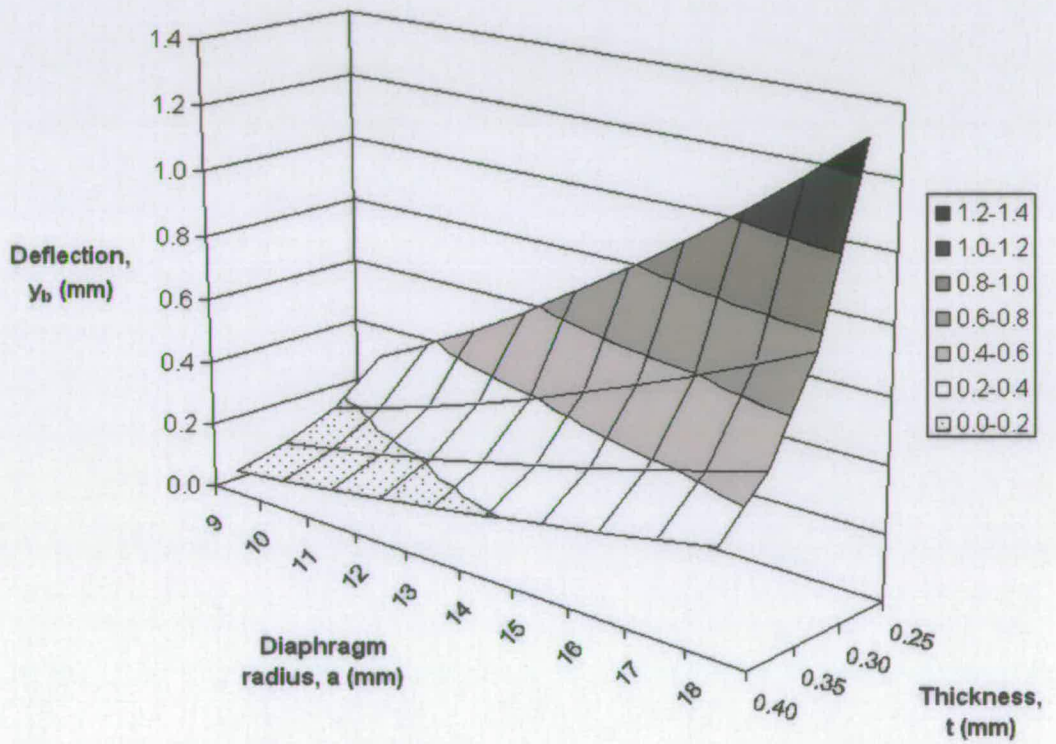


Figure 3.6: Surface Plot of Diaphragm Deflection as a Function of Outer Radius and Thickness - 50N Applied Force

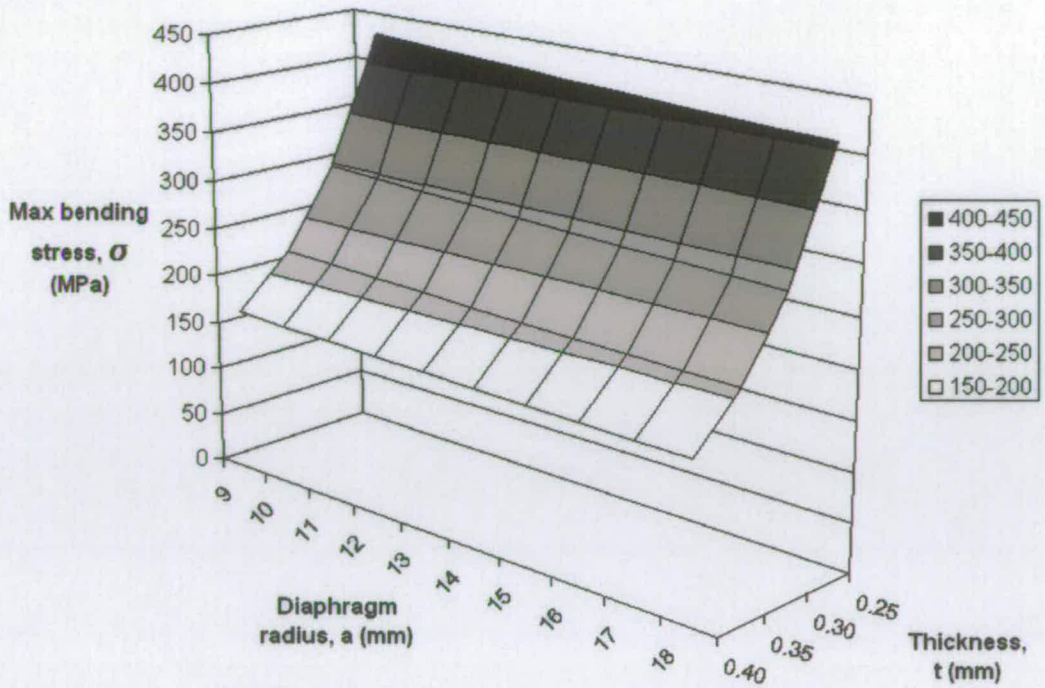


Figure 3.7: Surface Plot of Diaphragm Maximum Bending Stress as a Function of Outer Radius and Thickness - 50 N Applied Force

imum deflection would be imposed to allow gas flow with negligible surface effects, and this implies a minimum stress. Figures 3.6 and 3.7 suggest that by increasing the outer radius, the diaphragm thickness can be increased while maintaining the required deflection, and therefore the maximum bending stress can be reduced. However, a practical maximum outer radius would be imposed by the need to fit the injector into the cylinder head.

3.2.2 Fatigue

A further consideration in the design of the injector diaphragm is the 'endurance limit' or 'fatigue limit' under cyclic loading. For a maximum stress level in cyclic loading, brittle failure can occur after a certain number of cycles. For non-ferrous metals, the fatigue limit is defined as the maximum applied cyclic stress corresponding to failure after a specified number of cy-

cles. For steels, the endurance limit is defined - for maximum stresses below the endurance limit, fatigue failure will not occur [55,56].

A typical graph of maximum cyclic stress against number of cycles to failure (S-N curve) for steel is shown in Figure 3.8. The figure shows that for stresses below the endurance limit, failure does not occur.

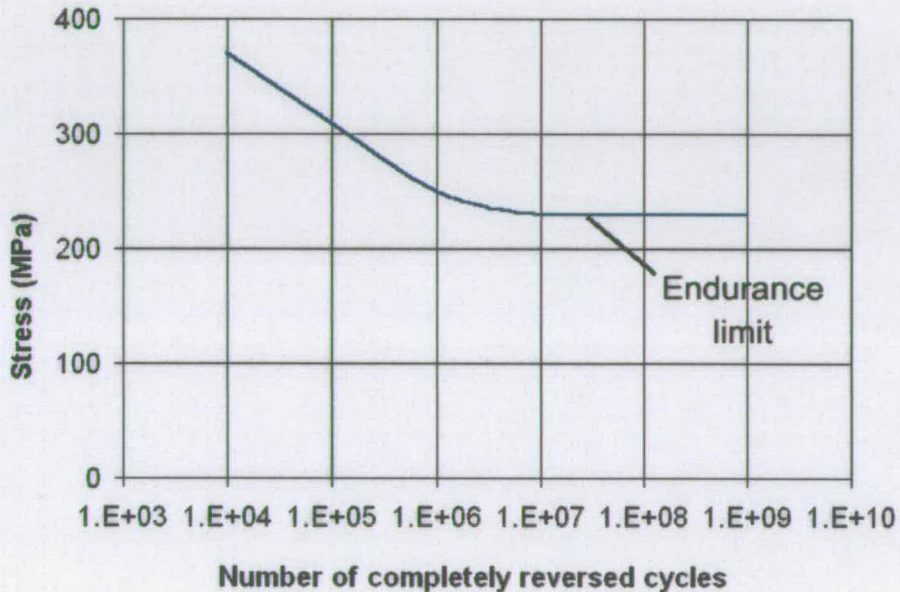


Figure 3.8: Example Endurance Limit of Steel Under Cyclic Loading: Maximum Cyclic Stress vs Number of Cycles [55]

For low carbon steels, the endurance limit is approximately half that of the ultimate tensile strength (UTS) of the material [55]. Typical UTS of high-strength steels are 400-480 MPa and for stainless steels between 655-860 MPa.

However, spring steels exist that exhibit higher yield strength and endurance limit. In a study on fatigue, Lee *et al.* used heat-treated spring steel with a yield strength of 1755 MPa and tensile strength 2149 MPa at 300°C [56]. Their results indicated the endurance limit stress was 660 MPa.

3.2.3 Stress Under Pressure - Hoop Stress

Further analysis has been carried out to assess the effect of elevated pressure on the tensile stress (hoop stress) in the cylindrical inlet tube of the injector. A simple result derived from the theory of stresses in thin-walled cylindrical pressure vessels is expressed by equation 3.4 [55].

$$\sigma = \frac{pr}{t} \quad (3.4)$$

where σ is the tensile stress, p is the gauge fluid pressure in the vessel, r is the radius of the pressure vessel wall, and t is the thickness of the wall. It can also be shown that the hoop stress described in equation 3.4 is twice the value of the longitudinal stress in the vessel wall [55].

For example, for a gas pressure of 100 bar, radius 2 mm and wall thickness 1 mm (see Appendix C), the tensile hoop stress would be 20 MPa.

3.2.4 Stress and Deflection Modelling

An injector component model developed with the SolidEdge package was used to create a CAE model of stress and deflection of the diaphragm. Consideration of a more complex geometry and load case model is possible with CAE modelling. This section provides model data for comparison with results using the equations outlined in Section 3.2.1. The CAE package used was ANSYS DesignSpace, which has the capability to import geometry data directly from SolidEdge Part (*.par) files.

The imported SolidEdge geometry was similar to the diaphragm and bonded solenoid core shown in Appendix C. The first support case considered was of fixed outer edge. The injector design drawings of Appendix C show the 30 mm diameter diaphragm clamped between the valve seat and cap, such that the clamped edge is at 26 mm diameter. Thus a modified SolidEdge

model of the component was created with 26 mm diameter diaphragm, and the effect of the clamp was modelled in DesignSpace as a fixed outer edge. The thickness of the diaphragm used in this model was 0.5 mm.

The material was defined as steel in DesignSpace, and a nominal force of 250 N was applied in the model to the surface that would be in contact with the return spring. The support and force environment is shown in Figure 3.9.

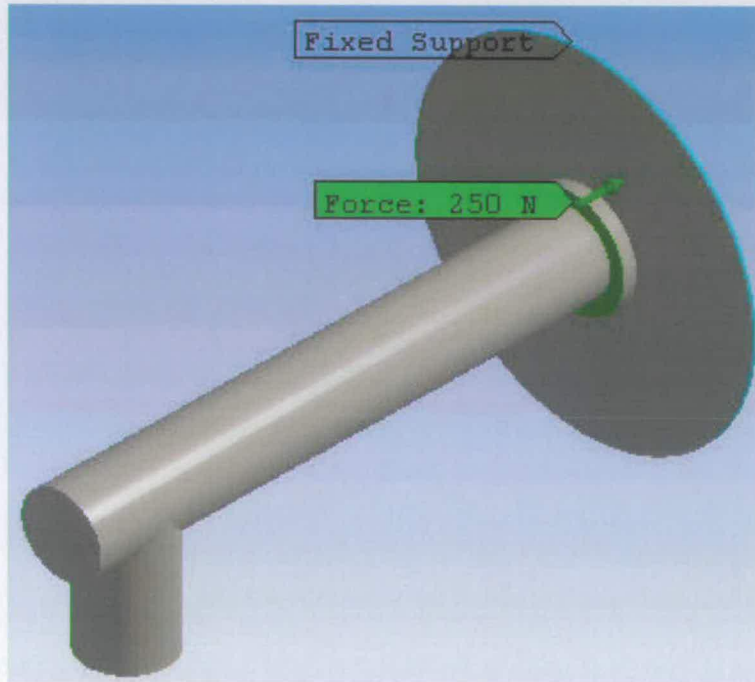


Figure 3.9: ANSYS DesignSpace Diaphragm Model: Fixed Edge Case Showing Force Applied

Figure 3.10 shows a DesignSpace generated plot of deflection for the fixed edge case with 250 N load applied. The figure shows the scale of the contours, showing that the calculated maximum deflection is 0.468 mm. Using the outer radius and thickness dimensions and applied force with the equations of Section 3.2.1 indicates a calculated maximum deflection of 0.420 mm.

A DesignSpace generated plot of shear stress for this load and support case is shown in Figure 3.11. The stress is plotted in one direction only,

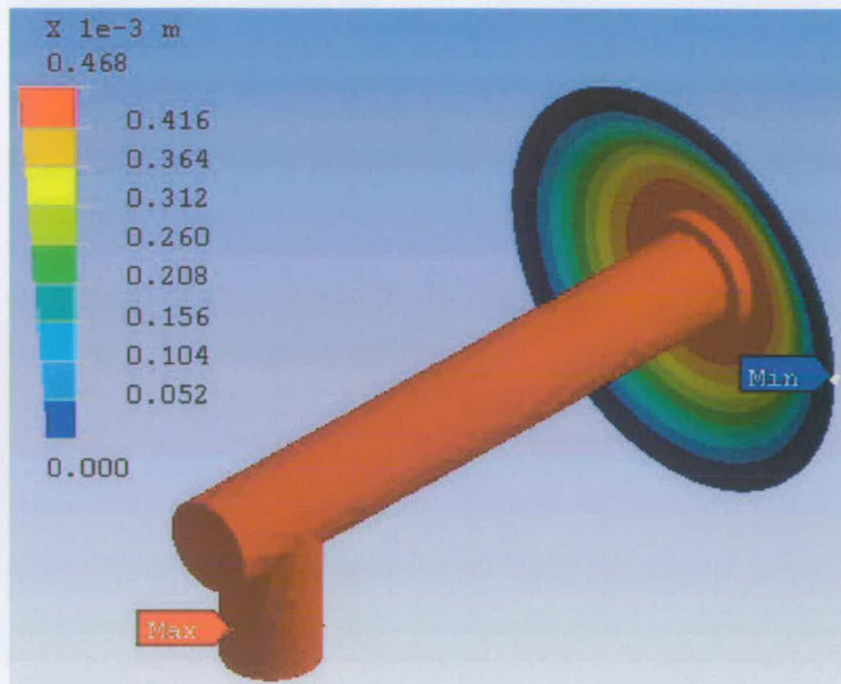


Figure 3.10: Diaphragm Model Fixed Edge Case: Deflection Plot

normal to the injector axis. The scale of the contours is shown, indicating that the maximum shear stress occurs at the fixed edge, and is 400 MPa. Using the equations for stress outlined in Section 3.2.1 indicates calculated maximum stress of 522 MPa.

It was thought that a more accurate model could be developed to reflect the fact that the diaphragm is clamped between the valve seat and cap, rather than having a true fixed edge. To investigate the effects of radial freedom of movement of the diaphragm between these components, a further simplified model was created and the cross section is shown in Figure 3.12. The figure shows that a single-piece clamp component was used to model the effect of the valve seat and cap. The diaphragm shown has outer diameter 30 mm and thickness 0.5 mm.

In this model the support of fixed edge was applied to the outer edge of the clamp, and a 250 N force was applied where the return spring would

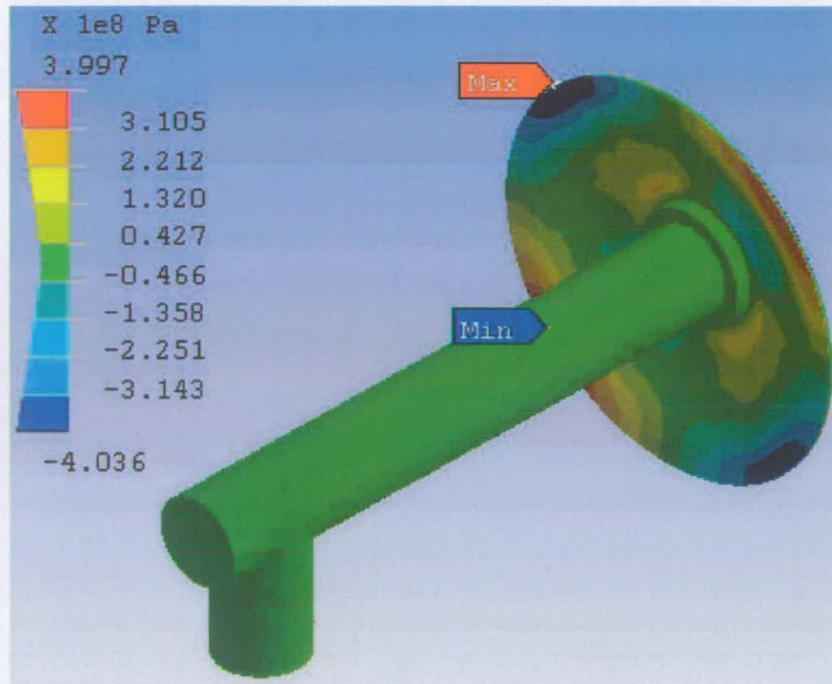


Figure 3.11: Diaphragm Model Fixed Edge Case: Shear Stress Plot

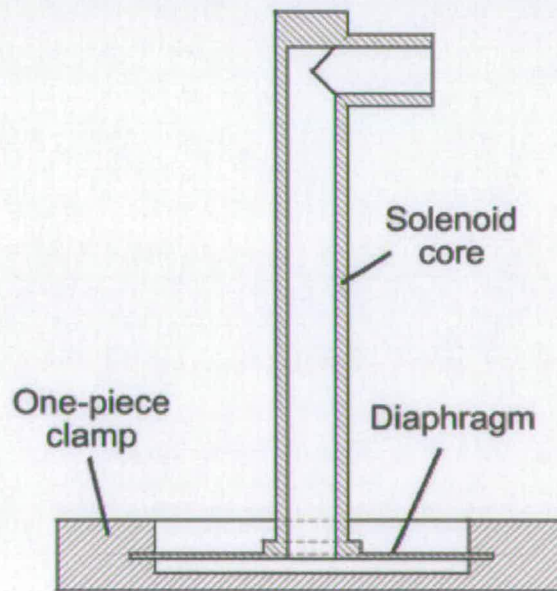


Figure 3.12: Diaphragm Model Clamped Edge Case: Geometry Cross Section

contact the diaphragm. The support and applied force environment is shown in Figure 3.13.

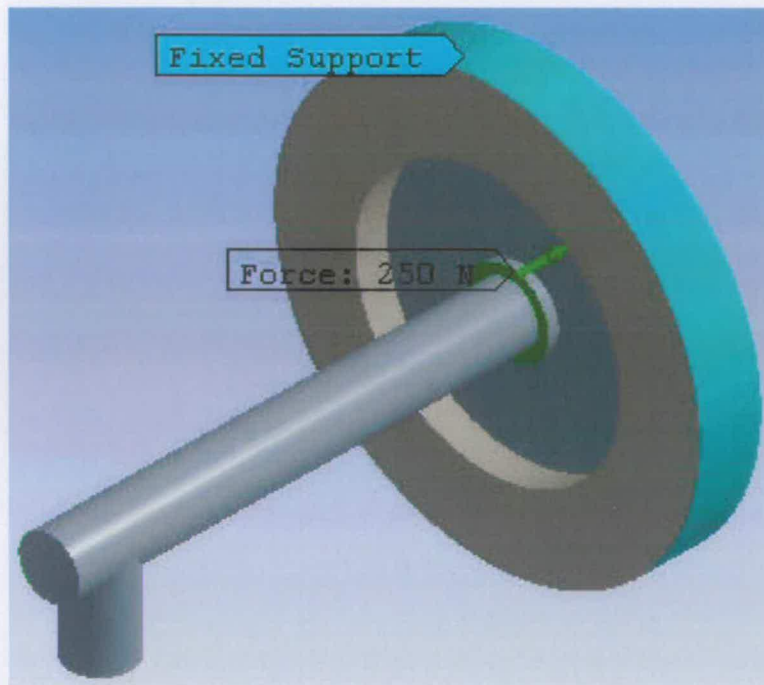


Figure 3.13: Diaphragm Model Clamped Edge Case: Support and Applied Force Environment

Figure 3.14 shows a plot of deflection under this support and applied force case. The scale of the contours is also shown. The results show that the calculated maximum deflection is 0.364 mm.

A plot of modelled stress is shown in Figure 3.15, including the scale of the plotted contours. Here, the maximum stress is calculated as 236 MPa.

The model was also used to calculate radial deflection of the diaphragm at the edge of the clamp. The results indicate calculated deflection in this direction to be $7.3 \mu\text{m}$.

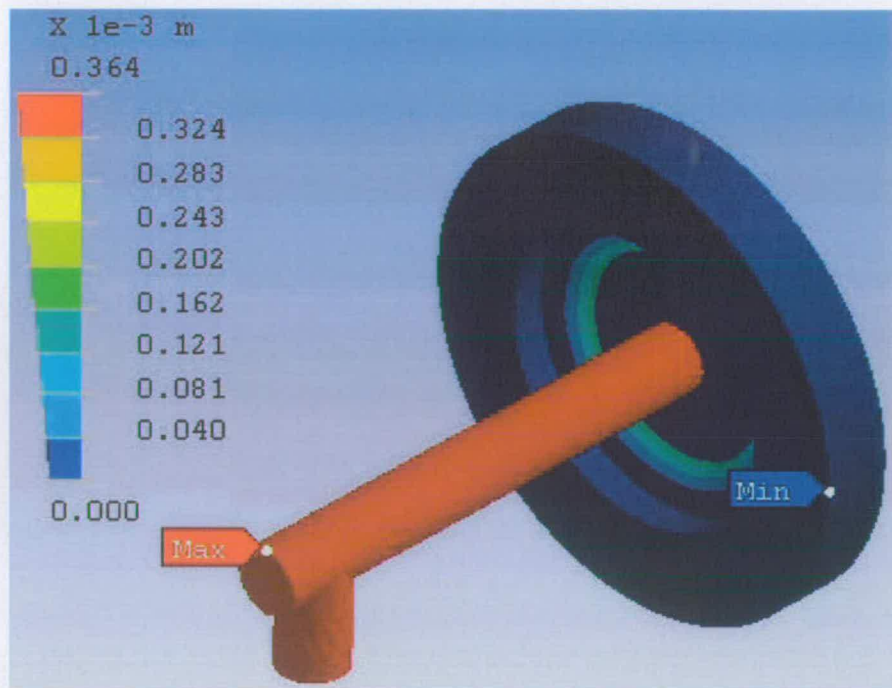


Figure 3.14: Diaphragm Model Clamped Edge Case: Deflection Plot

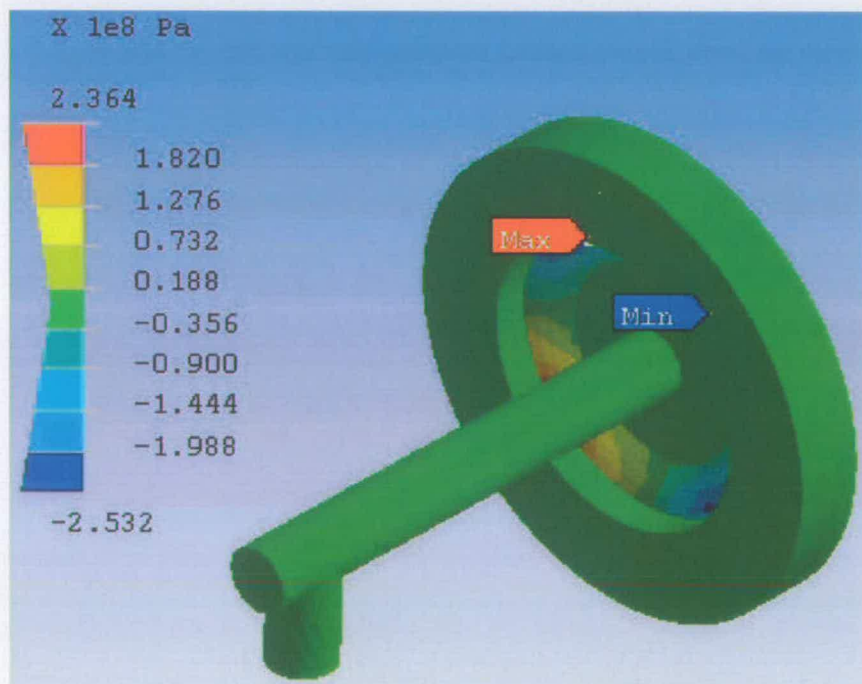


Figure 3.15: Diaphragm Model Clamped Edge Case: Stress Plot

3.3 Discussion

It has been shown that unlike liquid fuels or natural gas, hydrogen gas has very poor lubricating and cooling capability and wear and failure of contacting injector parts has proved to be a recurring problem. From the discussion in Chapter 2, injectors that incorporate a diaphragm or reed minimise sliding contact between injector parts, and therefore can overcome the problem of wear.

An existing commercial injector designed for manifold injection of natural gas that uses a reed and annular plate forms the basis of the new design. A further existing design that uses a deflecting diaphragm with a poppet valve fixed to the centre also forms the background to the design, since this type has also been found to exhibit low wear by minimising sliding contact between parts.

The new approach put forward in this report is to combine features of these two existing injectors to provide a unit capable of high pressure, high flow rate direct injection, while avoiding problems such as leakage and low response time. Rather than an annular plate and reed, the new design incorporates a steel annular diaphragm as the open/close valve itself. This would lead to fewer parts being used in the construction. A cylindrical solenoid, with the solenoid core bonded to the inside edge of the annular diaphragm provides actuation of the valve. Use of a cylindrical solenoid can provide higher pull force than the 'clapper' type solenoid used in the annular plate injector. Further, the new design houses the return spring outside the fuel inlet tube, avoiding the flow being impeded, as with the annular plate injector. Dimensioned drawings of the design are given in Appendix C.

Because hydrogen fuel must be delivered at pressure, an investigation was carried out into the possibility of incorporating a pump device in the

injector unit design. Particularly for direct injection, compression of the gas would be needed when the pressure in the storage tanks dropped below the required injection pressure. Incorporating a pump in the injector unit itself would eliminate the need for high pressure fuel supply lines, and associated safety concerns.

The simplified analysis of single-stage compression of hydrogen from 10 to 100 bar indicated that the gas temperature would be raised to 586 K and 77 J of energy per cycle per cylinder would be required over the process. This would constitute 3.4% of the total fuel energy supplied to the cylinder per cycle. At the top engine speed condition of 6000 RPM, up to 1.3 kW indicated power would be required to maintain cyclic compression. This corresponds to 0.5 bar MEP. In this analysis, mechanical, fluid and thermal losses were not considered, and the actual power required would be higher than this and depend on the type of device used. The design of a leak-free, durable pump unit is anticipated to be highly complex and was outwith the scope of the project.

From compressible flow theory, analysis of the relationship between gas supply pressure, mass flow rate and minimum geometric flow area was carried out. Using a highest design mass flow rate as a fixed parameter, the required flow area drops as the injection pressure increases as would be expected. In reality, a practical maximum flow area is imposed by packaging the injector nozzle between the inlet and exhaust valves in the cylinder head, and by ensuring that the flow orifice gap is less than the quenching gap of a hydrogen flame (0.64 mm). This latter constraint ensures that the flame can not pass into the fuel supply. Therefore to provide the highest design fuel mass flow rate, with a practical maximum flow area imposed, this implies that a minimum fuel supply pressure must be employed. For example, the analysis suggests that the supply pressure must be greater than 40 bar if the

flow area is to be kept under 10 mm^2 at the highest design fuel mass flow rate. The injector design drawings shown in Appendix C suggest a minimum geometric flow area of 6.28 mm^2 (see Section 4.1.3). This implies that 58 bar supply pressure would be required to deliver hydrogen at the highest design mass flow rate of 23 g/s.

To avoid leakage of hydrogen through the closed injector, the contact pressure between the diaphragm and valve seat would need to be greater than the supply pressure. Analysis shows that the return spring must provide a minimum of 280 N to satisfy this requirement.

Analysis of the stress and deflection of the annular steel diaphragm has been carried out using accepted mechanics equations. A general case of a fixed outer edge, with an annular line load applied at the inner edge to represent the effect of the bonded solenoid core, was investigated. Assuming an inner radius of 2 mm and an applied load of 50 N, the effect on the stress and deflection of the outer radius (9-18 mm) and plate thickness (0.25-0.40 mm) was assessed.

The analysis shows that the plate thickness has the greatest effect on the stress. The results also show that there is a direct trade-off between stress and deflection. With the dimensions shown in Appendix C of outer radius 13 mm and thickness 0.25 mm, the results show that the deflection would be 0.67 mm and the maximum radial bending stress 420 MPa. This is close to the ultimate strength of high-strength steel, which is typically in the range 415 - 480 MPa, and higher than the yield strength range of 290 - 345 MPa [55].

The calculations show that by increasing the outer radius, the diaphragm thickness can be increased while maintaining the required plate deflection. In turn, a greater plate thickness indicates lower bending stress. However, a practical maximum outer radius is imposed by the constraints of packaging the injector into the cylinder head.

Fatigue failure would occur for an applied cyclic maximum stress greater than the endurance limit of the material. This endurance limit stress is typically approximately half the ultimate strength of the material. The calculated diaphragm bending stress of 420 MPa would suggest that high-strength steel is not suitable for the diaphragm material. It has been shown, however, that heat-treated spring steel can exhibit an endurance limit of 660 MPa, and this type of steel may be more suited to the application. Hoop stress in the injector inlet pipe, under a gas supply pressure of 100 bar, has been calculated as 20 MPa; approximately 5% of the ultimate tensile strength of steel.

The ANSYS DesignSpace CAE package has been used to model deflection and stress of the injector diaphragm component, for comparison with the results using accepted mechanics equations. A modified model geometry of 26 mm diameter and 0.5 mm diaphragm thickness, with fixed edge support and 250 N load was used. The maximum deflection indicated by the model was 0.47 mm; 12% higher than the deflection calculated using the accepted equations of 0.42 mm.

CAE modelled maximum stress under this load and support case was 400 MPa; 23% lower than the result obtained by using the accepted mechanics equations of 522 MPa. Discrepancies between these results may be due to the slightly different geometry involved at the point of application of the force. In the DesignSpace model, the complete geometry of the diaphragm with the solenoid core bonded to its inside edge is used, with the load applied to the return spring contact surface. For the analysis using mechanics equations, an annular line load applied at a radius equal to that of the radius of the diaphragm annulus is modelled.

A more accurate model of the injector design was created, simulating the effect of clamping the diaphragm between the valve seat and the injector cap, rather than as a fixed edge. This arrangement would allow some freedom of

movement in the radial direction. With this modelled geometry, a fixed edge support was applied to a single-piece component, clamping the outer edge of the diaphragm. A 250 N force was applied to the return spring contact surface. For this case the modelled deflection was 0.36 mm; 23% lower than the fixed-edge model deflection.

Maximum stress for the clamped diaphragm model was calculated as 236 MPa, and this was 41% lower than the fixed-edge model results. The difference between these results may be due to modelling freedom of radial deflection in the case of the clamped diaphragm model. The model results indicate calculated radial movement of $7.3\ \mu\text{m}$ at the edge of the clamp.

Chapter 4

CFD MODEL

DEVELOPMENT

This chapter describes the geometry and mesh generation process of the three key models used in the analyses of Chapter 5. The type of geometry used, dimensions and co-ordinates of each model, geometric characteristics and differences to real geometry, anticipated locations of flow field features, mesh features and generation and finally the boundary types used are each considered in turn. Model parameters including fluid properties, boundary conditions and solver settings are detailed. A discussion on the methods employed to obtain a converged solution is also given.

4.1 Model Geometry and Mesh

The following subsections describe the geometry and mesh models developed for the CFD cases investigated in Chapter 5. All geometry and mesh generation was carried out using the Gambit pre-processor. In all cases, axi-symmetric geometry was used. Geometry was defined using vertices and

edges (rather than volume elements), then defining the outline as a face, meshing and defining the axis of symmetry along one boundary.

Triangular-scheme mesh generation was used for all models as this was found to give more stable mass continuity convergence compared with quad-type meshing.

4.1.1 Conical-Seat Injector

To assess the effectiveness of CFD in modelling trans-sonic compressible flows, a model of hydrogen flow through a convergent-divergent nozzle was developed. Actual flow rate-pressure data of hydrogen flow through a Bosch natural gas injector is available, and this allowed a benchmark for validation of a CFD model (see Section 5.1). The geometry of the flow path was modelled approximately on the Bosch poppet valve injector (Figure 2.8).

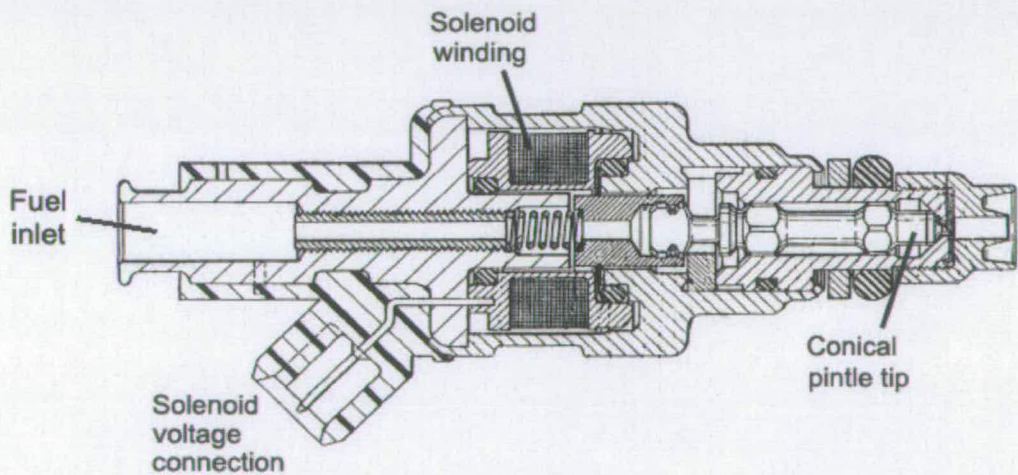


Figure 4.1: Bosch Solenoid-Actuated Conical Tip Injector [20]

Only the region of the conical pintle tip was modelled. The mesh coordinates used for the Bosch injector model are shown in Figure 4.2.

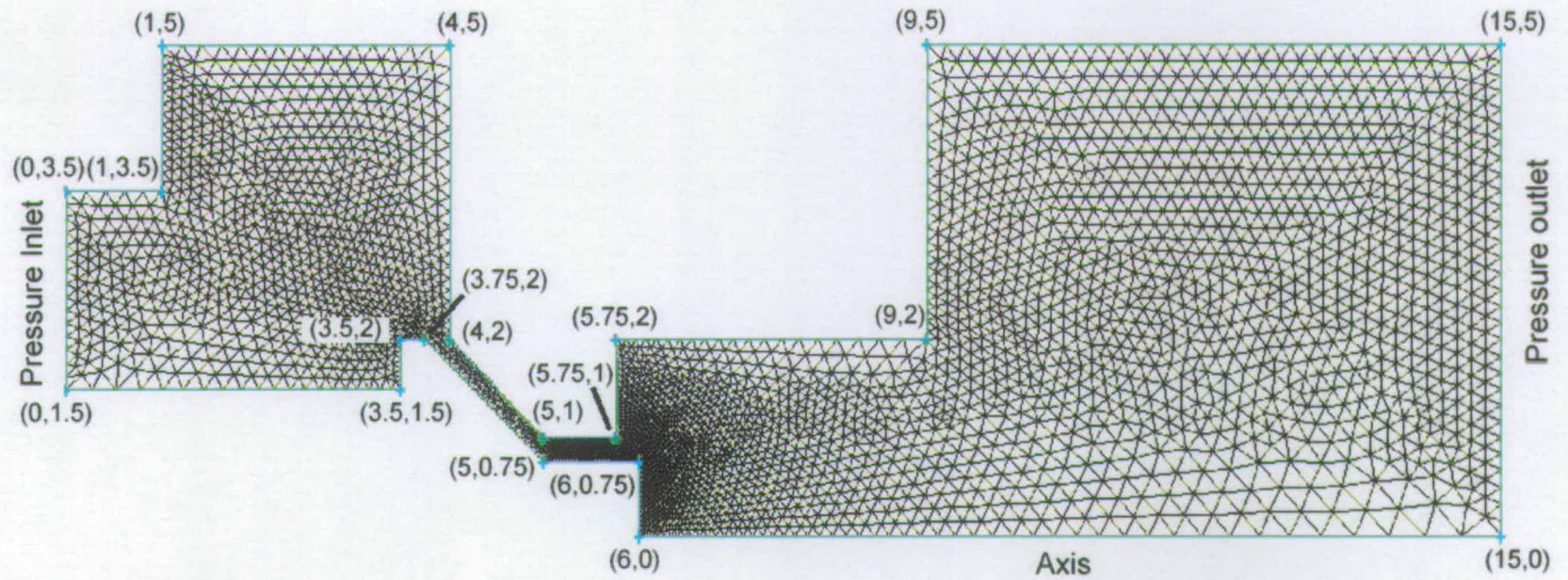


Figure 4.2: Model Geometry Coordinates

The minimum geometric flow area is modelled as a ring of outer radius 1 mm and inside radius 0.75 mm. This is shown in profile in Figure 4.2 at the tip of the pintle at coordinate (5,0.75). This would give a geometric minimum flow area of 1.37 mm².

The model mesh was developed as shown in Figure 4.2. The triangular cells have been biased so that the greatest mesh density occurs in the region of the minimum flow area. In this region, points of flow separation could exist, and the flow can be trans-sonic. High gradients of pressure could be expected, so a high mesh density is needed in this region. In all, this mesh has 6,232 cells, 9,543 faces and 3,312 nodes.

The mesh has also been biased to give a high cell density at the exit from the minimum flow area. Trans-sonic flow conditions in the minimum flow area can lead to shock wave formation at the exit, and associated high gradients of pressure could be expected here also.

Finally, the defined boundaries of Pressure Inlet, Axis (of rotational symmetry) and Pressure Outlet are shown in Figure 4.2. All remaining boundaries not labelled in Figure 4.2 were defined as type Wall. The Pressure Outlet boundary was placed relatively far (1 cm) from the nozzle exit. This is to mitigate any effects of defining constant pressure across the outlet boundary on the model results of the flow field at the nozzle.

4.1.2 Annular Plate Injector

Published hydrogen mass flow rate data through the annular plate injector described in Section 2.2.1 was used to further validate the effectiveness of CFD in modelling trans-sonic, compressible flows (see Section 5.2).

Cross section drawings of the annular plate injector shown in Figure 3.1 are given by Press [21], indicating that the outer diameter of the injector is

25 mm. The approximate dimensions of the flow path geometry have been obtained by scaling the drawings to the stated outer diameter. The dimensions are shown in mm in Figure 4.3, showing the injector in the open position, with the annular plate pulled up by the solenoid away from the valve seat.

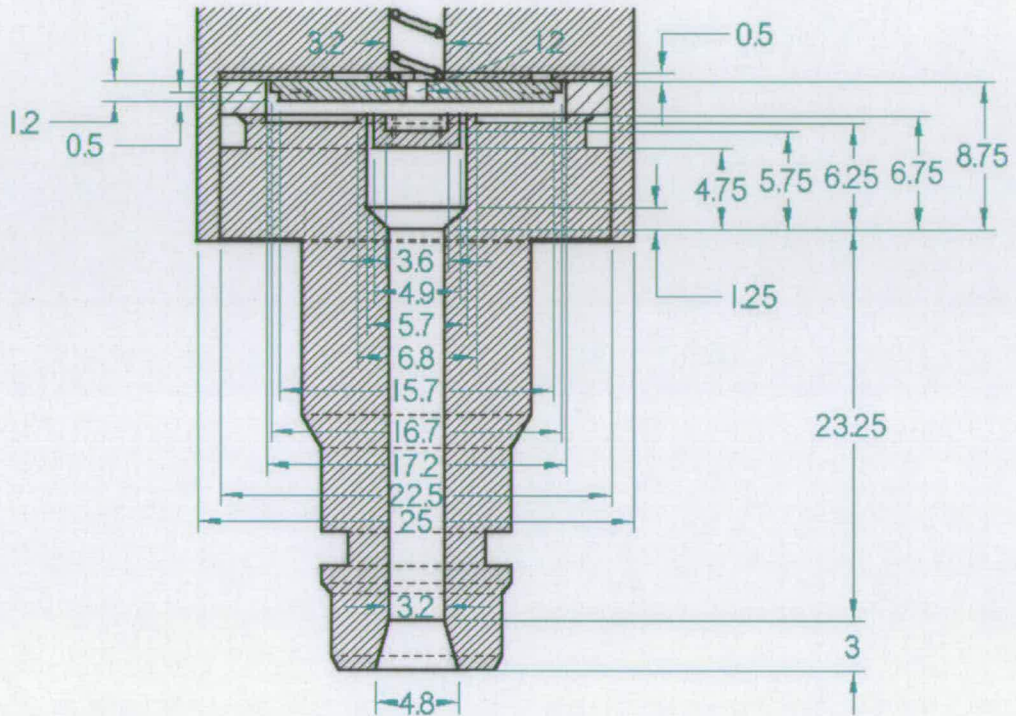


Figure 4.3: Annular Plate Injector Flow Path Geometry Dimensions (mm)

The Gambit mesh coordinates for this model were based on the dimensions shown in Figure 4.3. The minimum geometric flow area is located in the hole in the annular plate; area 4.5 mm^2 . The modelled geometry and triangular cell mesh is shown in Figure 4.4 (symmetry about the axis is not shown). As in Section 4.1.1 the cells have been biased to give a high mesh density in the region of the minimum flow area where high gradients of pressure may exist. This model mesh has 11,963 cells, 18,425 faces and 6,463 nodes.

The geometry of the return spring has been modelled as a series of concentric rings, rather than a helix in the inlet tube. Also, the three arc-shaped

orifices in the valve seat (as shown in Figure 3.2) have been modelled as one ring-shaped orifice.

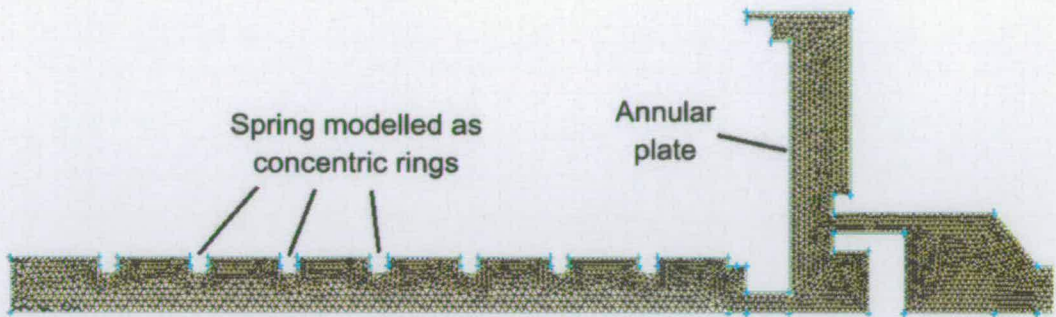


Figure 4.4: Model Triangular Mesh

The defined Pressure Inlet, Pressure Outlet and Axis boundaries are shown in Figure 4.5, and all boundaries not labelled in the figure were defined as type Wall. As in Section 4.1.1, the Pressure Outlet boundary has been placed relatively far (20 mm) from the exit from the minimum flow area.

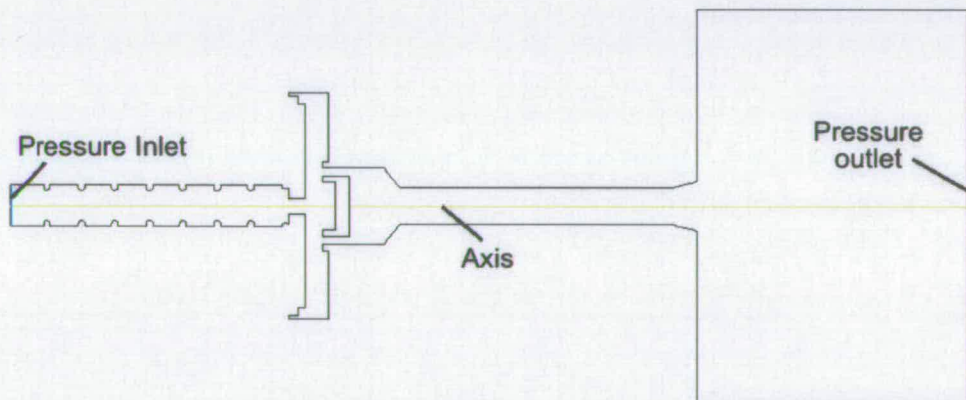


Figure 4.5: Model Flow Path Boundaries

4.1.3 Diaphragm Injector

Fully dimensioned drawings of the diaphragm injector design described in Section 3.1.1 are given in Appendix C. The gambit mesh geometry was

developed from these dimensions, and is shown in Figure 4.6. The three arc-shaped flow orifices in the valve seat (as shown in the drawings of Appendix C) have been modelled as a single ring-shaped orifice.

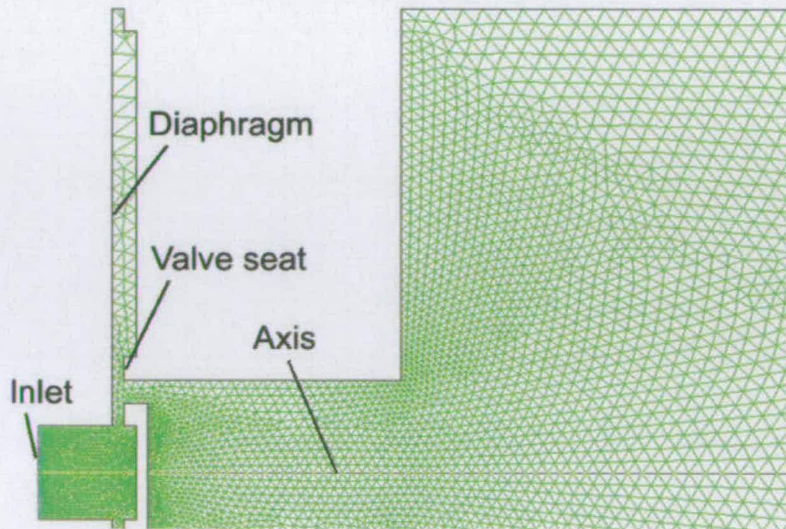


Figure 4.6: Diaphragm Injector Model Mesh

The mesh has been biased to give a high mesh density in the region of the diaphragm-valve seat interface, and in all the mesh has 8,760 cells, 13,390 faces and 4,631 nodes.

The defined Pressure Inlet and Axis of rotational symmetry boundaries are shown in Figure 4.6. The pressure outlet boundary (not shown in Figure 4.6) was placed far from the nozzle exit - 8.5 cm. All other boundaries not labelled in Figure 4.6 were defined as a type Wall.

The minimum flow area was determined by comparing the geometric areas of the inlet pipe, the region of radial flow between the diaphragm and valve seat, and the valve seat orifice. These flow areas are summarised in Table 4.1. The table shows that the region of radial flow between the diaphragm and the valve seat has the lowest geometric flow area, at 6.3 mm^2 .

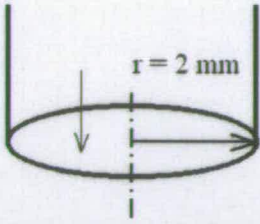
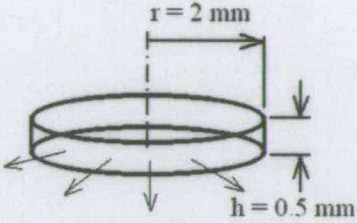
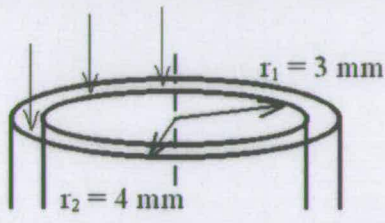
Region	Diagram	Equation	Flow Area
Inlet pipe		$A = \pi \cdot r^2$	12.6 mm ²
Diaphragm -valve seat interface		$A = 2\pi \cdot r \cdot h$	6.3 mm ²
Valve seat orifice		$A = \pi(r_2^2 - r_1^2)$	22.0 mm ²

Table 4.1: Determination of the Diaphragm Injector Minimum Flow Area

4.2 Model Parameters

The Gambit mesh cases described in Section 4.1 were imported into the two-dimension version of Fluent 5. The grid was then scaled to define the geometry units defined in Gambit in mm. A grid check was then performed, in particular checking for negative volume. Using the Mirror Planes option in the Views panel the grid view was set to show the symmetry about the axis boundary.

Each model was defined as single-species. The working fluid was defined as hydrogen, with properties imported from the Fluent fluids database. Table 4.2 summarises the properties used, and these were all defined as being constant.

Property	Value
Specific heat at constant pressure, c_p (J/kg.K)	14,283
Thermal conductivity, λ (W/m.K)	0.1672
Viscosity, μ (kg/m.s)	8.411e-6
Molecular weight, \tilde{m} (kg/kmol)	2.01594

Table 4.2: Material Properties of Hydrogen

In addition, in the Materials panel, since the model is developed for compressible flow, the fluid density was defined as obeying the ideal gas laws rather than the default constant definition. Under the Boundary Conditions panel, the fluid was also defined as hydrogen.

The operating condition was set to 101,325 Pa to represent atmospheric pressure. Initial boundary conditions were set as shown in Table 4.3.

Boundary	Condition	Value
Pressure inlet	Gauge Total Pressure	10 Pa
	Supersonic / Initial Gauge Pressure	5 Pa
	Total Temperature	300 K
	Direction Vector	
	- Axial	1
	- Radial	0
Pressure outlet	Velocity	
	- Intensity	10%
	- Viscosity ratio	10
	Gauge Pressure	0
	Backflow Temperature	300 K
	Turbulence	
- Intensity	10%	
- Viscosity ratio	10	

Table 4.3: Model Boundary Conditions

The RNG (Renormalisation Group) κ - ϵ viscous model was used, since it has been shown to offer superior results compared to the standard and realisable κ - ϵ models [58], with no viscous heating calculated.

The segregated solver (solving momentum, continuity and energy equations sequentially) was chosen for the simulations, since it was found that the coupled solver (solving equations simultaneously) resulted in regular floating point exception errors. Steady-state, axi-symmetric flow was also defined. Default under-relaxation factors and convergence criteria were used. A monitor of the mass flow rate across the inlet and outlet was set up to check for continuity convergence.

4.3 Obtaining a Converged Solution

As shown in Table 4.3, the initial inlet Gauge Total Pressure was set to 10 Pa. This is the gauge pressure with respect to the operating pressure defined in the Operating Conditions panel (101,325 Pa). The Supersonic/Initial Gauge Pressure is the static pressure and was set at 5 Pa to initialise the solution based on the pressure inlet boundary conditions.

Once the model was initialised, 10 iterations were performed before both Gauge Total Pressure and Supersonic/Initial Gauge Pressure were increased to 100 Pa. A further 30 iterations were then performed, checking for convergence using the plotted residuals. Both boundary conditions were then increased to 1,000 Pa, followed by 30 iterations, then to 10,000 Pa. Beyond this condition, the inlet pressure was increased in increments of 10-20 kPa, while performing 30-50 iterations between each increase. Starting the solution with a low pressure and increasing the boundary conditions incrementally in this way was found to provide a stable solution process avoiding errors.

With the inlet pressure boundary condition set to 2 bar, the solution was allowed to fully converge over around 300 iterations. While iterating, the mass continuity was checked using the mass flow rate monitor. A further check for convergence was then made by checking the mass flow rate

Flux Report. This report gives calculated absolute mass flux across specified boundaries (inlet and outlet), and calculates any difference, or net flux between boundaries. It is recommended [57] that the net calculated mass flux should be less than 0.01% of the absolute mass flux across the inlet or outlet for a converged solution.

The computation time per iteration was measured by timing 50 iterations and taking an average. The conical seat injector model took 2.52 seconds per iteration, the annular plate injector model 3.24 seconds and the diaphragm injector 2.78 seconds.

4.4 Discussion

The Gambit preprocessor has been used to develop geometry and mesh data for three CFD models. All three models were developed as axi-symmetric geometry, and used the triangular meshing scheme. This mesh scheme was found to give more stable mass continuity convergence than the quad scheme.

A convergent-divergent nozzle was modelled approximately based on a Bosch natural gas conical seat poppet-valve injector. The model has a minimum geometric flow area of 1.37 mm^2 .

A second model of the annular plate injector described in Section 2.2.1 was developed. The geometry of this injector was derived from published drawings. Key differences between the actual geometry and the model are that the return spring was modelled as a series of concentric rings, rather than a helix, and the three arc-shaped flow orifices were modelled as one ring-shaped orifice. This model has a minimum geometric flow area of 4.5 mm^2 .

Finally, a third model was developed from the dimensions of the injector design shown in Appendix C. Once again, the three arc-shaped flow orifices

have been modelled as a single ring-shaped orifice. The minimum geometric flow area for this model is 6.3 mm^2 .

All geometry models had a biased mesh, so that the greatest mesh density was placed in the region of the minimum flow area. This was carried out so that regions of flow separation and of high pressure gradient (e.g. across shock waves) could be modelled accurately. Also, all the models had the pressure outlet boundary placed relatively far from the minimum flow area. This was to minimise any effects of defining a constant pressure across the outlet boundary on the flow field in the minimum flow area.

The Gambit geometry and mesh data were imported into the Fluent CFD package, and each model was defined as single-species, with the properties of hydrogen assumed. Density was set as obeying the ideal gas law, rather than the default constant definition, since the model is of compressible flow. The segregated solver was used, since the coupled solver was found to give regular errors during the solution process.

To obtain a stable, converged solution, the initial inlet gauge pressure was set very low at 10 Pa. This boundary condition was then increased incrementally, performing a number of iterations between each increment to allow the solution to converge. In this way, it generally took between 5000 and 8000 iterations to reach a converged solution with 2 bar inlet pressure. For higher inlet pressure boundary conditions, several more thousand iterations were required.

The time per iteration was recorded for each model, and these are summarised in Table 4.4. The table also includes the number of cells, faces and nodes of the mesh of each model.

Table 4.4 clearly shows the computation time penalty as the number of cells in the mesh increases. Since 5000 to 8000 iterations were required to reach a solution with 2 bar inlet pressure, this implies that the total com-

Model	Seconds per Iteration	Cells	Faces	Nodes
Conical seat	2.52	6,232	9,543	3,312
Annular plate	3.24	11,963	18,425	6,463
Diaphragm	2.78	8,760	13,390	4,631

Table 4.4: Model Computation Times, Showing Numbers of Cells, Faces and Nodes

putation time for the diaphragm injector model would be between 3.9 and 5.6 hours. This excludes the time taken to adjust the parameters during the solution process.

Chapter 5

CFD MODEL ANALYSIS

To validate the application of CFD modelling to the particular design case of trans-sonic hydrogen flow, this chapter first compares modelled and empirical mass flow rate characteristics of two types of injector. Further validation is provided by comparing modelled flow characteristics of the diaphragm injector design with those predicted using equations describing compressible flow.

For each of these three cases, qualitative model results showing Mach number contours in the flow field are shown to check for predicted trans-sonic flow ($Ma > 1$). Corresponding velocity vector plots also show the position of the vena contracta, or minimum flow area. Quantitative results show the pressure flow field across the injector model geometry and the computed mass flow rate-inlet pressure relationship. Further modelled results show the effect of the back pressure on shock wave formation at the injector exit.

5.1 Compressible Flow Model Validation

5.1.1 Published Data

Pashley and Stone [22] have published mass flow rate data of CO₂, N₂ and He through a Bosch methanol injector similar to that shown in Figure 2.8. These data were used to give an initial validation of CFD modelling of trans-sonic compressible flows. The published data are shown in Figure 5.1.

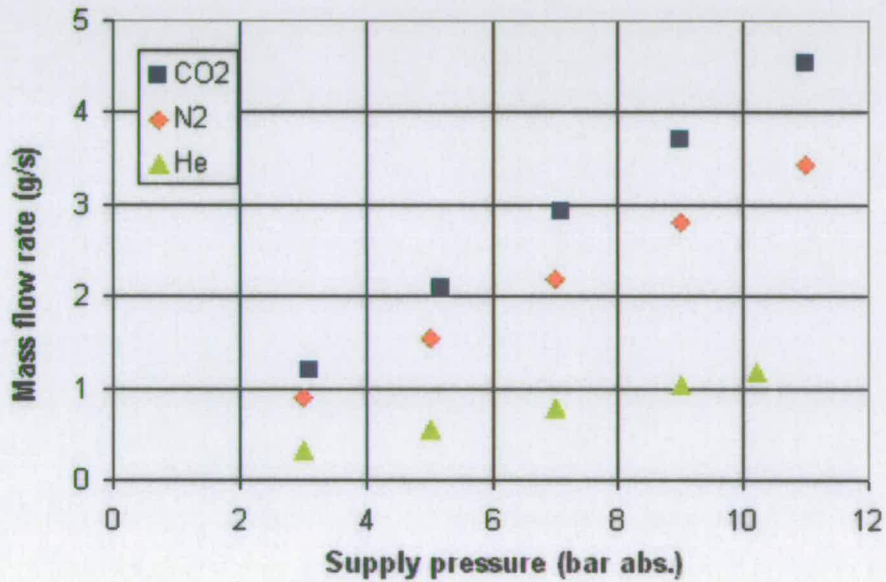


Figure 5.1: Published Mass Flow Rate Data of Gases Through a Bosch Methanol Injector [22]

Using the sonic flow compressible flow equation (see Section 5.3.1) these data were used to calculate the effective flow area, A_e - the 'throat' area, or minimum flow area in the flow path - of the injector.

$$A_e = \frac{\dot{m}}{p_0} \frac{\sqrt{T_0} \sqrt{R}}{\sqrt{\gamma}} \left(\frac{\gamma + 1}{2} \right)^{\frac{\gamma+1}{2(\gamma-1)}} \quad (5.1)$$

Corresponding calculated A_e results for the mass flow rate data in Figure 5.1 are shown in Figure 5.2. The figure shows that the calculated flow area

reduces at pressures below 6 bar - by up to 8% - but remains almost constant at higher pressure.

The results also show that the effective flow area reduces with lower molecular mass; helium (4 g/mol) demonstrates the lowest effective flow area compared with N₂ (28 g/mol) and CO₂ (44 g/mol) - up to 17% lower than CO₂. These researchers put this down to increased frictional losses with helium flow, associated with higher volumetric flowrates and velocities [22]. For helium at supply pressures above 6 bar, the effective flow area was calculated as 1.2 mm². For hydrogen (2 g/mol), the effective flow area may be somewhat lower than this.

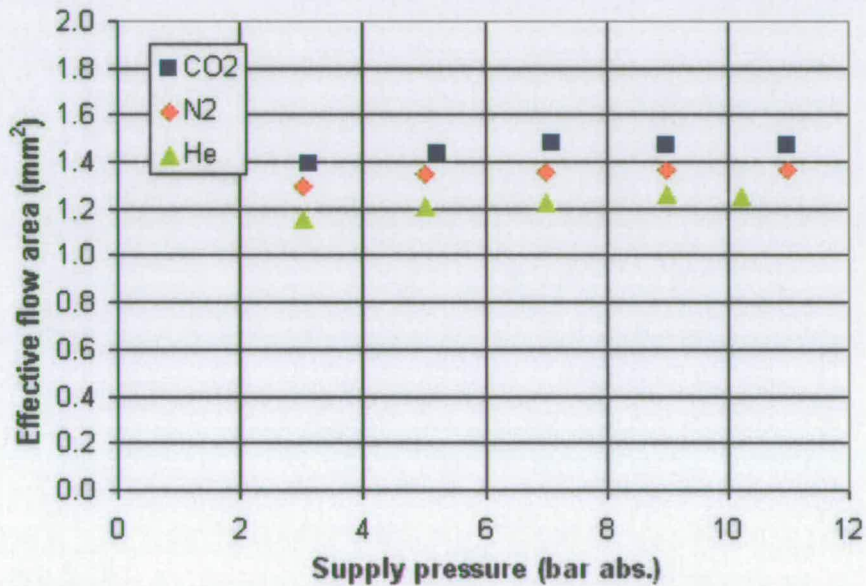


Figure 5.2: Calculated Effective Flow Area of the Bosch Methanol Injector

Assuming the flow area of the injector to be 1.2 mm² with hydrogen flow, equation 5.1 was used again to predict the mass flow rate of hydrogen gas through the injector at various supply pressures. The results of this analysis are shown in Figure 5.3.

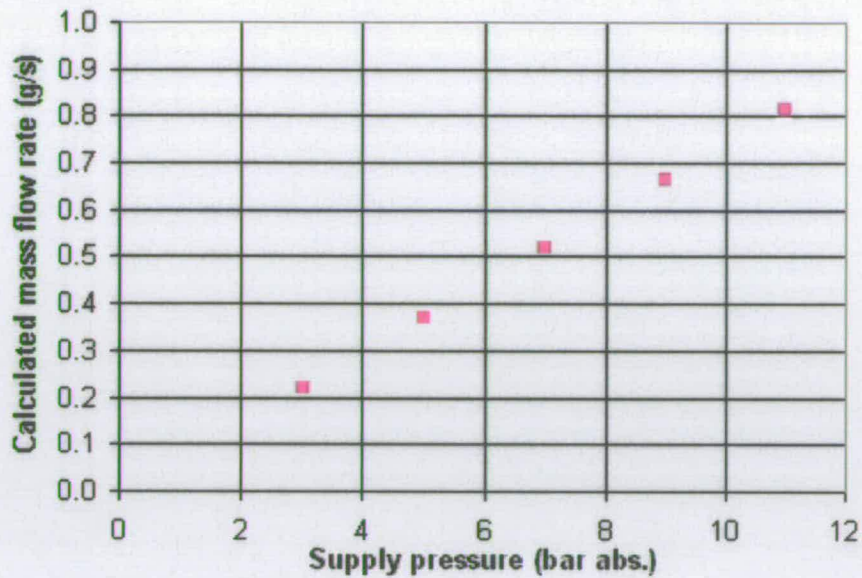


Figure 5.3: Predicted Mass Flow Rate of Hydrogen Through the Bosch Methanol Injector

5.1.2 Results Analysis

5.1.2.1 Qualitative Flow Field Results

The published data described in Section 5.1.1 were compared with results of a CFD model of the geometry described in Section 4.1.1. Figure 5.4 shows a Mach number (Ma) plot for a converged Fluent solution under 10 bar supply pressure, using the geometry and mesh shown in Figure 4.2. The plot has been clipped to the range $0 < Ma < 1$ - supersonic flow is outside the plot range, and is shown in black in Figure 5.4. The figure shows that the flow is trans-sonic across the minimum flow area - the flow is sub-sonic ($Ma < 1$) upstream, and super-sonic ($Ma > 1$) downstream.

Figures 5.5 and 5.6 show Mach number plots, zoomed to the area at the pintle tip; the region of the minimum flow area. Figure 5.5 shows Mach number ($0 < Ma < 1$) for 2 bar gauge inlet pressure, and Figure 5.6 for 10 bar

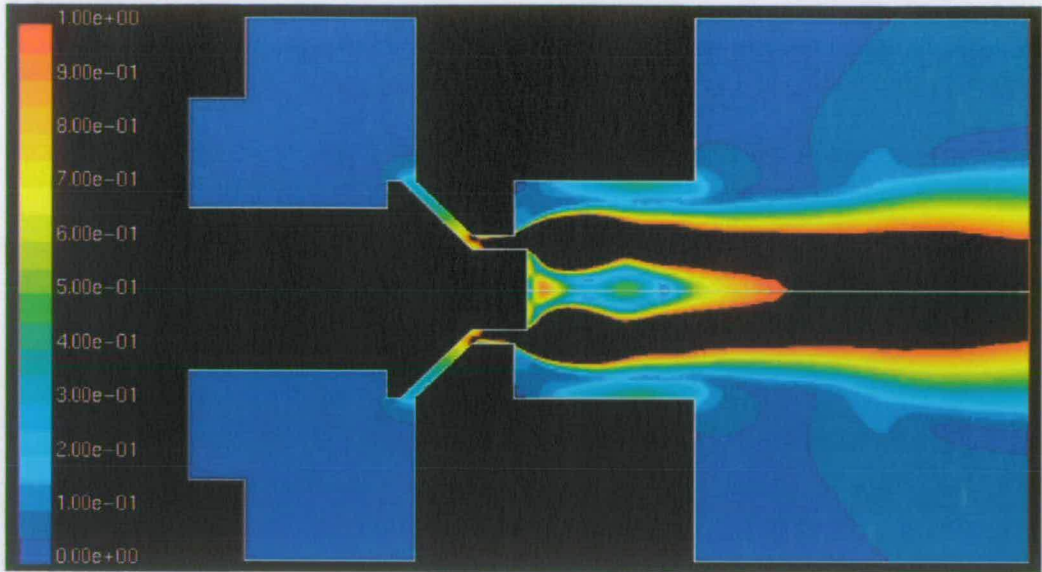


Figure 5.4: Mach Number Plot ($0 < Ma < 1$) at 10 bar g. Supply Pressure

gauge inlet pressure. Under 10 bar supply pressure, the region of supersonic flow spans the complete minimum flow area section.

Figure 5.7 shows a velocity vector plot of the flow field through the minimum flow area and at the exit jet at the pintle tip. This plot highlights the recirculation zones in the minimum flow area and where the flow expands at the exit.

The location of the vena contracta is clearly shown by the velocity vector plot in Figure 5.8, where it is marked by the low velocity recirculation zone near the pintle tip. Figure 5.8 shows the effective minimum flow area at the ‘throat’, and that this area is smaller than the geometric minimum flow area.

Finally, Figure 5.9 shows a plot of contours of absolute pressure. The plotted range has again been clipped, to $101,325 \text{ Pa} < p < 1,101,325 \text{ Pa}$. The plot shows the high gradient pressure drop across the throat, and further expansion to below atmospheric pressure (below the plotted scale - black region) at the pintle tip.

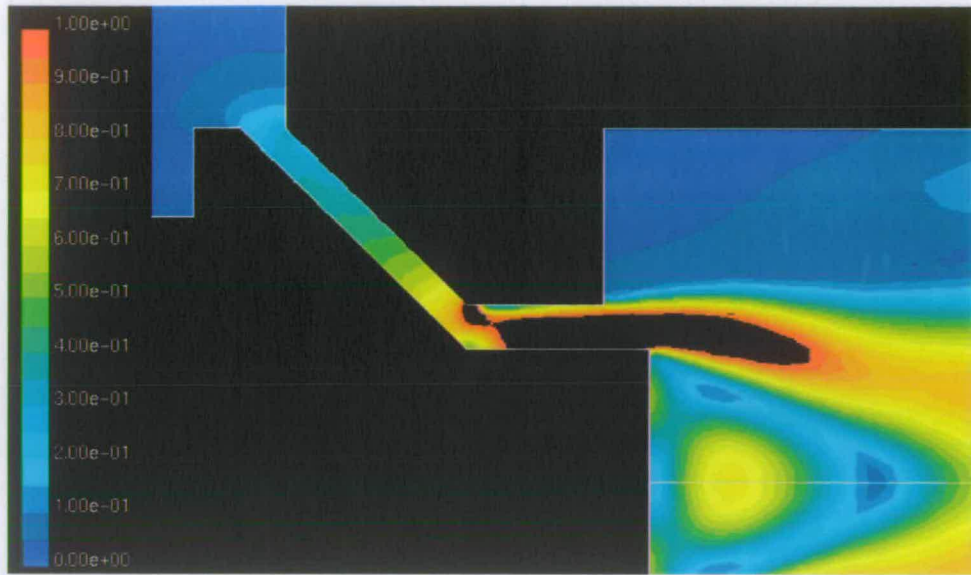


Figure 5.5: Mach Number Plot ($0 < Ma < 1$) at the Throat Section - 2 bar g. Supply Pressure

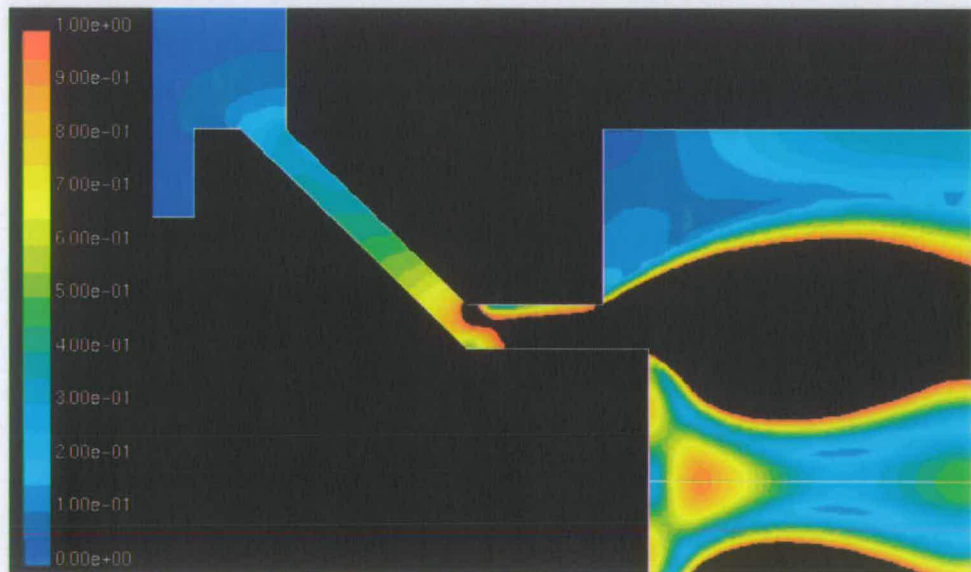


Figure 5.6: Mach Number Plot ($0 < Ma < 1$) at the Throat Section - 10 bar g. Supply Pressure

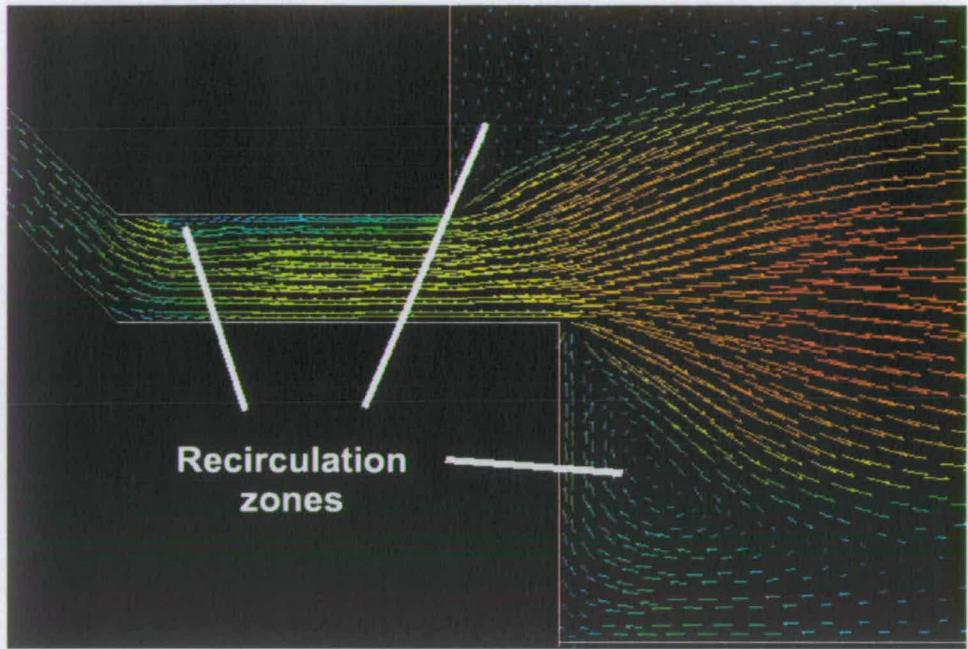


Figure 5.7: Velocity Vector Plot Showing Recirculation Zones - 10 bar Gauge Supply Pressure

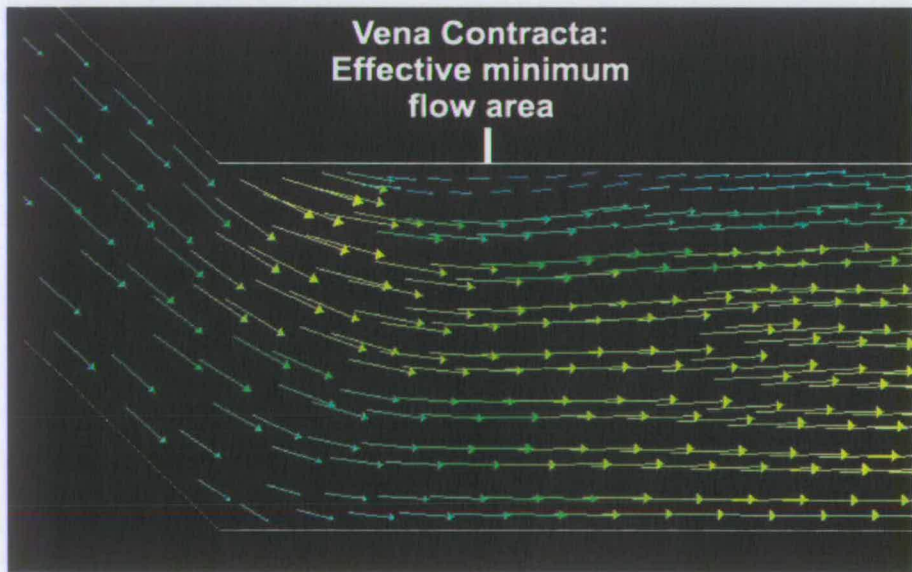


Figure 5.8: Close-Up of Velocity Vectors at the Throat Section - 10 bar Gauge Supply Pressure

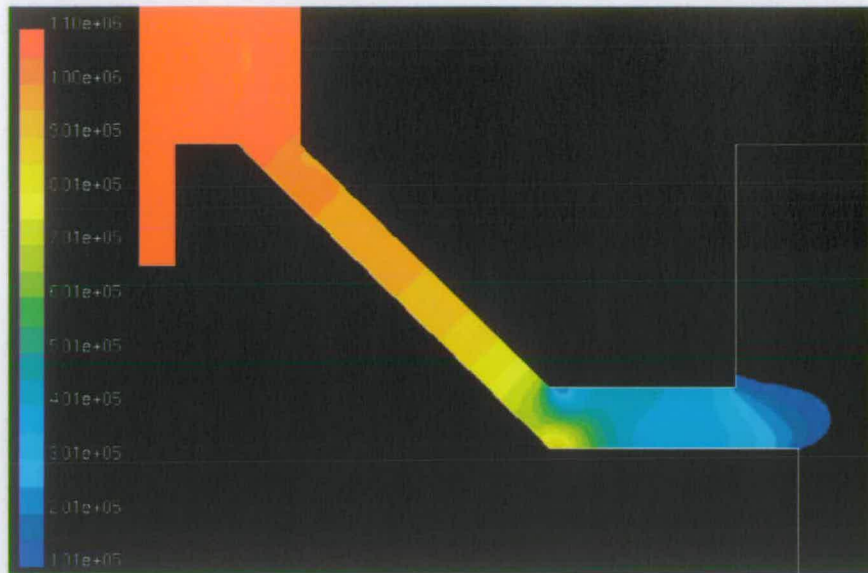


Figure 5.9: Absolute Pressure Contours ($101,325 \text{ Pa} < p < 1,101,325 \text{ Pa}$) at the Throat - 10 bar Gauge Supply Pressure

5.1.2.2 Quantitative Model Results

Figure 5.10 shows results of the Fluent Mass Flux report at various Pressure Inlet boundary conditions. It was shown in Section 5.1.2.1 that the flow is trans-sonic throughout the range of 2 bar to 10 bar gauge inlet pressure. Figure 5.10 shows that as expected under these conditions, the modelled mass flow rate increases linearly with supply pressure; a linear best-line-fit has been superimposed on the model data. Also included in Figure 5.10 is the hydrogen mass flow rate derived from published data in Section 5.1.1. The figure shows that the model is validated by the real data, since a linear relationship is correctly calculated. The results also show that the model predicts on average 13.2% lower mass flow rate than the derived real data.

The geometric minimum flow area of the model was shown in Section 4.1.1 to be 1.37 mm^2 . Using the model mass flow rate results shown in Figure 5.10, the effective flow area was calculated using equation 5.1. The results

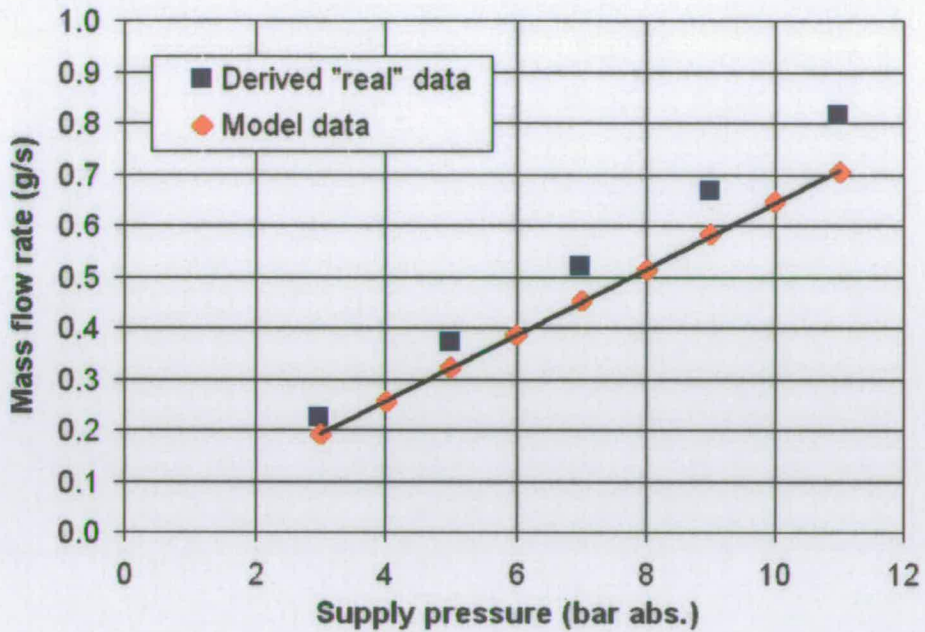


Figure 5.10: Calculated Model Mass Flow Rate vs Inlet Pressure with Results Derived From Real Data

are shown in Figure 5.11. The figure also shows the effective flow area derived from published data, of the Bosch injector as given in Figure 5.2.

Figure 5.11 shows that the calculated model effective flow area changes little with pressure inlet boundary condition compared with the published data; up to 1.6% drop at lower pressures compared to the maximum 8% drop shown by the published data. The model effective flow area is approximately 1.04 mm^2 , and this is 13.3% lower than the effective flow area of the Bosch injector (as would be expected, since the mass flow rate data is 13% lower than the published data). Equation 5.2 relates the discharge coefficient, C_d , to the effective flow area, A_e , and the geometric flow area, A_g (1.37 mm^2). This implies that the discharge coefficient predicted by the model is 76%.

$$A_e = C_d A_g \quad (5.2)$$

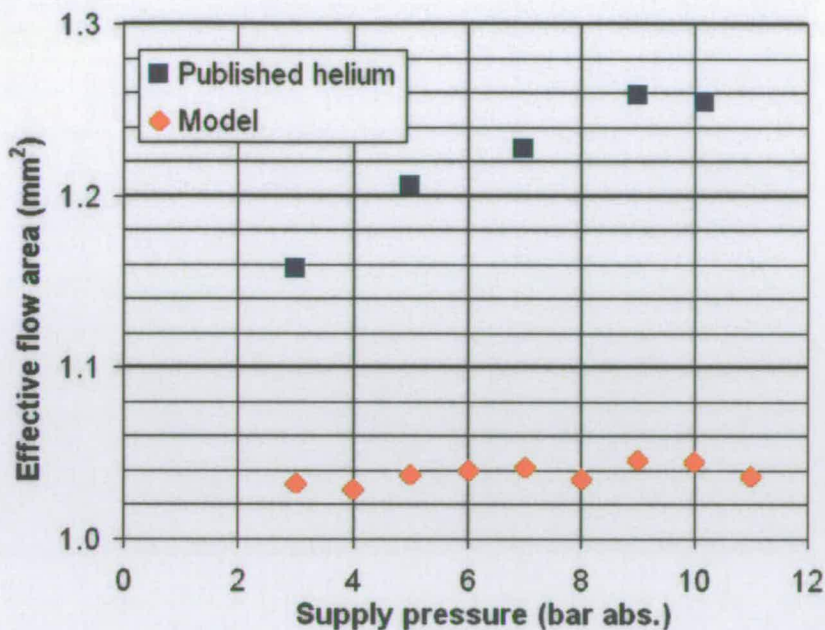


Figure 5.11: Calculated Model Effective Flow Area (1.0-1.3 mm²) vs Inlet Pressure with Results Derived From Real Data

The discrepancy in the mass flow rate data shown in Figure 5.10 is due to differences between the actual geometry of the Bosch injector and the approximated geometry used in the model. These results could suggest that the geometric minimum flow area of the model is smaller than that of the Bosch injector.

5.2 Annular Plate Injector Model and Validation

5.2.1 Published Data

Kabat and Heffel [20] have published fuel delivery data of hydrogen through the annular plate injector described in Section 2.2.1. Figure 5.12 shows the published data of gas delivery, m_{H_2} , vs injection pulse width, PW, (injection duration) for supply pressures of 5.15 bar abs. and 6.18 bar abs.

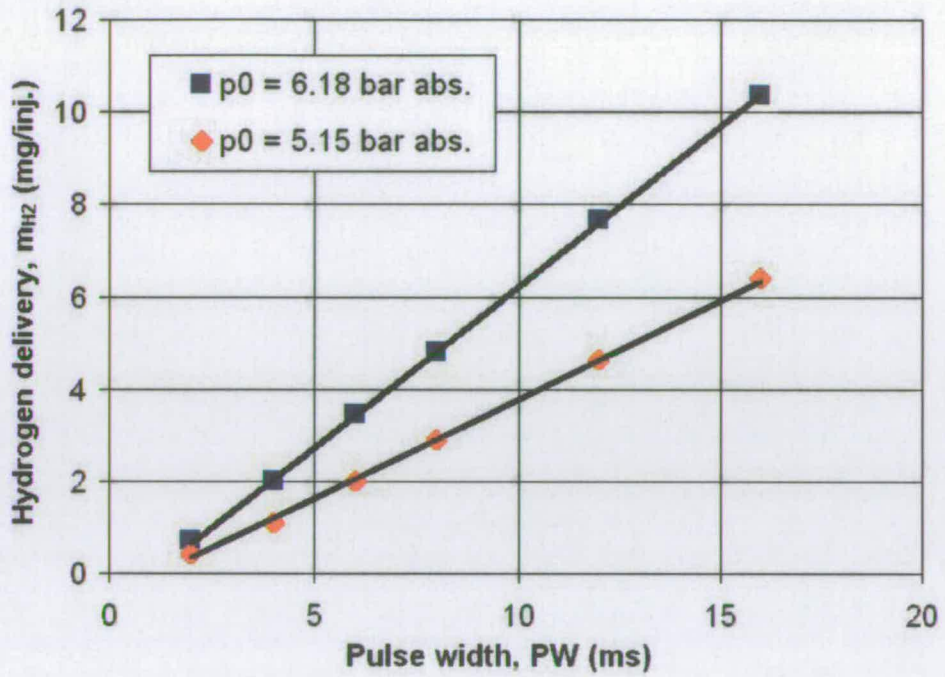


Figure 5.12: Published Fuel Delivery Data vs Injector Pulse Width of an Annular Plate Injector [20]

The data of Figure 5.12 lie on linear best line fits described by equations 5.3 and 5.4.

$$m_{H_2, p_0=6.18} = 0.69PW - 0.74 \quad (5.3)$$

$$m_{H_2, p_0=5.15} = 0.43PW - 0.49 \quad (5.4)$$

Figure 5.13 shows the relationship between the average flow rate during injection (quotient of hydrogen delivery / pulse width) vs pulse width. The figure shows that the dynamic mass flow rate reduces significantly when the injection pulse width is short. This is probably because the injector does not open instantaneously, and the flow is restricted during the injector-opening and injector-closing periods. As a proportion of the total injector pulse width,

these open and close periods become more significant as the pulse width is reduced, lowering the average flow rate.

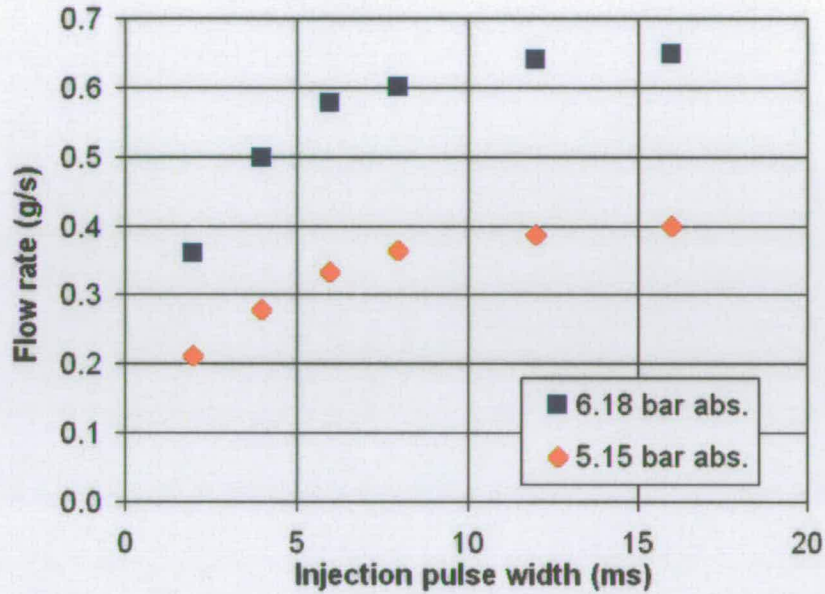


Figure 5.13: Dynamic Hydrogen Flow Rate vs Pulse Width

The static mass flow rate can be obtained by manipulating the linear best line fit equations shown in Figure 5.12 to express the mass flow rate as a function of pulse width. The flow rate as the pulse width tends to infinity then indicates the static mass flow rate. For the supply pressure cases of 5.15 and 6.18 bar abs., the static mass flow rates are 0.43 and 0.69 g/s respectively. To allow graphical comparison with flow rate data in Section 5.2.2.2 the two data points are plotted in Figure 5.14.

Using equation 5.1, these mass flow rate data were used to calculate the effective flow area, A_e , of the injector. The flow rate and effective flow area data are summarised in Table 5.1.

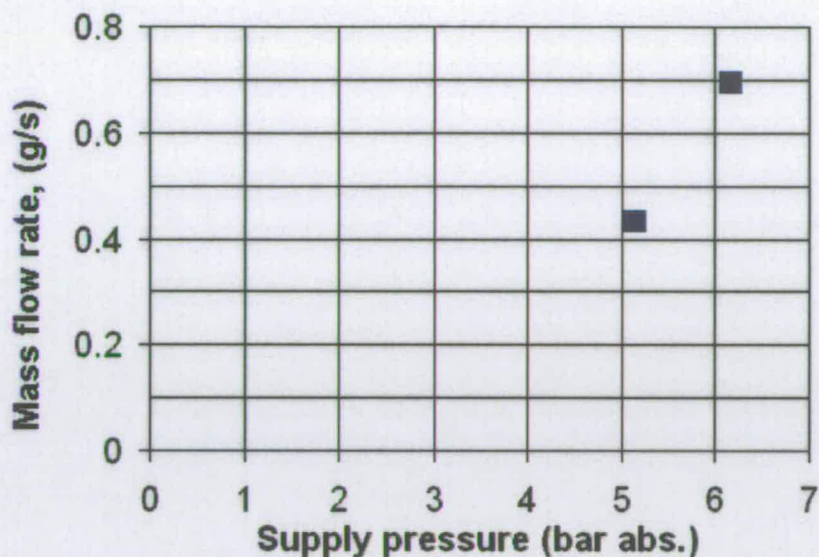


Figure 5.14: Static Hydrogen Flow Rate vs Supply pressure

Supply pressure (bar abs.)	Mass flow rate (g/s)	Effective flow area mm ²
5.15	0.43	1.4
6.18	0.69	1.8

Table 5.1: Mass Flow Rate and Effective Flow Area Data for Annular Plate Injector

5.2.2 Results Analysis

5.2.2.1 Qualitative Flow Field Results

A Mach number plot for a converged solution of the model geometry described in Section 4.1.2, with the inlet pressure boundary condition set to 618,325 Pa abs., is shown in Figure 5.15. The contour range has been clipped to show subsonic flow only ($0 < Ma < 1$). The figure shows the trans-sonic region (outside the plotted range, shown in black) at the minimum flow area in the hole in the annular plate.

A plot of velocity vectors in the flow field is shown in Figure 5.16. The plot shows where recirculation zones are located at the exit from the minimum flow area, through the valve seat, and into the injector outlet tube.

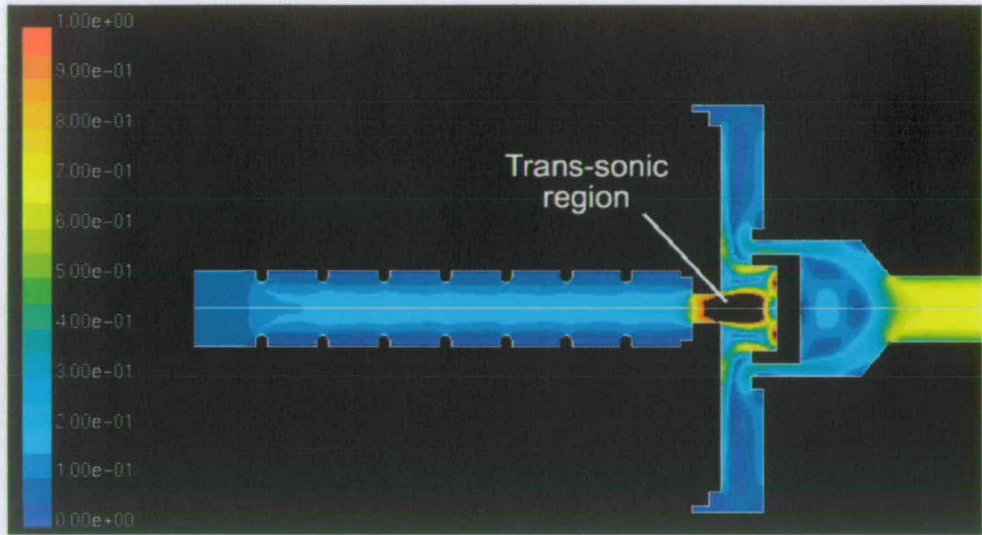


Figure 5.15: Mach Number Plot ($0 < Ma < 1$) - 6.18 bar abs. Supply Pressure

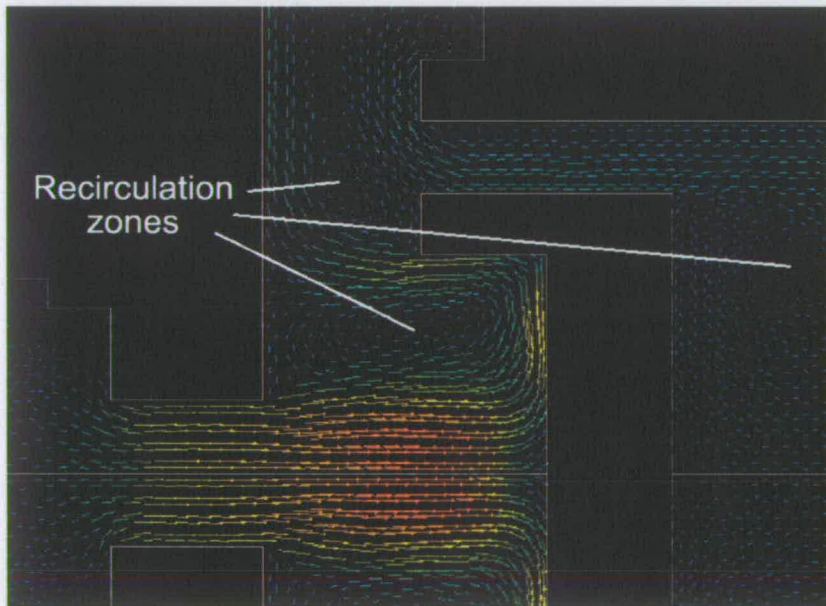


Figure 5.16: Velocity Vector Plot Showing Recirculation Zones - 6.18 bar abs. Supply Pressure

The approximate location of the vena contracta in the geometric minimum flow area is shown in Figure 5.17.

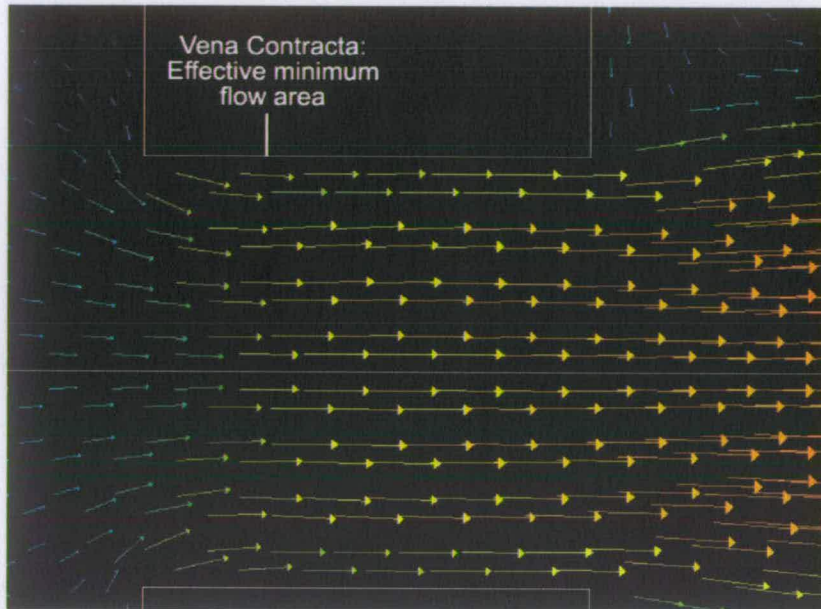


Figure 5.17: Velocity Vector Plot Showing Location of the Vena Contracta - 6.18 bar abs. Supply Pressure

Figure 5.18 shows contours of absolute pressure in the region of the inlet tube. The plotted range has been clipped to $598,325 \text{ Pa} < p_{abs} < 618,325 \text{ Pa}$ to highlight the drop in pressure across this region. As the figure shows, a 0.2 bar pressure drop is modelled as the flow passes through the inlet tube. This pressure drop is caused by the return spring geometry, which has been modelled as a series of concentric rings. Flow through an inlet pipe with a helical spring may display a lower pressure drop than is shown in Figure 5.18.

Contours of absolute pressure clipped to the range of atmospheric pressure, 101,325 Pa, to 601,325 Pa are shown in Figure 5.19. The figure highlights the high gradient of pressure in the minimum flow area, and expansion to below atmospheric pressure at the exit from the valve seat.

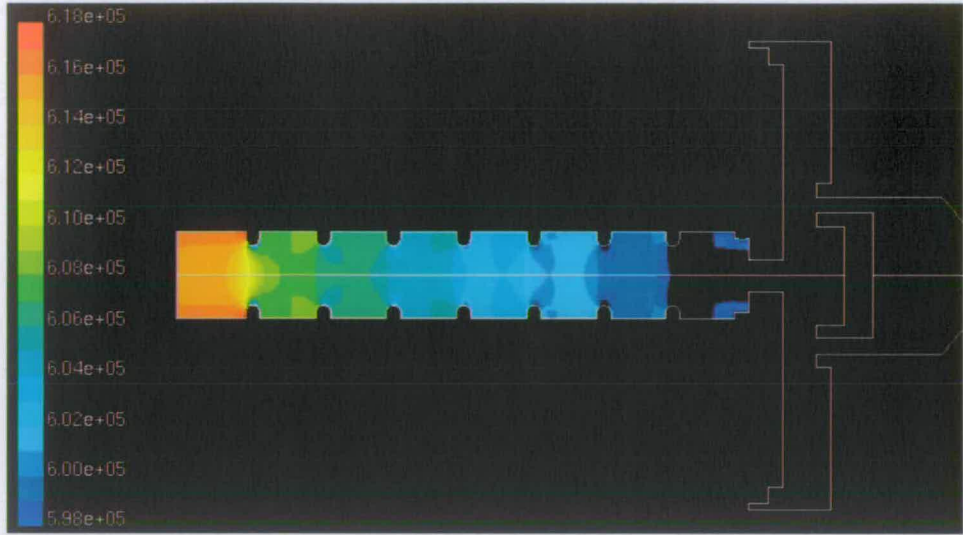


Figure 5.18: Absolute Pressure Contours ($598,325 \text{ Pa} < p_{abs} < 618,325 \text{ Pa}$) in the inlet tube - 6.18 bar abs. Supply Pressure

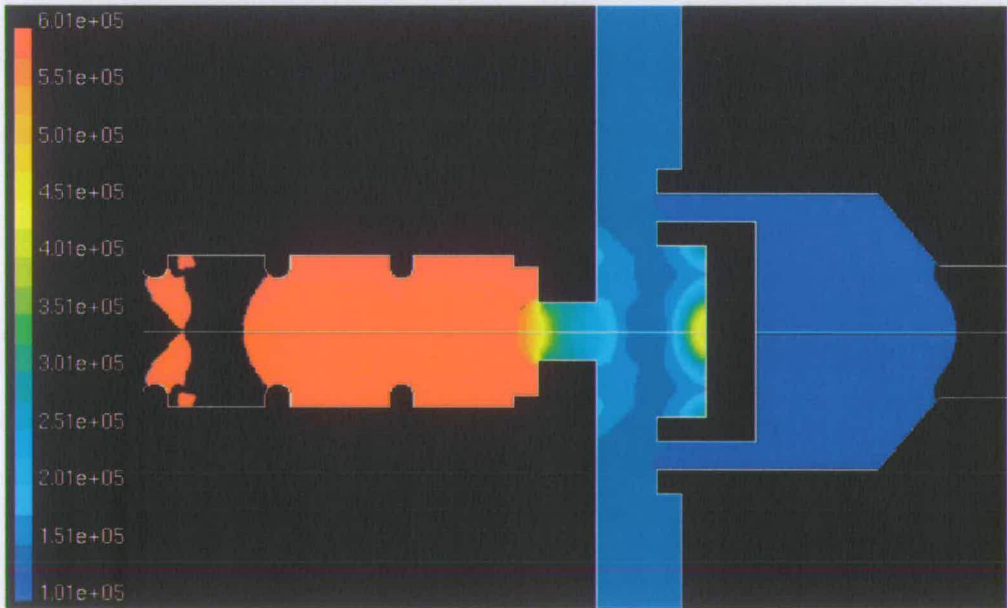


Figure 5.19: Absolute Pressure Contours ($101,325 \text{ Pa} < p_{abs} < 601,325 \text{ Pa}$) in the inlet tube - 6.18 bar abs. Supply Pressure

5.2.2.2 Quantitative Model Results

Figure 5.20 shows model results of reported Mass Flux at inlet pressures between 3 bar and 7 bar. As expected for trans-sonic flow, the model predicts a linear relationship between mass flow rate and supply pressure. The published mass flow rate data derived in Section 5.2.1 is included in Figure 5.20. The figure shows that the model predicts up to 50% lower mass flow rate than the published data.

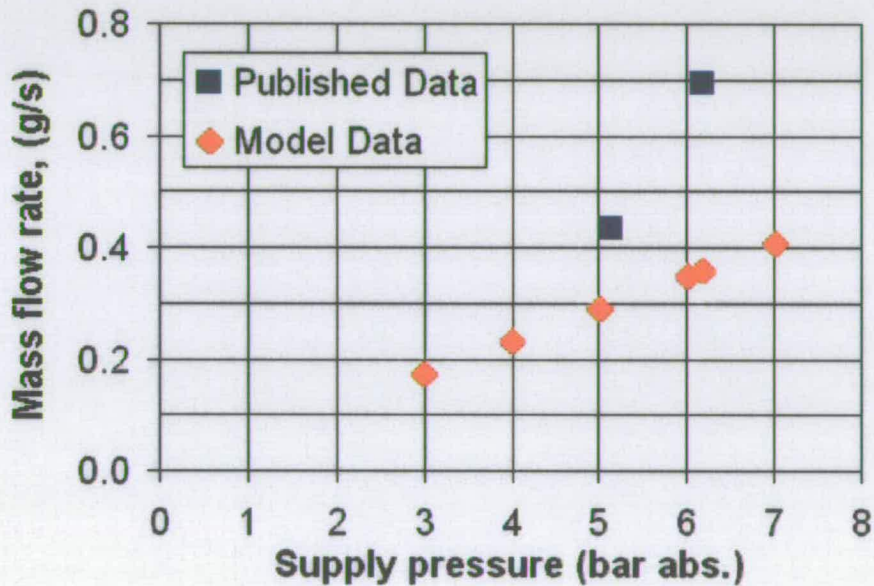


Figure 5.20: Model Mass Flow Rate Results vs Inlet Pressure with Published Data

Effective flow area, calculated using equation 5.1 and the mass flow rate and pressure data in Figure 5.20, is shown in Figure 5.21. The data shows that the model predicts a maximum 1.6% drop in effective flow area with lower supply pressure compared to the 25% drop indicated by the published data.

As described in Section 4.1.2, the geometric minimum flow area of the modelled injector is 4.52 mm^2 . The data in Figure 5.21 indicate a modelled

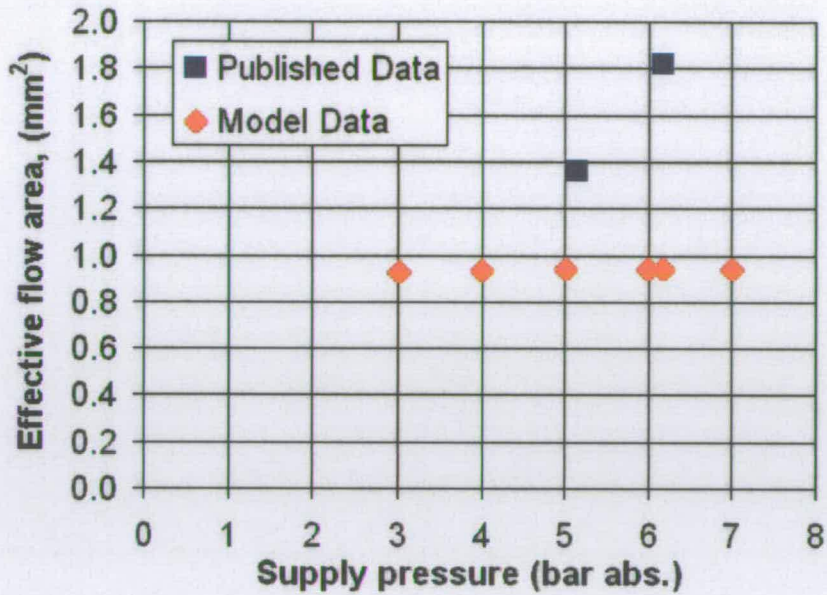


Figure 5.21: Calculated Effective Flow Area

effective flow area of approximately 1 mm^2 . Using equation 5.2, this implies that the discharge coefficient of the modelled injector would be 22%.

The discrepancy between the published and modelled mass flow rate data and the low modelled discharge coefficient could be due to higher pressure losses in the inlet pipe (see Section 5.2.2.1) since the return spring geometry is modelled as a series of concentric rings rather than a helix. Also, the model geometry has very square edges where flow separation can readily occur leading to high pressure losses in the flow field. In reality, the edges would be more rounded and this could account for some discrepancy between the published and modelled mass flow rate data. Error in estimating the dimensions of the injector components (see Section 4.1.2) could also contribute to the discrepancy.

5.3 New Injector Design and Validation

Against Theory

5.3.1 Compressible Flow Theory

Radial flow such as flow through a poppet valve can be described by the equations derived for compressible flow through a nozzle [7]. Mass flow rate, \dot{m} , is related to the upstream stagnation pressure, p_0 , and stagnation temperature, T_0 , static pressure just downstream of the flow restriction (assumed equal to the pressure at the restriction, or throat, p_T), and a reference area, A_R , characteristic of the valve design. The relationship is given by equation 5.5 - the full derivation is given by Douglas *et al.* [24].

$$\dot{m} = \frac{C_d A_R p_0}{\sqrt{RT_0}} \left(\frac{p_T}{p_0} \right)^{1/\gamma} \sqrt{\left\{ \frac{2\gamma}{\gamma-1} \left[1 - \left(\frac{p_T}{p_0} \right)^{\frac{\gamma-1}{\gamma}} \right] \right\}} \quad (5.5)$$

Consider a case where p_0 and p_T are initially at equal pressure. p_T is then decreased; the flow rate is initially zero and then increases as the downstream pressure drops. A plot of \dot{m} against p_T/p_0 as p_T is decreased exhibits a maximum mass flow rate at some pressure ratio, according to equation 5.5. Figure 5.22 shows such a plot of equation 5.5, with \dot{m} as a function of p_T/p_0 , where p_0 and p_T are initially equal to 6.18 bar abs., and then p_T is decreased. The p_T/p_0 axis is inverted, with values from 1.0 to 0.0 shown. Gas properties, $\gamma = 1.41$ and $R = 4121 \text{ J/kg.K}$ were used in the calculation, with $T_0 = 300 \text{ K}$ and an arbitrary flow area, $C_d A_R = 2 \text{ mm}^2$.

According to equation 5.5, the maximum mass flow rate occurs for the value of $p_T/p_0 = r$ which makes:

$$\frac{d}{dr} \left[r^{2/\gamma} \left(1 - r^{(\gamma-1)/\gamma} \right) \right] = 0 \quad (5.6)$$

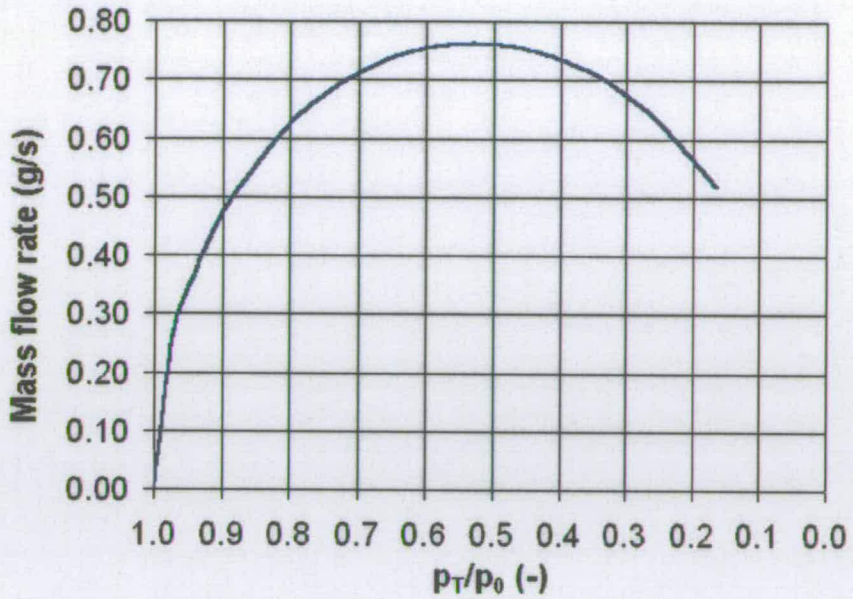


Figure 5.22: Calculated Effective Flow Area

Manipulation of equation 5.6 shows that at this condition

$$r = \frac{p_T}{p_0} = \left[\frac{2}{\gamma + 1} \right]^{\gamma/(\gamma-1)} \quad (5.7)$$

Further derivation shows that at this condition, the velocity of the gas, v , at the throat section equals the local velocity of sound, c [24]:

$$v = \sqrt{\frac{\gamma p_T}{\rho_T}} = c \quad (5.8)$$

Thus equation 5.7 describes the critical pressure ratio for sonic flow at the throat. For hydrogen ($\gamma=1.41$), the critical pressure ratio is equal to 0.527. If the downstream, or throat pressure, p_T , is at atmospheric pressure (1.01 bar), this implies a minimum supply pressure, p_0 of 1.92 bar to ensure trans-sonic flow.

Douglas *et al.* [24], describe a case known as the Laval nozzle, where the flow is subsonic in the converging section, at critical or transonic conditions

at the throat, and supersonic in the diverging section. The derivation shows that the mass flow rate for this case is described by equation 5.9:

$$\dot{m} = \frac{C_d A_R p_0}{\sqrt{RT_0}} \sqrt{\gamma} \left(\frac{2}{\gamma + 1} \right)^{\frac{\gamma+1}{2(\gamma-1)}} \quad (5.9)$$

Equation 5.9 shows that under these conditions the mass flow rate is independent of the downstream pressure. A change in mass flow rate could only be propagated upstream at the velocity of sound and therefore could not pass through the throat where the fluid velocity is sonic; the flow is 'choked' [24].

Thus equation 5.5 and Figure 5.22 describe the mass flow rate under subsonic conditions only. Once the critical pressure ratio is reached, the mass flow rate is described by equation 5.9 and remains constant and at a maximum for any further drop in downstream pressure, if the inlet pressure remains constant.

The pressure of the gas jet exiting the minimum flow area, is not necessarily equal to the back pressure of the gas into which the jet is discharging. If the back pressure, p_b , is lower than the jet exit pressure, p_e , the nozzle is 'under-expanded', and expansion waves form at the exit (Figure 5.23(a)). If the back pressure is higher than the jet pressure, the nozzle is 'over-expanded'. If the pressure difference is small, oblique shock waves form at the exit (Figure 5.23(b)). For larger pressure differences, normal shock waves form in the nozzle (Figure 5.23(c)).

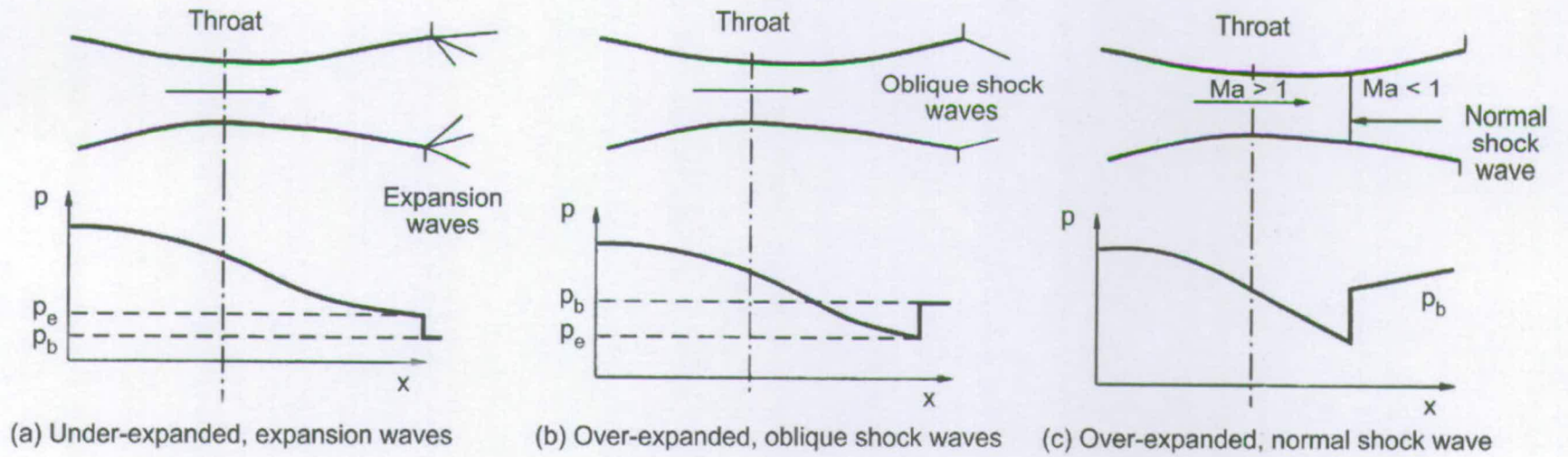


Figure 5.23: Shock wave Formation at a Nozzle Exit [24]

5.3.2 Results Analysis

5.3.2.1 Qualitative Flow Field Results

Figure 5.24 shows a plot of Mach number for a converged solution with 618,325 Pa abs. inlet pressure boundary condition. The plotted data range has been clipped to $0 < Ma < 1$, to plot subsonic flow only; areas of supersonic flow are shown as black regions off the high end of the plotted scale. The figure shows that at this inlet pressure, a region of supersonic flow occurs in a ring between the diaphragm and valve seat. The flow becomes subsonic again before entering a second supersonic region in the gaps in the valve seat. This region extends far into the expansion zone, around its edge.

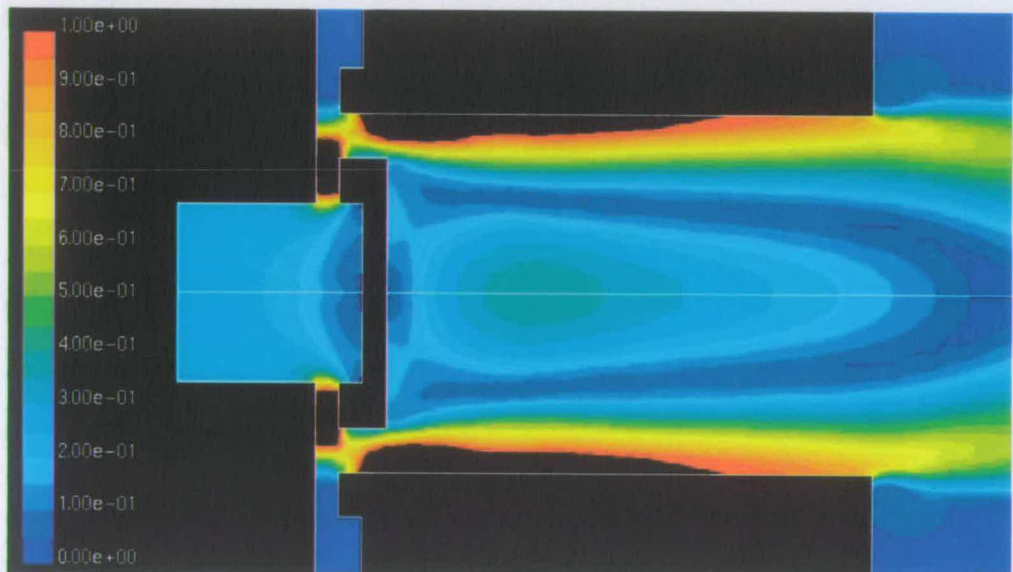


Figure 5.24: Mach Number Plot ($0 < Ma < 1$) - 6.18 bar abs. Inlet Pressure

A velocity vector plot in the minimum flow area region is shown in Figure 5.25. The figure shows the location of recirculation zones in the inlet, between the diaphragm and valve seat, in the valve seat gaps and in the expansion zone.

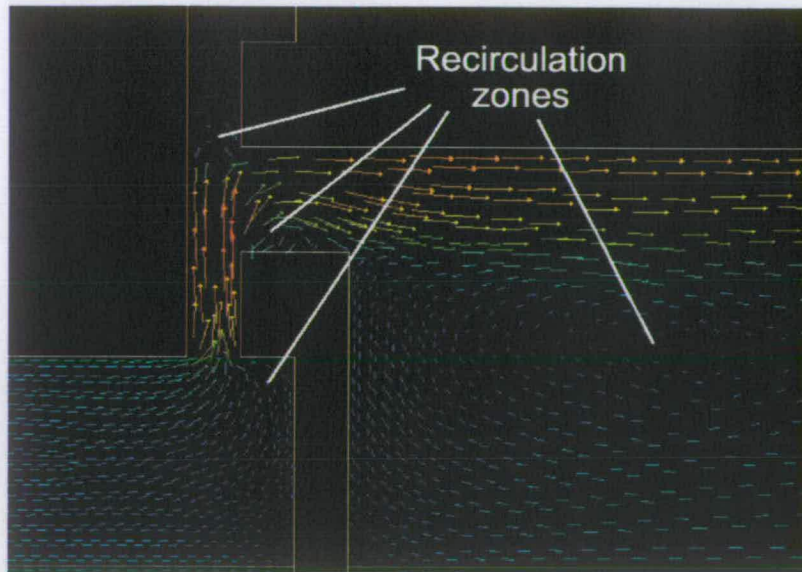


Figure 5.25: Velocity Vector Plot Showing Recirculation Zones - 6.18 bar abs. Inlet Pressure

Figure 5.26 shows a close-up of velocity vectors in the region of minimum flow area. The figure shows two venae contractae, corresponding to the two supersonic regions shown in Figure 5.24.

Finally, Figure 5.27 shows contours of absolute pressure clipped to the range of atmospheric pressure, 101,325 Pa, to 501,325 Pa. The high gradient of pressure in the minimum flow area is shown, followed by expansion to below atmospheric pressure in the expansion zone and finally reaching atmospheric pressure at the exit.

To compare theoretical and computed shock wave formation, a case with inlet pressure boundary condition set to 67 bar abs. was used. At this inlet pressure, the computed mass flow rate was 23 g/s corresponding to the maximum design mass flow rate for DI (see Appendix A).

Figure 5.28 shows a Mach number plot, clipped to show supersonic flow contours only in the range $1 < Ma < 3$. The outlet pressure boundary condition was at 2.2 bar abs. The figure shows that the supersonic region spans the complete width of the expansion zone at the nozzle exit.

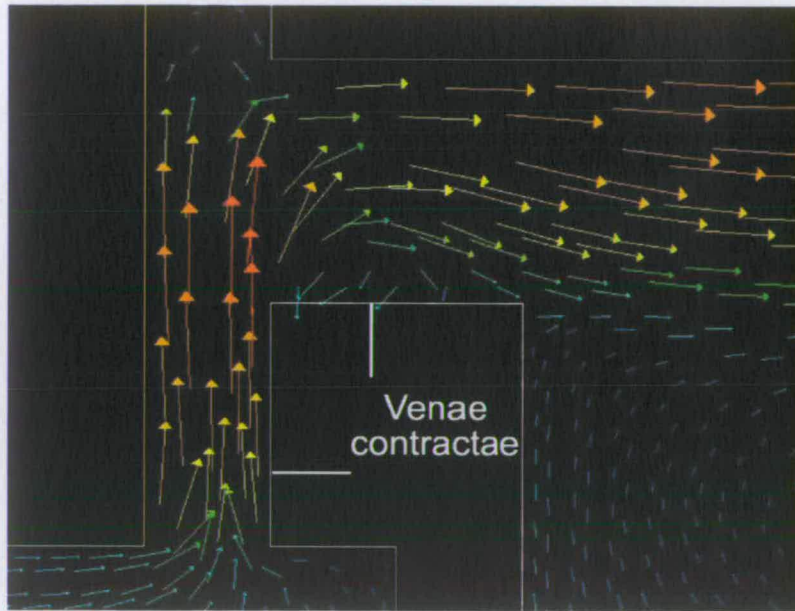


Figure 5.26: Velocity Vector Plot Showing Location of the Venae Contractae - 6.18 bar abs. Inlet Pressure

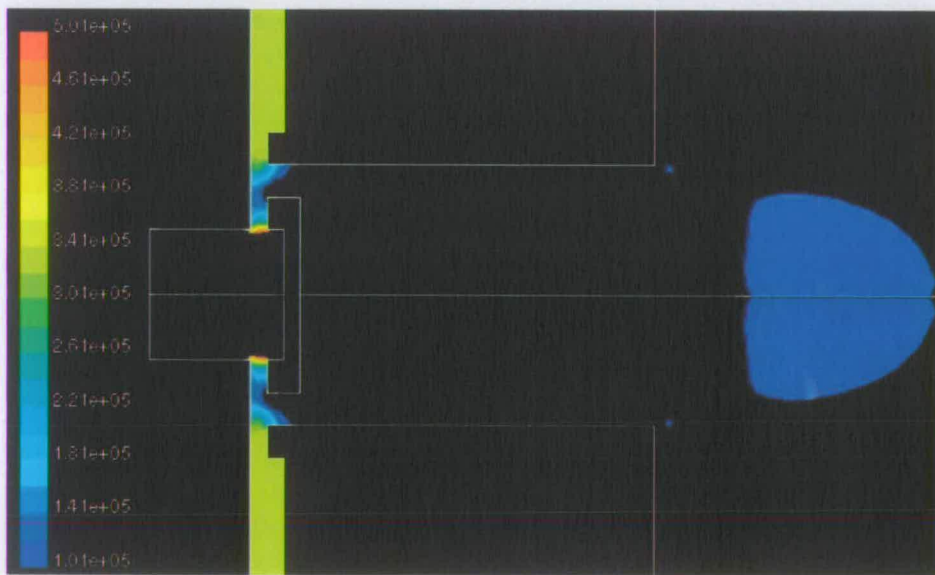


Figure 5.27: Absolute Pressure Contours ($101,325 \text{ Pa} < p_{abs} < 501,325 \text{ Pa}$) in the minimum flow area region - 6.18 bar abs. Inlet Pressure

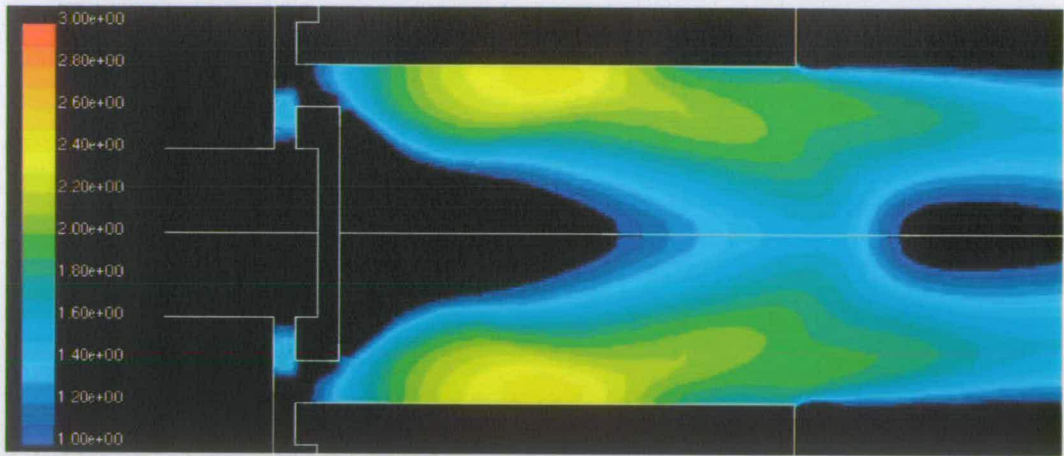


Figure 5.28: Mach Number Plot ($1 < Ma < 3$) for Outlet Pressure Boundary Condition 2.2 bar abs.

Contours of computed absolute pressure in the range $0 < p_{abs} < 8$ bar abs., for the same inlet and outlet boundary conditions are shown in Figure 5.29. This figure shows that the pressure in the expansion zone is higher than the back pressure. From the discussion in Section 5.3.1, this suggests that expansion waves may be present at the nozzle exit.

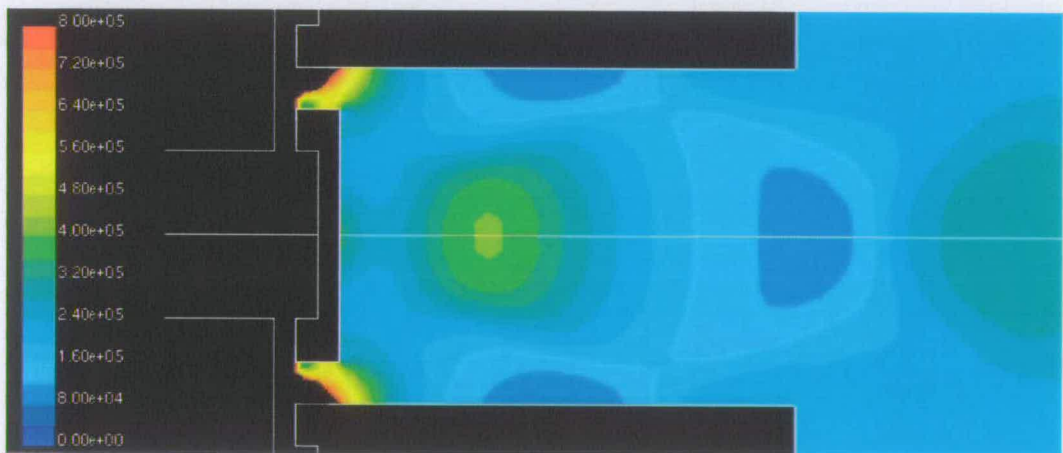


Figure 5.29: Absolute Pressure Plot ($0 < p_{abs} < 8$ bar abs.) for Outlet Pressure Boundary Condition 2.2 bar abs.

To indicate the presence of shock waves in the flow field, a plot of pressure gradient contours, dp/dX , is shown in Figure 5.30. For comparison with similar plots at higher back pressure, the plotted range has been clipped

to $0 < dp/dX < 6e8 \text{ Pa/m}$. The figure shows low gradients of pressure in the expansion zone and at the nozzle exit, indicating that no shock waves are present in this region.

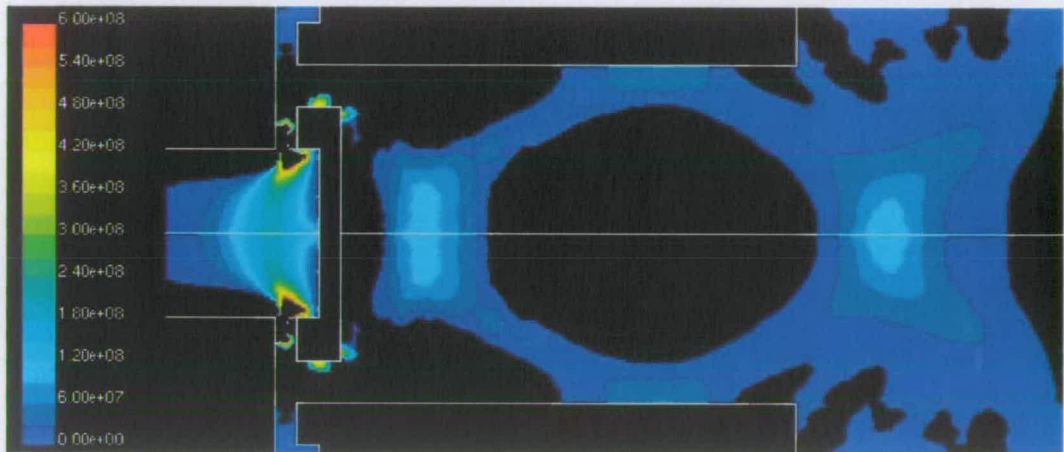


Figure 5.30: Pressure Gradient Plot ($0 < dp/dX < 6e8 \text{ Pa/m}$) for Outlet Pressure Boundary Condition 2.2 bar abs.

The outlet pressure boundary condition was increased to 3.0 bar abs., and Figure 5.31 shows a plot of absolute pressure under this condition. The figure shows that the pressure in the expansion zone and the back pressure are approximately equal.

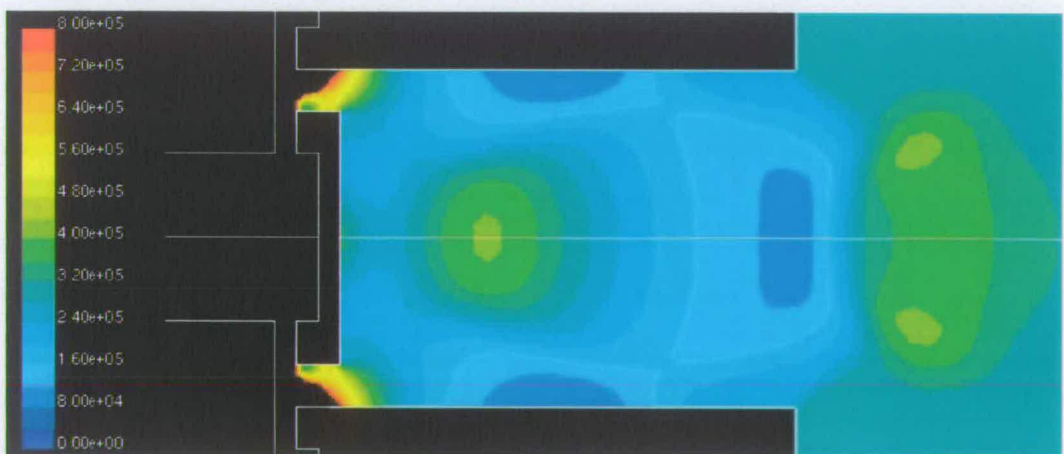


Figure 5.31: Absolute Pressure Plot ($0 < p_{abs} < 8 \text{ bar abs.}$) for Outlet Pressure Boundary Condition 3.0 bar abs.

Figure 5.32 shows a pressure gradient plot under the outlet boundary condition of 3.0 bar abs. This figure shows oblique regions of high pressure gradient at the nozzle exit.

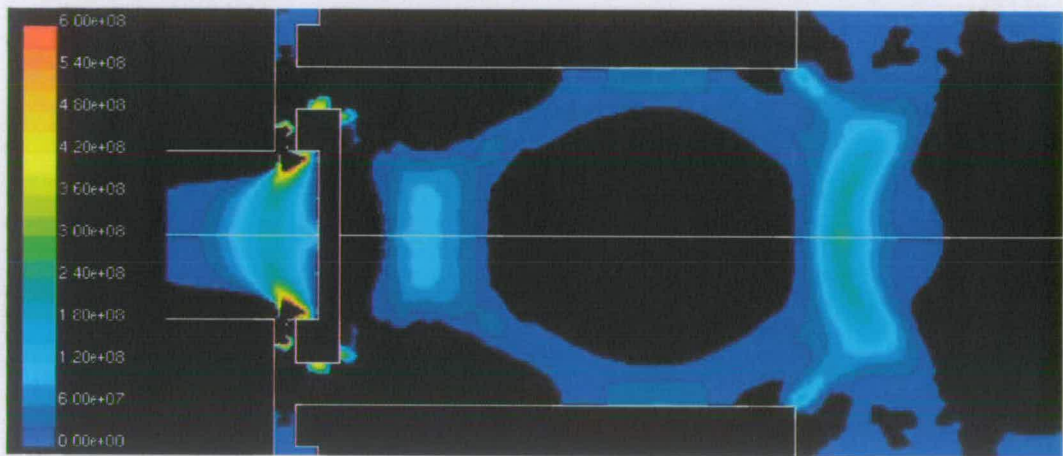


Figure 5.32: Pressure Gradient Plot ($0 < dp/dX < 6e8$ Pa/m) for Outlet Pressure Boundary Condition 3.0 bar abs.

The outlet pressure boundary condition was further increased to 4.0 bar abs., and an absolute pressure plot for this condition is shown in Figure 5.33. This figure shows that the pressure in the expansion zone is lower than the back pressure. According to the theory in Section 5.3.1, under these conditions, oblique shock waves would be expected at the exit.

A pressure gradient plot for the 4.0 bar abs. outlet pressure boundary condition is shown in Figure 5.34. This figure shows clear high pressure gradients at the nozzle exit, indicating the presence of oblique shock waves. A further region of high pressure gradient is shown spanning the width of the nozzle exit between these points, approximately normal to the axis.

Finally, the outlet pressure boundary condition was increased to 5.0 bar abs. Figure 5.35 shows a Mach number plot, clipped to the range $1 < Ma < 3$ for comparison with Figure 5.28. The figure shows that the flow slows to subsonic flow upstream of the nozzle exit.

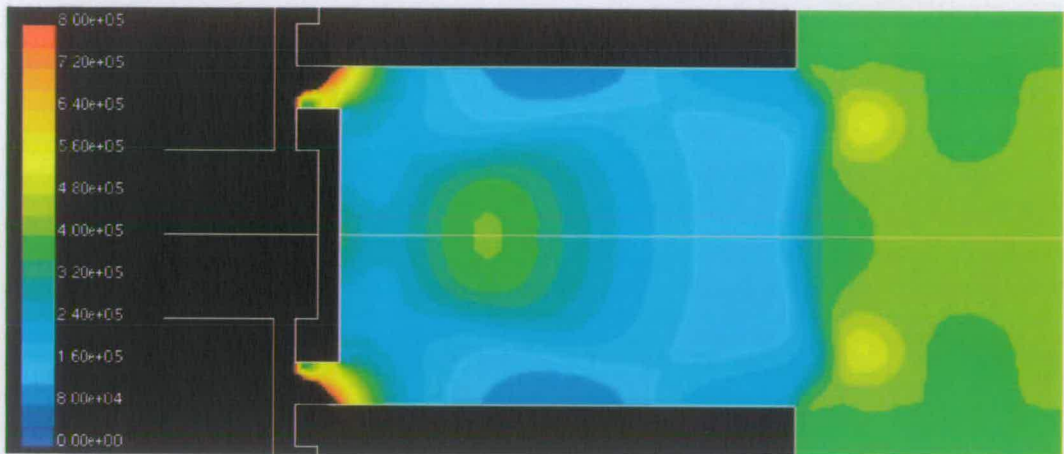


Figure 5.33: Absolute Pressure Plot ($0 < p_{abs} < 8$ bar abs.) for Outlet Pressure Boundary Condition 4.0 bar abs.

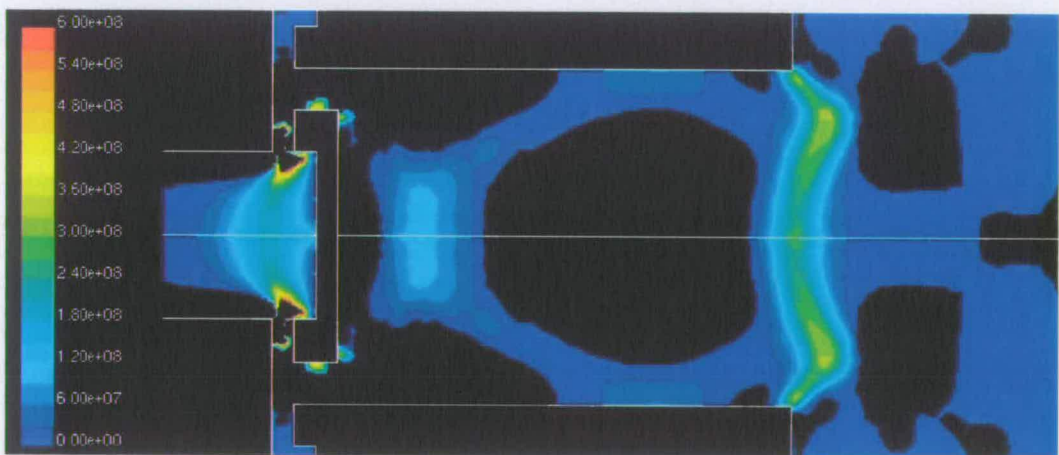


Figure 5.34: Pressure Gradient Plot ($0 < dp/dX < 6e8$ Pa/m) for Outlet Pressure Boundary Condition 4.0 bar abs.

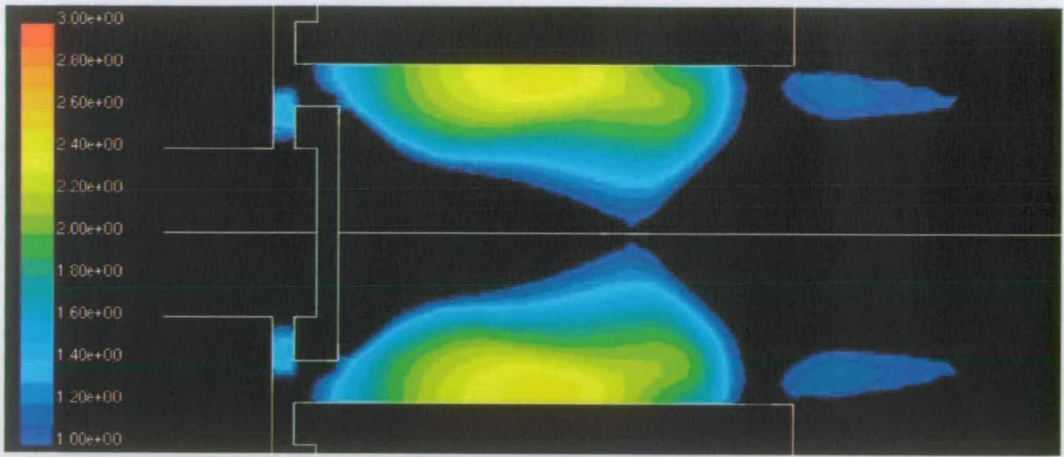


Figure 5.35: Mach Number Plot ($1 < Ma < 3$) for Outlet Pressure Boundary Condition 5.0 bar abs.

Figure 5.36 shows contours of absolute pressure with 5.0 bar abs. outlet pressure, again showing lower pressure in the expansion zone than at the nozzle exit. This would imply that normal shock waves could be present within the expansion zone, and Figure 5.36 indicates this.

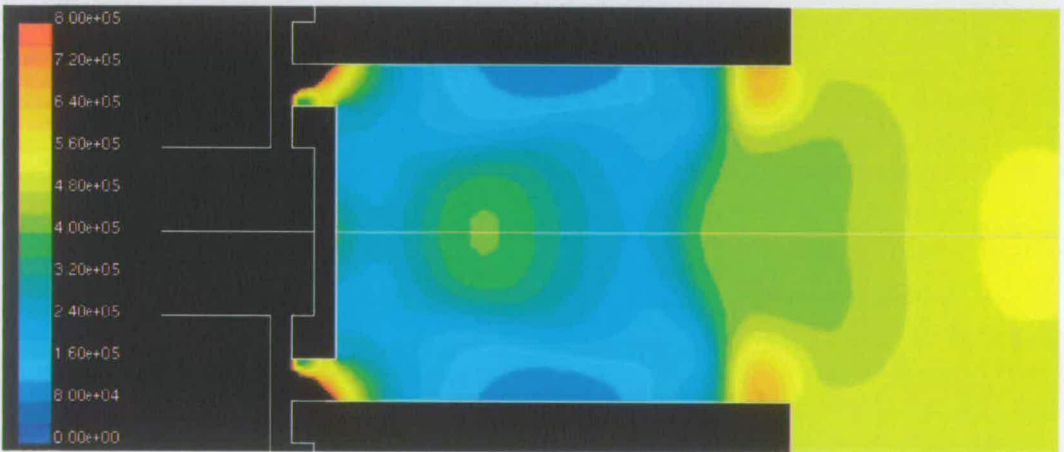


Figure 5.36: Absolute Pressure Plot ($0 < p_{abs} < 8$ bar abs.) for Outlet Pressure Boundary Condition 5.0 bar abs.

Finally, Figure 5.37 shows a pressure gradient plot for the 5.0 bar abs. outlet pressure boundary condition case. The figure clearly shows a high pressure gradient band within the expansion zone, indicating the presence of a normal shock wave.

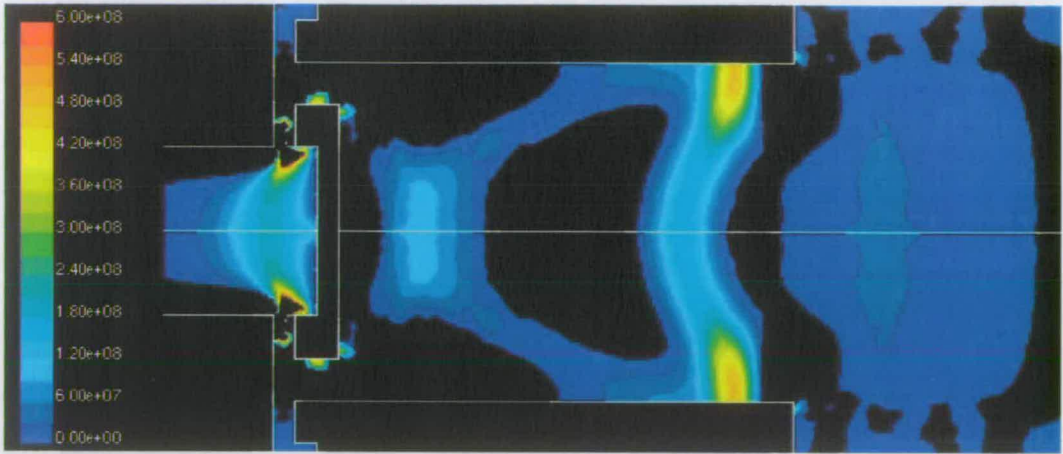


Figure 5.37: Pressure Gradient Plot ($0 < dp/dX < 6e8 \text{ Pa/m}$) for Outlet Pressure Boundary Condition 5.0 bar abs.

5.3.2.2 Quantitative Flow Field Results

The Gambit model geometry described in Section 4.1.3 was tested for similarity to the theory discussed in Section 5.3.1. In Fluent, the inlet pressure boundary condition was defined as 6.18 bar abs., and the outlet pressure (referred to as the downstream pressure p_{ds}) boundary condition as 4.95 bar abs. Thus the initial pressure ratio, p_{ds}/p_0 was 0.80. The downstream pressure was then decreased, such that the ratio p_{ds}/p_0 decreased in increments of 0.05, down to 0.25. After reaching a converged solution at each p_{ds} , a report of mass flux was generated, and the maximum Mach number in the flow field was recorded.

For comparison, expected results were generated according to the theory described in Section 5.3.1. For these results, the geometric flow area 6.28 mm^2 (see Section 4.1.3) was used in the calculation. Modelled and theoretical results of mass flow rate are summarised in Figure 5.38. Also shown are the computed maximum Mach number in the flow field.

Figure 5.38 shows the theoretical results in the subsonic range as the downstream pressure is decreased, down to $p_{ds}/p_0 = 0.527$ according to equa-

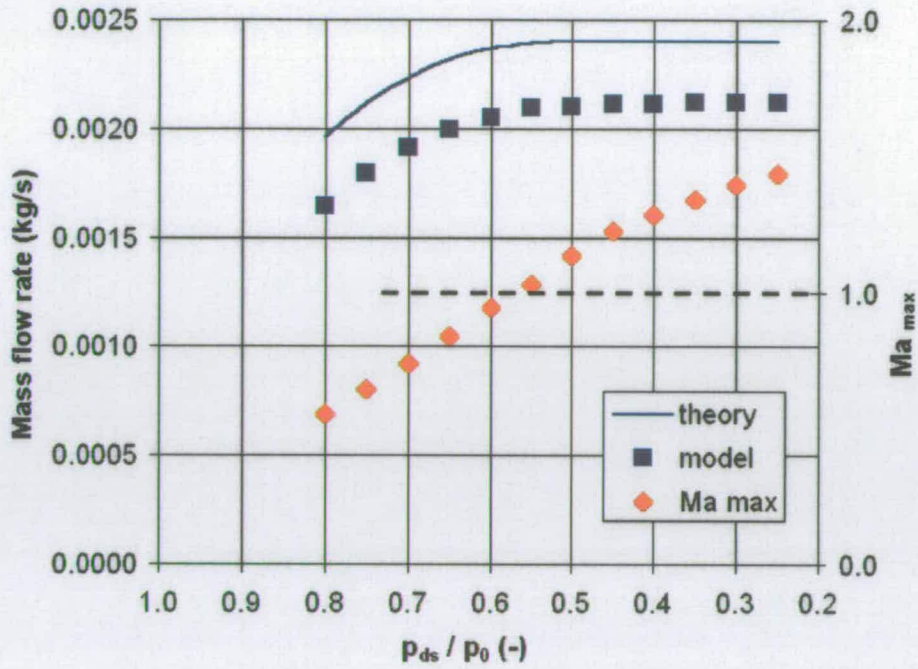


Figure 5.38: Computed and Theoretical Mass Flow Rate vs Pressure Ratio, with Maximum Computed Flow Field Mach Number

tion 5.5, and then remaining constant with a further drop in downstream pressure, according to equation 5.9. The computed mass flux results are generally approximately 13% lower than the theoretical values. This could be attributed to the effective flow area of the modelled flow being lower than the geometric flow area used in the theoretical calculations. Calculating the discharge coefficient, C_d , as the ratio of model mass flow rate to theoretical mass flow rate, C_d is shown to increase from 84% with subsonic flow at $p_{ds}/p_0 = 0.80$ to 88% at $p_{ds}/p_0 = 0.50$.

From the corresponding results of maximum Mach number shown in Figure 5.38, supersonic flow ($Ma < 1$) is shown to occur at $p_{ds}/p_0 < 0.57$. This is higher than the calculated critical pressure ratio for sonic flow, of 0.527. This could be attributed to differences between the outlet pressure boundary condition setting and the pressure at the minimum flow area, or throat pressure, p_T .

The capability of the injector in delivering hydrogen for direct injection applications was assessed by increasing the model boundary conditions to high supply pressure for high mass flow rate. As discussed in Section 3.1.3 and Appendix A the highest design mass flow rate is 23 g/s and the theory suggests that 58 bar supply pressure would be required to deliver hydrogen at this flow rate, given the geometric minimum flow area of 6.3 mm².

It was found that increasing the model inlet pressure boundary condition to 66 bar gave predicted mass flow rate of 23 g/s. This mass flow rate and supply pressure suggest a predicted effective flow area of 5.7 mm², and in turn a discharge coefficient of 90%.

Comparison of the modelled and published mass flow rate results of the annular plate injector (see Section 5.2.2.2) suggest that the model predicted up to 50% lower mass flow rate than the published results. This was thought to be due in part to the model geometry having square edges leading to higher pressure losses in the flow field than could be expected with more rounded edges. This could imply that for the new diaphragm injector design, a fabricated injector with more rounded edges than the model geometry would require lower supply pressure than the 66 bar predicted to deliver the highest design mass flow rate.

5.4 Discussion

By first validating the use of CFD in modelling compressible flows, then comparing a model of the new injector design with results to be expected from theory, further proof of concept has been provided that the design offers a practical solution to hydrogen direct injection. The following sections summarise the key findings of this chapter.

5.4.1 Compressible Flow Model Validation

Published CO₂, N₂ and He mass flow rate data through a Bosch conical seat poppet valve injector were used as a benchmark to assess the effectiveness of CFD in modelling trans-sonic, compressible flows. The published data was used with the compressible flow equation to calculate the Bosch injector effective flow area. The results show that effective flow area reduces by up to 8% for pressures below 6 bar, but remains constant for higher pressures. Also shown is the effect of molecular mass on the effective flow area; helium, with much lower molecular mass than CO₂ (4 g/mol compared to 44 g/mol) showed up to 17% lower effective flow area. This is thought to be due to increased frictional losses associated with higher volume flow rate for helium. It is assumed that hydrogen flow (molecular mass 2 g/mol) would lead to similar effective flow area to the results for helium through the Bosch injector; approximately 1.2 mm².

Mach number plots generated from the CFD model of the approximated geometry of the Bosch injector indicate trans-sonic flow in the region of the minimum flow area at 10 bar supply pressure. Plots of the velocity vectors in the same region clearly show the predicted location of the vena contracta, with recirculation zones in the minimum flow area and also at the expansion zone at the flow exit. Further, a plot of the pressure contours across this region indicates a high pressure gradient in the trans-sonic region and expansion to below atmospheric pressure at the exit.

Comparison of the published and modelled mass flow rate data shows that both indicate a linear increase with supply pressure, as expected for trans-sonic flow. The model mass flow rate data is on average 13% lower than the published Bosch injector data. The effective flow area of the model was calculated from the mass flow rate data as approximately 1.0 mm² (13%

lower than that of the Bosch injector of 1.2 mm^2). The geometric minimum flow area of the model was 1.37 mm^2 , and this implies that the predicted discharge coefficient is 76%.

The lower effective flow area predicted by the CFD model could imply that the geometric minimum flow area of the model is smaller than that of the Bosch injector.

The mass flow rate data used to validate the effectiveness of CFD in modelling compressible flow was for low supply pressure - up to 10 bar - and the effectiveness of compressible flow modelling is only verified in this range of pressure. The effect of higher pressures - up to 58 bar - as modelled in Section 5.3.2, may not be validated by this comparison to empirical data in the range up to 10 bar.

5.4.2 Annular Plate Injector Model

Published data of mass flow rate through the annular plate-type injector described in Section 2.2.1 were used to further validate compressible flow modelling. The data published was dynamic mass flow rate during cyclic operation of the injector. These results showed that average fuel flow rate during the injection period reduces significantly as the pulse width is reduced. This is probably because of the increased significance of flow restriction during the injector-opening and injector-closing periods.

The data were first manipulated to express the static mass flow rate under steady state conditions for two inlet pressure conditions - 5.15 and 6.18 bar abs. These data were then used with the compressible flow equation to calculate the effective flow area of the annular plate injector. These were calculated as 1.4 mm^2 for the 5.15 bar abs. inlet pressure case and 1.8 mm^2

for 6.18 bar abs. inlet pressure; 22% lower effective flow area at the lower inlet pressure.

The published data were compared with data from the CFD model using the model geometry described in Section 4.1.2. A Mach number plot for 6.18 bar abs. inlet pressure indicated trans-sonic flow in the minimum flow area; the plate annulus. Velocity vector plots in the region of the minimum flow area and exit from the valve seat indicate the location of recirculation zones and of the vena contracta. A relatively large recirculation zone is modelled in the recess between the exit from the minimum flow area and the valve seat.

A plot of absolute pressure contours in the inlet pipe suggests a 0.2 bar pressure drop across this region. This is due to the obstruction by the model of the return spring in the inlet pipe. The spring was modelled as a series of concentric rings at the outer edge of the inlet pipe, rather than a helix.

Plotted absolute pressure contours across the minimum flow area and valve seat exit show a high pressure gradient in the trans-sonic region, and expansion to below atmospheric pressure at the exit.

Results of mass flux showed that the model predicts a linear increase in mass flow rate with supply pressure as expected, but up to 50% lower mass flow rate than the published data. This discrepancy could be due in part to higher pressure losses being modelled in the inlet pipe than would be incurred in reality, due to the crudely modelled return spring geometry. Other errors in the model geometry could also contribute. For example, the model geometry has square edges and in reality the edges would be more rounded. More rounded edges would lead to less propensity for flow separation and associated pressure losses. Error in scaling the cross-section drawings to derive dimensions of the injector components could also contribute to the discrepancy in mass flow rate results.

Calculating the effective flow area (1 mm^2) using the compressible flow equation and comparing with the geometric minimum flow area (4.5 mm^2) indicates a predicted discharge coefficient of 22%. This low coefficient is probably due to pressure losses caused by the obstructions in the inlet pipe, and the large recirculation zone between the exit from the minimum flow area and valve seat.

5.4.3 Diaphragm Injector Model

Results from the model of the new diaphragm-type injector design were compared with results derived from compressible flow theory. A case where the inlet and outlet pressures are initially equal, then the inlet pressure is held constant and the outlet pressure is decreased was considered. The theory suggests that for sub-sonic flow (low pressure drop across the injector) the mass flow rate increases to a maximum as the pressure ratio p_T/p_0 decreases. When the critical pressure ratio (0.527 for hydrogen) is reached, the flow becomes sonic at the minimum flow area, and the mass flow rate remains constant for any further drop in downstream pressure.

Also, the flow field pattern at the nozzle exit depends on the difference between the nozzle exit pressure and the back pressure. If the nozzle exit pressure is higher than the back pressure of the gas into which the jet is discharging, expansion waves can form at the exit. If the exit pressure is lower than the back pressure, oblique shock waves can form. If the exit pressure is much lower than the back pressure, normal shock waves can form in the nozzle.

A Mach number plot from the CFD model results of the diaphragm injector indicates the presence of two separate trans-sonic zones with an inlet pressure of 6.18 bar abs. One trans-sonic region occurs at the geometric

minimum flow area as expected, and the second region occurs in the valve seat orifice and extends from there around the edge of the expansion zone. A plot of velocity vectors in this region indicates two *venae contractae* corresponding to the two areas of trans-sonic flow. A plot of absolute pressure indicates the expected high gradient of pressure across the minimum geometric flow area, and expansion to below atmospheric pressure.

To predict the effect of the downstream pressure on the flow pattern, a case of inlet pressure 67 bar was used and the outlet pressure boundary condition was increased from atmospheric pressure. Plots of pressure gradient contours (dp/dX) were used to highlight expansion waves and shock waves. At outlet pressure 2.2 bar abs., absolute pressure contours indicate that the model jet exit pressure would be higher than the back pressure, suggesting the presence of expansion waves. The pressure gradient plot at this condition shows relatively low gradients, with no apparent shock waves or expansion waves present.

For outlet boundary condition of 3.0 bar, the modelled jet exit pressure is lower than the back pressure, suggesting that oblique shock waves could exist. The pressure gradient plot at this condition clearly shows a region of relatively high gradient, oblique to the nozzle exit. This effect becomes accentuated when the outlet pressure boundary condition is increased to 4.0 bar, and this suggests the presence of an oblique shock wave. For outlet pressure boundary condition 5.0 bar, predicted jet exit pressure is much lower than the back pressure, and the pressure gradient plot shows a thin region, approximately normal to the injector axis of symmetry, of high pressure gradient. This suggests the presence of a normal shock wave in this region.

To compare the theoretical and modelled sub- and super-sonic mass flow rate-pressure relationship, the model boundary conditions were initially set such that the pressure ratio was 0.80. The downstream pressure was then

incrementally decreased, recording the mass flow rate and maximum Mach number in the flow field. The theory suggests that the flow would become super-sonic at pressure ratios below 0.527. The model results show super-sonic flow occurring at pressure ratios below 0.57. The pressure ratio is strictly defined as the ratio of throat pressure to inlet pressure, rather than the downstream pressure to inlet pressure as was used to calculate the ratio for the model. This could account for the discrepancy in theoretical and model critical pressure ratios.

As expected from the theory, the model predicts that for sub-sonic flow the mass flow rate increases to a maximum with decreasing pressure ratio. When the flow becomes supersonic the mass flow rate remains constant for any further decrease in pressure ratio.

Comparing theoretical and model mass flow rate indicates a predicted discharge coefficient of the injector geometry of between 84% and 88%, showing the higher coefficient for lower pressure ratios.

For hydrogen delivery at the highest design mass flow rate for direct injection applications (23 g/s), the theory suggests that 58 bar supply pressure would be required, given the design geometry. The CFD model predicts that 66 bar would give 23 g/s mass flow rate and this implies that the effective flow area would be 5.7 mm^2 at this high pressure. The difference between the geometric minimum flow area and modelled effective flow area suggest that the discharge coefficient would be 90%.

The results of the annular plate injector model indicated up to 50% lower mass flow rate at the same supply pressure compared to the published results. This is thought to be partly due to the model geometry having square edges where in reality more rounded edges could be expected. More rounded edges in the flow field would lead to lower propensity to flow separation, and lower pressure losses as a result. This could imply that for a fabricated diaphragm

injector with more rounded edges than the model geometry, lower pressure than 66 bar would be required to deliver the highest design mass flow rate of 23 g/s.

Chapter 6

CONCLUSIONS

The thesis proposed by this work is that a new design of fuel injector, incorporating an annular diaphragm as the open/close device, would, by avoiding sliding contact between components exhibit low wear when metering hydrogen fuel. Further, that it can be shown by simulation that the injector can be designed to withstand cyclic stresses and deliver hydrogen fuel at a rate suitable for direct injection to the cylinder of an IC engine.

This chapter concludes the report by consolidating the key findings of this work that support the thesis. As background to the study, the conclusions to be drawn from the literature base in the field are first given, showing how they have guided the current work and where the shortfalls are in the state-of-the-art. A contribution to knowledge in the field has been given by presenting a normalised comparison of published performance data of hydrogen research engines, and this chapter summarises the key findings of this work.

To address the shortfalls in the state-of-the-art, this chapter describes the key features of the new approach to injector design put forward in this report. The design combines features of two existing injectors to provide a unit capable of high pressure, high flow rate direct injection, while avoiding problems such as leakage and low response time. Proof given in the report

that the injector can be designed in theory to withstand the stress of high fluid pressure and repeated diaphragm deflection is further summarised in this chapter. Further theoretical proof of concept is given that the modelled flow field within the injector geometry forms as expected from theory and validation with empirical data.

Finally, recommendations for how the current work could be developed further are discussed.

6.1 The State of the Art

It has been shown that hydrogen fuel offers an opportunity to provide quality engine load control as opposed to quantity control typical of carburetted petrol engines. Researchers typically employ unthrottled air intake while varying the inducted mass of fuel to control engine load. Due to the low density of hydrogen, a high volume flow rate must be used to induct the required mass of fuel per cycle. For carburetion, MI and PI, there is a relatively long time available for fuel induction so low supply pressures can be used for fuel delivery. For DI, the induction time available is greatly reduced, and high pressures must be used to achieve the required mass flow rate. Sonic flow through the injector must also be achieved so that the mass flow rate is unaffected by changes in the downstream pressure.

For MI and PI fuel induction, it has been found that injectors designed for use with natural gas can provide sufficient flow capabilities when metering hydrogen fuel. However, since hydrogen gas provides very little inherent cooling or lubricating capability compared with natural gas, wear of contacting injector parts has proved to be a serious problem for injector design. Leakage has also been a recurring problem due to hydrogen's low viscosity and molecular size, particularly when high supply pressures are used. Methods to

overcome these problems include providing improved valve seating materials and employing a reed- or diaphragm-valve design to minimise sliding contact.

It has been shown that because of the wide flammability limits and low minimum ignition energy of a hydrogen-air mixture, pre-ignition can easily result from contact between the inducted charge and hot residual gases or burning oil deposits. The principal disadvantage of pre-mixed induction is that the presence of a combustible mix in the inlet manifold leads to conditions where backfire can easily result if pre-ignition occurs before IVC. DI induction eliminates the possibility of backfire by avoiding having fuel in the intake manifold, but pre-ignition can still result, leading to non-optimal engine performance and the risk of knocking combustion. This can be avoided if injection is started close to the scheduled ignition, but this leaves less time for fuel-air mixing.

An advantage of pre-mixed induction over DI is that there is more time available for the fuel and air to form a homogeneous mixture, and this has been shown to improve the cycle efficiency. However, these methods lead to displacement of the intake air by the fuel and volumetric efficiency is reduced significantly. With DI, the full cylinder volume of air can be drawn in for the cycle, maximising the total charge energy and keeping volumetric efficiency high through the range of equivalence ratio compared with pre-mixed fuel induction techniques.

Emissions of NO_x from hydrogen-fuelled engines have been shown to be strongly dependent on equivalence ratio. In the lean range ($\phi < 0.5$) NO_x levels reach negligible levels, but as the mixture approaches stoichiometry, NO_x is much higher (200%) than that of petrol. It has been shown that by injecting very close to TDC and continuing injection during the combustion process, rapid pressure rise and associated high NO_x formation can be avoided.

This report has collated several sets of published performance data of single-cylinder hydrogen engines and presented them on a normalised scale so that direct comparison can be made between the induction methods. This offers a new presentation of the data to the field, and shows that DI offers consistently higher IMEP than MI and carburetion induction methods. This is probably due to the increased volumetric efficiency associated with DI induction.

6.2 New Diaphragm Injector Design

This report has described in detail a new approach to the design of hydrogen direct injectors. The approach is specifically aimed at high pressure DI applications, and addresses the problem of wear associated with hydrogen gas injection. Two particular injectors have been shown in previous work to exhibit low wear when metering hydrogen gas. One used a diaphragm-poppet valve arrangement, the diaphragm separating hydraulic fluid and hydrogen passages, and the other used a reed-annular plate arrangement, the plate acting as the open/close valve. In both cases, sliding contact between parts was minimised or eliminated resulting in low wear.

The new design approach combines features of these two existing injectors. Rather than an annular plate and reed, the design incorporates a steel annular diaphragm as the open/close valve itself. This would lead to fewer parts being used in the construction. A cylindrical solenoid, with the solenoid core bonded to the inside edge of the annular diaphragm provides actuation of the valve. Use of a cylindrical solenoid can provide higher pull force than the clapper type solenoid used in the annular plate injector. Further, the new design houses the return spring outside the fuel inlet tube, avoiding the flow being impeded, as with the annular plate injector.

Because of the need with direct injection to provide high supply pressure, an investigation was carried out into the possibility of incorporating a gas pump in the injector unit. A simplified scenario of single-stage compression of hydrogen gas from 10 to 100 bar was considered and the analysis suggests that a minimum of 3.4% of the fuel energy supplied to the cylinder per cycle would be required to power the compression process. This would correspond to 0.5 bar MEP. Because a pump unit would require careful design to provide durable, leak-free operation, this injector feature was not investigated further.

The relationship between supply pressure and minimum flow area has been discussed, indicating that to achieve the highest design mass flow rate of 23 g/s at least 40 bar inlet pressure would be required if the flow area is to be kept below 10 mm². Practical maximum flow areas would be imposed by ensuring that no gap is wider than the quenching gap of a hydrogen flame, to prevent the flame propagating into the fuel supply and possibly causing heat damage to the injector components. The geometric minimum flow area of the diaphragm injector is 6.3 mm², and from compressible flow theory this suggests that 58 bar supply pressure would be required to provide the highest design mass flow rate for DI applications. To prevent leakage of hydrogen through the closed injector, it has been shown that the return spring force would need to be at least 280 N so that the diaphragm-valve seat contact pressure is greater than the supply pressure.

Using accepted mechanics equations, the relationship between the steel diaphragm dimensions and its deflection and radial bending stress under applied load of 50 N has been investigated. For the design dimensions of outer diameter 26 mm, thickness 0.25 mm and annulus diameter 4 mm, the analysis suggests that the deflection would be 0.67 mm and the maximum radial bending stress would be 420 MPa. Since the required deflection is 0.5 mm this implies that a 50 N force is adequate to provide this. However,

the stress in the diaphragm is greater than the fatigue endurance limit stress and yield strength of some types of steel. Spring steels have been shown to exhibit a fatigue endurance limit of 660 N and this may be a more suitable material. The analysis shows that by increasing the outer diameter of the diaphragm the thickness can be increased while maintaining the required deflection, and this would lead to lower bending stress under the same applied load. However, there is a practical maximum diameter imposed by the need to fit the injector unit into the cylinder head. Hoop stress due to the gas pressure within the injector inlet tube has been calculated as 20 MPa under 100 bar pressure.

The ANSYS DesignSpace CAE package, with imported SolidEdge geometry, was used to first compare FEA results with those using the accepted equations, and then to build a more accurate model of the edge support and load case applied to the diaphragm. An initial model of fixed edge support and 250 N load applied to a diaphragm of thickness 0.5 mm was created. The DesignSpace model indicated a deflection of 0.47 mm; 12% higher than the 0.42 mm calculated using the equations. Modelled bending stress was 23% lower than the calculated stress, at 400 MPa compared to 522 MPa. The geometry used in the model included the solenoid core bonded to the edge of the diaphragm annulus, whereas the calculations assumed an annular line load applied directly at a radius equal to the radius of the diaphragm annulus. This could explain the discrepancies between the FEA model and calculated results.

Rather than having a true fixed edge, the diaphragm in the injector design is clamped around its outer edge between the valve seat component and the cap. This would allow radial deflection of the diaphragm and a second FEA model was created to investigate the effects of this on the deflection and maximum stress. Under an applied load of 250 N, the modelled deflection

was 23% lower than the fixed-edge model at 0.36 mm. Stress was 41% lower at 236 MPa. The model indicated radial deflection of the diaphragm at the edge of the clamp of 7.3 μm .

In summary, this report offers an original approach to hydrogen direct injector design, taking features of two existing injectors to create a new model. Further, the calculated supply pressure, spring force, stress, fatigue and deflection modelling given in this report provide a theoretical proof of concept that the design offers a functional solution to the challenge of hydrogen direct injection. Further concept validation has been provided by investigating the flow characteristics of the design in relation to published empirical data.

6.3 Development of CFD Models

To predict the relationship between supply pressure, mass flow rate, back pressure and exit flow field of the diaphragm injector design, detailed CFD modelling was undertaken. The Gambit preprocessor was used to develop geometry and mesh files for analysis using the Fluent CFD package. All the models developed used axi-symmetric geometry, with triangular mesh schemes. The triangular mesh was preferred, since the quad scheme resulted in poor mass continuity convergence.

Three models were developed, the first based approximately on the geometry of a Bosch conical-seat, poppet valve natural gas injector. For this model, only the region of the conical pintle tip and nozzle exit were modelled. A second model of the reed-annular plate injector was developed. The dimensions for this model were obtained by scaling published drawings to the stated outer diameter of the injector casing. Key geometric differences were that the return spring was modelled as a series of concentric rings rather than a helix around the outer edge of the inlet pipe. Also, in reality the

injector has three arc-shaped flow orifices in the valve seat component, and these were modelled as a single ring-shaped orifice. Finally, the diaphragm injector design geometry was modelled, again with the three arc-shaped flow orifices modelled as one ring-shaped orifice.

When developing the mesh structure of each model, care was taken to bias the mesh so that the greatest cell density was placed in the region of the minimum flow area and the nozzle exit. In these regions, trans-sonic flow can be expected and associated high pressure gradients. A high mesh density in these regions would facilitate accurate modelling of these high pressure gradients, for example across any shock waves that may be present.

In the Fluent environment, each model was defined as single-species, and the properties of hydrogen were assumed. Density was defined as obeying the ideal gas law, rather than the default constant definition, since compressible flow was being modelled. The segregated solver was used rather than the coupled solver as this was found to give a more stable solution process.

For each model, a converged solution was obtained by initially setting the inlet pressure boundary condition very low at 10 Pa, then performing several iterations before increasing the boundary condition again. Increasing the inlet pressure boundary condition incrementally avoided divergence errors, and generally 5,000 to 8,000 iterations were required overall to bring the inlet pressure up to 2 bar.

The computation time per iteration was recorded over the process and compared to the numbers of mesh cells of each model. These results showed a clear computation time penalty with an increase in the number of cells. For example, 5,000 iterations of a model with 6,232 cells took 3.5 hours total computation time, whereas a model with 11,962 cells took 4.5 hours. This excludes the time taken to adjust the boundary conditions over the process.

6.4 CFD Modelling Results

The approximated Bosch poppet-valve injector geometry was first used to assess the effectiveness of CFD in modelling compressible hydrogen flows. Published real data of the mass flow rate of various gases through a Bosch injector was used as a benchmark for the assessment, by comparing the sonic flow mass flow rate-supply pressure relationship between published and modelled results. A comparison of the effective flow area-supply pressure relationship was also made.

The published results indicate that the effective flow area reduces by up to 8% for supply pressure less than 6 bar, and also that 17% lower effective flow area was shown for helium than for CO₂. This is thought to be due to an increase in friction losses with helium flow, associated with lower molecular mass (4 g/mol compared to 44 g/mol for CO₂) and higher volume flow rate. Because hydrogen has a similar molecular mass to helium (2 g/mol) it is assumed that hydrogen flow would exhibit similar effective flow area at 1.2 mm².

A Mach number plot of the modelled flow field indicated trans-sonic flow at 10 bar supply pressure as expected, while velocity vector plots indicated the location of the vena contracta in the minimum flow area and the location of recirculation zones. An absolute pressure plot indicated a high pressure gradient across the trans-sonic region, and expansion to below atmospheric pressure at the nozzle exit.

Comparison of the published and modelled mass flow rate data shows that both sets of results indicate a linear increase with supply pressure. The model predicted on average 13% lower mass flow rate than the published data, and therefore 13% lower effective flow area at 1 mm². This discrepancy is probably due to differences between the approximated model geometry -

particularly the minimum geometric flow area - and the actual geometry of the Bosch injector. The geometric minimum flow area of the model geometry is 1.37 mm^2 , and this suggests the predicted discharge coefficient of 76%.

Further assessment of compressible flow CFD modelling was carried out by modelling the geometry of the existing annular plate injector on which the design of the new diaphragm injector is largely based. In particular, the assessment sought to compare sonic-flow mass flow rate of published and modelled results, and estimate the discharge coefficient of the injector by comparing geometric and effective minimum flow areas.

Two data points of the static mass flow rate (derived from published dynamic mass flow rate data) at two supply pressures were used for comparison to model-predicted data. The published mass flow rate data was used to calculate the effective flow area of the annular plate injector, as 1.8 mm^2 at 5.15 bar abs. inlet pressure, and 22% lower at 1.4 mm^2 at 6.18 bar abs. inlet pressure.

A Mach number plot was first used to confirm sonic flow at the minimum flow area. Velocity vector plots indicated the location of the vena contracta and also indicated relatively large recirculation zones at the exit from the minimum flow area. Absolute pressure plots indicated a pressure drop along the inlet pipe due to flow restriction caused by the model of the return spring.

The model predicted results show a linear increase in mass flow rate with supply pressure as expected, but up to 50% lower mass flow rate than the published data. This discrepancy could be due to differences in the real and model geometry. In particular the model of the return spring as a series of concentric rings could lead to greater pressure loss along the inlet pipe than could be expected through a helical spring. Also, the model does not have the rounded edges that would be expected in machined injector components; square edges would lead to a higher propensity for flow separation and greater

pressure losses as a result. Further, error in scaling the injector dimensions to the stated outside diameter from published cross-section drawings would also contribute to differences between the published and modelled mass flow rate results.

The effective flow area of the model geometry was calculated from mass flow rate results as 1.0 mm^2 . Comparing this to the geometric minimum flow area of 4.5 mm^2 indicates a predicted discharge coefficient of 22%. This low coefficient is probably the result of the pressure losses in the inlet pipe, and the large recirculation zones at the exit from the minimum flow area.

The mass flow rate data used to validate the effectiveness of CFD in modelling compressible flow was for low supply pressure - up to 10 bar - and the effectiveness of compressible flow modelling is only verified in this range of pressure. The effect of higher pressures - up to 58 bar - as modelled for the diaphragm-type injector, may not be validated by this comparison to empirical data in the range up to 10 bar.

Finally, a model of the new diaphragm-type injector design was created, and the modelled flow field was compared with compressible flow theory. The theory suggests that for sonic flow the formation of shock waves depends on the pressure difference between the exit from the minimum flow area and the back pressure into which the jet is discharging. For exit flow higher than the back pressure the flow is under-expanded and expansion waves would be expected to form. For exit flow lower than the back pressure the flow is over-expanded and oblique shock waves may form. If the exit flow is much lower than the back pressure a normal shock wave could form in the nozzle exit region.

The theory further suggests that for sub-sonic flow the mass flow rate increases to a maximum with decreasing ratio of throat pressure, p_T , to supply pressure, p_0 . At the critical pressure ratio - 0.527 for hydrogen - the

flow becomes sonic and the mass flow rate remains constant with any further decrease in pressure ratio.

A modelled flow field Mach number plot at an inlet pressure of 6.18 bar abs. suggests the presence of two trans-sonic regions, one in the geometric minimum flow area as expected, with a further region downstream of this in the valve seat orifice. A velocity vector plot of this region indicates two *venae contractae* corresponding to the two trans-sonic regions. This plot also indicates the location of recirculation zones.

To model the effect of the downstream pressure on the flow field at the nozzle exit, the inlet pressure was set to 67 bar. The outlet pressure boundary condition was then initially increased to 2.2 bar. At these conditions, an absolute pressure plot indicated that the nozzle exit pressure would be higher than the back pressure. A plot of pressure gradient in the region was used to highlight the presence of expansion or shock waves, and at these conditions only low fluctuations in pressure gradient were shown.

With the outlet pressure boundary condition increased to 3.0 bar, the model indicated lower nozzle exit pressure than the back pressure. The pressure gradient plot showed clear regions, oblique to the nozzle exit, of high gradient and this suggests the presence of oblique shock waves. At an outlet pressure of 4.0 bar, the effect is accentuated, with higher pressure gradients shown in the same region. When the outlet pressure is increased to 5.0 bar, the pressure gradient plot shows a thin band of high pressure gradient, approximately normal to the injector axis of symmetry, suggesting the presence of a normal shock wave.

To compare the relationship between pressure ratio and sub- and super-sonic mass flow rate, the boundary conditions were initially set such that the pressure ratio was 0.80; sub-sonic flow. The outlet boundary condition was then incrementally decreased while holding the inlet pressure constant,

recording the modelled mass flow rate and maximum Mach number in the flow field at each increment. It was found that the maximum flow field Mach number reached 1 when the pressure ratio reached 0.57. This is higher than the expected critical pressure ratio for super-sonic flow for hydrogen of 0.527. Since the pressure ratio is defined as that of throat pressure rather than downstream pressure to supply pressure this may account for the discrepancy.

As expected from the theory, for sub-sonic flow the mass flow rate increased to a maximum with decreasing pressure ratio. Once the critical pressure ratio was reached, when the flow becomes super-sonic, the modelled mass flow rate remained constant for any further decrease in pressure ratio.

Comparing theoretical mass flow rate calculated from the geometric minimum flow area, with modelled mass flow rate indicated that the discharge coefficient would be between 84-88%, increasing for lower pressure ratio. For hydrogen delivery suitable for direct injection applications, to achieve the highest design mass flow rate of 23 g/s the theory suggests that 58 bar pressure would be required. Increasing the model inlet pressure boundary condition to 66 bar indicated a mass flow rate of 23 g/s, suggesting that the discharge coefficient at these conditions could be 90%.

However, the results of the modelled geometry of the annular plate injector indicated 50% lower mass flow rate than the published results. This is in part due to increased losses in the modelled flow field as a result of non-rounded edges. This would imply that lower supply pressures than 66 bar would be needed for delivery of 23 g/s if the diaphragm-type injector components were machined with rounded edges.

6.5 Recommendations for Continued Work

In previous work, a detailed assessment of safety with the handling of hydrogen has been made. This work identified the key properties of hydrogen gas that lead to safety concerns [2,3]. The primary safety concern with handling hydrogen is of leakage, collection and possible ignition of the gas. The work presented in this report was limited to simulation of the new injector structure and flow field to build a comprehensive design. Fabrication of a prototype injector, based on the design outlined in this report, and testing in a laboratory would provide data of durability and flow characteristics for comparison with the simulated results. To facilitate this, an experiment test bench that ensures safety while handling high pressure hydrogen must first be provided.

Experimentation could first include comparison of stress and deflection under applied load of the injector diaphragm component with the predicted data. Fatigue failure could also be assessed, by applying cyclic loading to the component. A experiment-design issue would be in considering the effect on test equipment of failure of the diaphragm. It should also be noted that exposure to hydrogen can have a considerable effect on the structural properties of steel, and degradation, or 'embrittlement', can occur [59]. This is a particular concern when the material is used to contain the hydrogen under high pressure, where high tensile stresses would be expected. Any structural tests should include consideration of the prolonged exposure to hydrogen.

Since hydrogen must be supplied at high pressure for direct injection, further investigation of the possibility of incorporating a pump in the injector unit could be carried out. Considerations would include what type of pump would provide high efficiency while ensuring leak-free and durable operation.

Other experimentation with a fabricated prototype could include the relationships between mass flow rate, supply pressure and pressure ratio across the injector. These could be compared with the modelled results outlined in this report. Further CFD modelling work could include developing a time-dependent, two-species model of the flow field. This work would indicate the dissipation of the hydrogen jet into the cylinder gases. This is an important factor for direct injection; since injection starts at a point after IVC, there is very little time for the fuel and air to mix to a homogeneous blend compared with manifold injection and carburetion. Poor mixing of the charge leads to high cycle-to-cycle power variation and poor efficiency. CFD modelling coupled with flow imaging of the discharge from a prototype injector would give a useful model of this important feature of injector design.

In previous work, a single-cylinder research engine was extensively tested for performance running on petrol fuel [3]. This work provided a sound benchmark for comparison with engine performance running on hydrogen fuel. A key goal for continuation of the work presented in this report would be to fit a prototype injector into a research engine and run some tests for performance.

Bibliography

- [1] Eisenstein, P, 2003, "Kicking the oil habit", Professional Engineering, **16**, 8, pp 26-27, Institute of Mechanical Engineers.
- [2] Overend, E, 1999, "Hydrogen combustion engines", Internal report, The University of Edinburgh.
- [3] Overend, E, 2000, "Design, Development and Benchmarking of a Hydrogen-Fuelled Engine Test Facility", University of Edinburgh MEng Thesis.
- [4] Das, L, 1990, "Fuel induction techniques for a hydrogen operated engine", Int J Hydrogen Energy, **15**, 11, pp 833-842.
- [5] Billings, R, Hatch, S and DiVacky, R, 1983, "Conversion and testing of hydrogen-powered post office vehicle", Int J Hydrogen Energy, **8**, pp 943-948.
- [6] Lee, J, Kim, Y, Lee, C and Caton, J, 2000, "An investigation of a cause of backfire and its control due to crevice volumes in a hydrogen fueled engine", ASME 2000 Spring Technical Conference, ICE-Vol **34-3**, Paper No 2000-ICE-284.
- [7] Heywood, J, 1988, Internal Combustion Engine Fundamentals, McGraw-Hill Inc.
- [8] Sierens, R and Rosseel, E, 1998, "Backfire mechanism in a carburetted hydrogen fuelled engine", Proc 12th WHEC, **2**, pp 1537-1546.
- [9] Jing-Ding, L, Ying-Qing, L and Tian-Shen, D, 1986, "Improvement on the combustion of a hydrogen fueled engine", Int J Hydrogen Energy, **11**, 10, pp 661-668.
- [10] Swain, M, Pappas, J, Adt, R and Escher, W, 1981, "Hydrogen-fueled automotive engine experimental testing to provide an initial design-data base", SAE Paper 810350.

- [11] Rosseel, E and Sierens, R, 1997, "Knock detection in a hydrogen engine", SAE Paper 970039.
- [12] Mathur, H and Khajuria, P, 1984, "Performance and emission characteristics of hydrogen fueled spark ignition engine", *Int J Hydrogen Energy*, **9**, 8, pp 729-735.
- [13] Mathur, H and Das, L, 1991, "Performance characteristics of a hydrogen fuelled SI engine using timed manifold injection", *Int J Hydrogen Energy*, **16**, 2, pp 115-127.
- [14] MAN, 1996, "MAN hydrogen propulsion system for city busses", *MAN Engine Technology / Advance Development*, Technical Information Issue, 4/96.
- [15] Das, L, Gulati, R and Gupta, P, 2000, "Performance evaluation of a hydrogen-fuelled spark ignition engine using electronically controlled solenoid-actuated injection system", *Int J Hydrogen Energy*, **25**, pp 569-579.
- [16] Swain, M, Schade, G and Swain, M, 1996, "Design and testing of a dedicated hydrogen-fueled engine", SAE Paper 961077.
- [17] Sierens, R and Verhelst, S, 2000, "Experimental study of a hydrogen fueled engine", *ASME 2000 Spring Technical Conference*, **34-3**, Paper No 2000-ICE-285, pp9-16.
- [18] Kabat, D, Stockhausen, W and Szczepanski, J, 2001, "Hydrogen engine fuel injection system development", Ford Motor Company, Technical Report, SRR-2001-0139.
- [19] Barkhimer, R and Wong, H, 1995, "Application of digital, pulse-width-modulated, sonic flow injectors for gaseous fuels", SAE Paper 951912.
- [20] Kabat, D and Heffel, J, 2001, "Durability implications of neat hydrogen under sonic flow conditions on pulse-width modulated implications", Ford Motor Company FRL, Technical Report, SRR-2001-0140.
- [21] Press, R, 2000, "Gaseous Fuel Injector", US Patent and Trademark Office, Patent Number 6,161,783.
- [22] Pashley, N and Stone, R, 1998, "Predictions of liquid fuel injector performance with gaseous fuels", *Proc Instn Mech Engrs*, **212**, D, pp 311-317.
- [23] Mahan, B and Myers, R, 1987, *University Chemistry Fourth Edition*, The Benjamin/Cummings Publishing Company Inc.
- [24] Douglas, J, Gasiorek, J and Swaffield, J, 1995, *Fluid Mechanics Third Edition*, Longman Group Limited.

- [25] Heffel, J, McClanahan, W and Norbeck, J, 1998, "Electronic fuel injection for hydrogen fueled internal combustion engines", SAE Paper 981924.
- [26] Swain, M and Swain, M, 1995, "Elimination of abnormal combustion in a hydrogen-fueled engine", National Renewable Energy Laboratory, TP-425-8196.
- [27] Varde, K and Frame, G, 1984, "A study of combustion and engine performance using electronic hydrogen fuel injection", *Int J Hydrogen Energy*, **9**, 4, pp 327-332.
- [28] Tang, X, Kabat, D, Natkin, R and Stockhausen, W, 2002, "Ford P2000 hydrogen IC engine development", SAE Paper 02P-130.
- [29] Sierens, R and Verhelst, S, 2001, "Influence of the injection parameters on the efficiency and power output of a hydrogen fueled engine", ICE Spring Technical Conference, **1**, 36-1, pp57-64.
- [30] Lynch, F, 1983, "Parallel induction: a simple fuel control method for hydrogen engines", *Int J Hydrogen Energy*, **8**, 9, pp 721-730.
- [31] Lee, S, Yi, H and Kim, E, 1995, "Combustion characteristics of intake port injection type hydrogen fueled engine", *Int J Hydrogen Energy*, **20**, 4, pp 317-322.
- [32] Watson, H, Milkins, E, Martin, W and Edsell, J, 1984, "An Australian hydrogen car", *Proc 5th WHEC*, pp 1549-1562.
- [33] Valdimarsson, P and Arnason, B, 1996, "Design of a pre-chamber for IC engines operating on low pressure hydrogen", *Proc 11th WHEC*, **2**, pp 1569-1578.
- [34] Meier, F, Khler, J, Stolz, W, Bloss, W and Al-Garni, M, 1994, "Cycle-resolved hydrogen flame speed measurements with high speed Schlieren technique in a hydrogen direct injection SI engine", SAE Paper, 942036.
- [35] Binder, K and Withalm, G, 1982, "Mixture formation and combustion in a hydrogen engine using hydrogen storage technology", *Int J Hydrogen Energy*, **7**, 8, pp 651-659.
- [36] Jorach, R, Enderle, C and Decker, R, 1997, "Development of a low-NO_x truck hydrogen engine with high specific power output", *Int J Hydrogen Energy*, **22**, 4, pp 423-427.
- [37] Guo, L, Lu, H and Li, J, 1999, "A hydrogen injection system with solenoid valves for a four-cylinder hydrogen-fuelled engine", *Int J Hydrogen Energy*, **24**, pp377-382.

- [38] Green, R and Glasson, N, 1992, "High-pressure hydrogen injection for internal combustion engines", *Int J Hydrogen Energy*, **17**, 11, pp 895-901.
- [39] Welch, A and Wallace, J, 1990, "Performance characteristics of a hydrogen-fueled diesel engine with ignition assist", SAE Paper 902070.
- [40] Ikegami, M, Miwa, K and Shioji, M, 1982, "A study of hydrogen fuelled compression ignition engines", *Int J Hydrogen Energy*, **7**, 4, pp 341-353.
- [41] Martorano, L and Dini, D, 1983, "Hydrogen injection in two-stroke reciprocating gas engines", *Int J Hydrogen Energy*, **8**, 11/12, pp 935-938.
- [42] Kim, J, Kim, Y, Lee, J and Lee, S, 1995, "Performance characteristics of hydrogen fueled engine with the direct injection and spark ignition system", SAE Paper 952498.
- [43] Varde, K and Frame, G, 1985, "Development of a high-pressure hydrogen injection for SI engine and results of engine behavior", *Int J Hydrogen Energy*, **10**, 11, pp 743-748.
- [44] Rallis, C, Habbitts, S and Van Dijk, R, 1997, "A hydraulically controlled diaphragm-type hydrogen gas injector", *Int J Hydrogen Energy*, **22**, 11, pp 1071-1073.
- [45] Furuhashi, S, 1989, "Hydrogen engine systems for land vehicles", *Int J Hydrogen Energy*, **14**, 12, pp 907-913.
- [46] Glasson, N and Green, R, 1994, "Performance of a spark-ignition engine fuelled with hydrogen using a high-pressure injector", *Int J Hydrogen Energy*, **19**, 11, pp 917-923.
- [47] Koyanagi, K, Hiruma, M, Yamane, K and Furuhashi, S, 1993, "Effect of hydrogen jet on mixture formation in a high-pressure injection hydrogen fueled engine with spark ignition", SAE Paper 931811.
- [48] Koyanagi, K, Hiruma, M, Hashimoto, H, Yamane, K and Furuhashi, S, 1993, "Low NO_x emission automobile hydrogen engine by means of dual mixture formation", SAE Paper 930757.
- [49] Yi, H, Lee, S and Kim, E, 1996, "Performance evaluation and emission characteristics of in-cylinder injection type hydrogen fueled engine", *Int J Hydrogen Energy*, **21**, 7, pp 617-624.
- [50] Furuhashi, S and Fukuma, T, 1986, "High output power hydrogen engine with high pressure fuel injection, hot surface ignition and turbocharging", *Int J Hydrogen Energy*, **11**, 6, pp 399-407.
- [51] Billings, E, 1983, "Advances in hydrogen engine conversion technology", *Int J Hydrogen Energy*, **8**, 11/12, pp 939-942.

- [52] Giles, W, 1966, "Fundamentals of valve design and material selection", SAE Paper 660471.
- [53] Eastop, T and McConkey, A, 1993, Applied Thermodynamics for Engineering Technologists, Longman Group Limited.
- [54] Roark, R, 1989, Roark's Formulas for Stress and Strain 6th Edition, McGrawHill.
- [55] Beer, F and Johnston, E, 1992, Mechanics of Materials 2nd Edition, McGraw Hill.
- [56] Lee, C, Lee, K, Li, D, Yoo, S and Nam, W, 1997, "Microstructural influence on fatigue properties of a high-strength spring steel", Materials Science and Engineering A241, **30-37**, Elsevier Science.
- [57] Fluent Inc., 1998, "Fluent 5 User's Guide", Fluent Inc.
- [58] Zhou, B, Bouak, F, Fleck, B and Gauthier, J, 2000, "Comparison of turbulence models for swirling effects on ejector performances", Canadian Aeronautics and Space Journal, 46(4), December.
- [59] Das, L, 1991, "Safety aspects of a hydrogen-fuelled engine system development", Int J Hydrogen Energy, **16**, pp 619-624.

Appendix A

INJECTOR MASS FLOW REQUIREMENT FOR DI

To calculate the mass flow requirements of the hydrogen direct injector design, some parameters were first defined for a 'worst case' engine operating condition. The 'worst case' condition would be for injection over a short crank angle duration, and at a high engine speed. The parameters assumed for the case are summarised in Table A.1. Gas properties are also given in Table A.1 that are used in the analysis that follows.

For stoichiometric operation, the mass of hydrogen required per cycle is related to the volume of air drawn into the cylinder. For a hydrogen and oxygen mix, the stoichiometric combustion equation, expressed per mole of fuel is



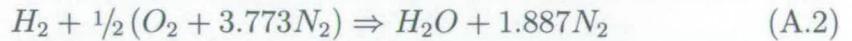
The molar fractions of nitrogen and oxygen in atmospheric air need to be found to express the stoichiometric combustion equation for a hydrogen and air mix. Since 1 kmol of any perfect gas occupies the same volume as

Quantity and units	Value
Top engine speed (RPM)	6000
Minimum injection duration ($^{\circ}\text{CA}$)	30
Equivalence ratio, ϕ (-)	1
Swept volume, V_s (m^3)	0.507e-3
Density of NTP air, ρ_{air} (kg/m^3)	1.293
Volume fraction of O_2 in air (%)	20.95
Volume fraction of atmospheric nitrogen in air (%)	79.05
Molecular weight of H_2 , \tilde{m}_{H_2} (g/mol)	2.016
Molecular weight of atmospheric air, \tilde{m}_{air} (g/mol)	28.96
Molecular weight of H_2O , $\tilde{m}_{\text{H}_2\text{O}}$ (g/mol)	18.02
Molecular weight of N_2 , \tilde{m}_{N_2} (g/mol)	28.16
Ratio of specific heats of H_2 , γ_{H_2} (-)	1.41
Gas constant of H_2 , R_{H_2} ($\text{J}/\text{kg}\cdot\text{K}$)	4121
Hydrogen gas supply temperature, T_0 (K)	300

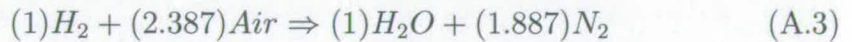
Table A.1: Assumed Engine Operating Condition Data and Gas Properties [24]

any other perfect gas, the molar fraction is simply calculated as the ratio of the volume fractions of N_2 and O_2 - i.e. 3.773 moles N_2 per mole O_2 .

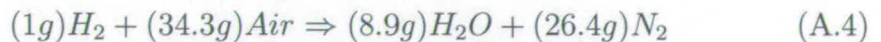
Thus the stoichiometric combustion equation for hydrogen and atmospheric air can be expressed as:



Expressing equation A.2 in numbers of moles of each species:



Multiplying the number of moles of each species by its molecular weight (Table A.1) and scaling to express the equation per gram of H_2 , gives:



Thus 34.3 grams of atmospheric air per gram of H_2 are required for complete combustion. This is the stoichiometric air-fuel ratio - $\sigma_{\text{H}_2} = 34.3$.

It can similarly be shown that for petrol, the stoichiometric air-fuel ratio, $\sigma_{petrol} = 14.6$.

Assuming the volumetric efficiency of the engine is unity, the mass of air drawn into the cylinder is simply calculated from the product of swept volume, V_s (see Table A.1), and the air density, ρ_{air} . From the data in Table A.1, this implies that the mass of air, $m_{air} = 0.66$ g. At an equivalence ratio of $\phi = 1$, and taking $\sigma_{H_2} = 34.3$, this implies that the mass of hydrogen required per cycle, $m_{H_2} = 0.019$ g.

This is the mass of H_2 that must be injected during the injection period for stoichiometric operation. The mass flow rate through the injector during this injection period is simply related to the engine speed (6000 RPM) and the injection duration (30° CA) - i.e. $\dot{m}_{H_2} = 22.9$ g/s.

This is the highest design mass flow rate during the injection period, for the top engine speed and minimum required injection CA duration. For these parameters the injection time duration is at a minimum of 0.83 ms.

From the discussion in Section 5.3.1, equation 5.9 was rearranged to express the required supply pressure in terms of the mass flow rate and injector flow area. Taking the required mass flow rate to be 22.9 g/s, the required supply pressure was calculated for a range of effective flow area. The results are shown in Figure A.1.

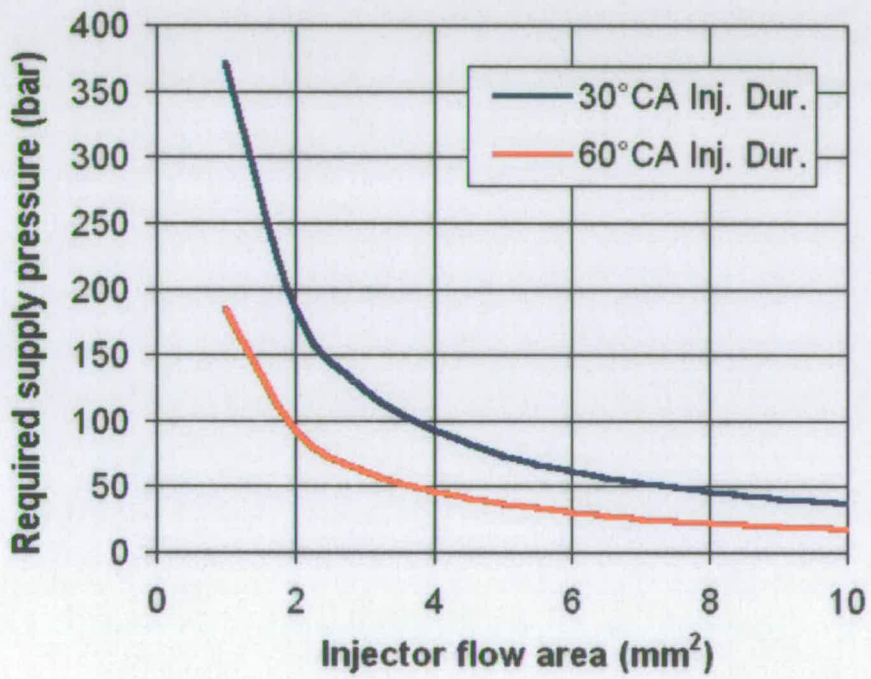


Figure A.1: Required Supply Pressure as a Function of Injector Nozzle Effective Flow Area for Highest Design H₂ Mass Flow Rate (22.9 g/s)

Appendix B

ANNULAR PLATE

DEFLECTION AND STRESS

Roark [54] describes a general loading case of a circular plate with applied uniform annular line load as shown in Figure B.1.

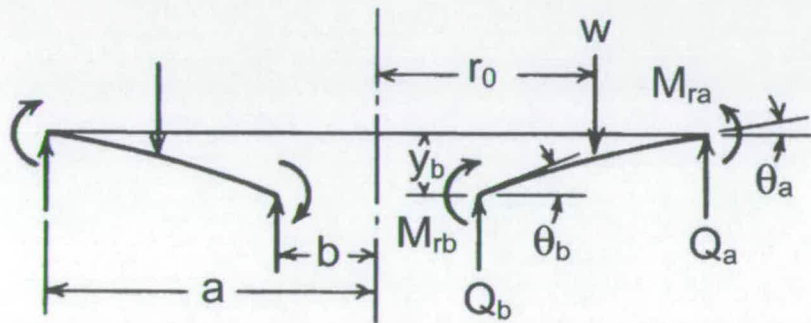


Figure B.1: General Load Case of an Annular Plate [54]

Table B.1 defines the quantities shown in Figure B.1 and those used in the formulae that follow for bending stress and deflection. Values subscripted with 'a' or 'b' apply at the outer or inner edge respectively. Values subscripted 'r' or 't' refer to radial or tangential quantities.

Symbol and units	Quantity
a (m)	Outer plate radius
b (m)	Inner plate radius
t (m)	Plate thickness
r ₀ (m)	Acting radius of annular line force, w
w (N/m)	Annular line force magnitude
y (m)	Deflection
Q (N/m)	Unit shear force (per unit circumferential length)
M (N.m/m)	Unit bending moment
θ (radians)	Change in radial slope
E (N/m ²)	Modulus of elasticity
G (N/m ²)	Modulus of rigidity
ν (-)	Poisson's ratio
D	Plate constant
C _x	Plate constants dependent on a/b
L _x	Loading constants dependent on a/r ₀
σ (N/m ²)	Bending stress

Table B.1: Definition of Symbols

The following equations relate to a specific edge constraint case of a fixed outer edge and free inner edge. The following values are defined for this case; $M_{rb} = 0$ N.m/m; $Q_b = 0$ N/m; $y_a = 0$ m; $\theta_a = 0$ radians.

$$y_b = \frac{-wa^3}{D} \left(\frac{C_1 L_6}{C_4} - L_3 \right) \quad (\text{B.1})$$

$$\theta_b = \frac{wa^2}{DC_4} L_6 \quad (\text{B.2})$$

$$M_{ra} = -wa \left(L_9 - \frac{C_7 L_6}{C_4} \right) \quad (\text{B.3})$$

$$Q_a = \frac{-wr_0}{a} \quad (\text{B.4})$$

Plate constants used in equations B.1 to B.3 are defined as follows:

$$D = \frac{Et^3}{12(1-\nu^2)} \quad (\text{B.5})$$

$$C_1 = \frac{1+\nu}{2} \frac{b}{a} \ln \frac{a}{b} + \frac{1-\nu}{4} \left(\frac{a}{b} - \frac{b}{a} \right) \quad (\text{B.6})$$

$$L_6 = \frac{r_0}{4a} \left[\left(\frac{r_0}{a} \right)^2 - 1 + 2 \ln \frac{a}{r_0} \right] \quad (\text{B.7})$$

$$C_4 = \frac{1}{2} \left[(1+\nu) \frac{b}{a} + (1-\nu) \frac{a}{b} \right] \quad (\text{B.8})$$

$$L_3 = \frac{r_0}{4a} \left\{ \left[\left(\frac{r_0}{a} \right)^2 + 1 \right] \ln \frac{a}{r_0} + \left(\frac{r_0}{a} \right)^2 - 1 \right\} \quad (\text{B.9})$$

$$L_9 = \frac{r_0}{a} \left\{ \frac{1+\nu}{2} \ln \frac{a}{r_0} + \frac{1-\nu}{4} \left[1 - \left(\frac{r_0}{a} \right)^2 \right] \right\} \quad (\text{B.10})$$

$$C_7 = \frac{1}{2} (1-\nu^2) \left(\frac{a}{b} - \frac{b}{a} \right) \quad (\text{B.11})$$

Radial and tangential bending stresses can be calculated using moment values M_r and M_t respectively with equation B.12:

$$\sigma = \frac{6M}{t^2} \quad (\text{B.12})$$

Finally, Poisson's ratio is a function of the modulus of elasticity and modulus of rigidity:

$$\nu = \frac{E}{2G} - 1 \quad (\text{B.13})$$

Appendix C

DIAPHRAGM INJECTOR DESIGN DRAWINGS

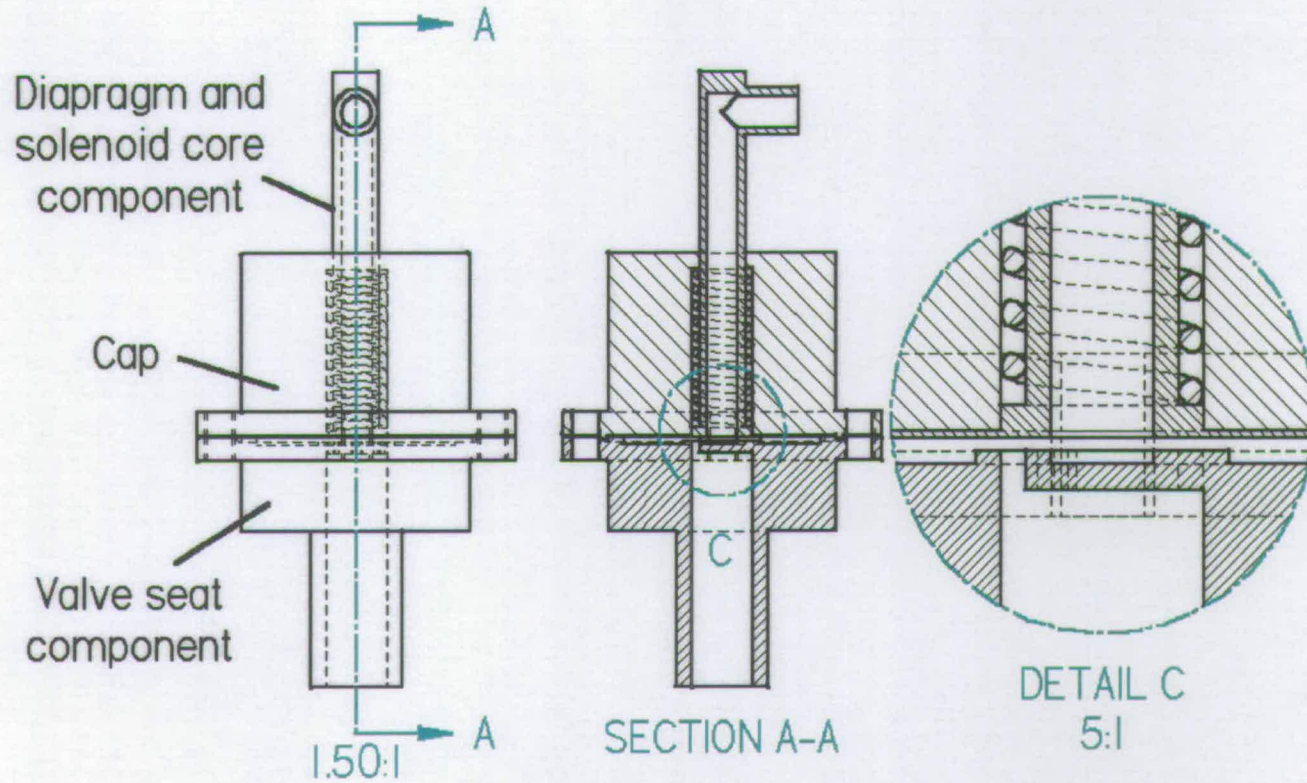


Figure C.1: Injector assembly

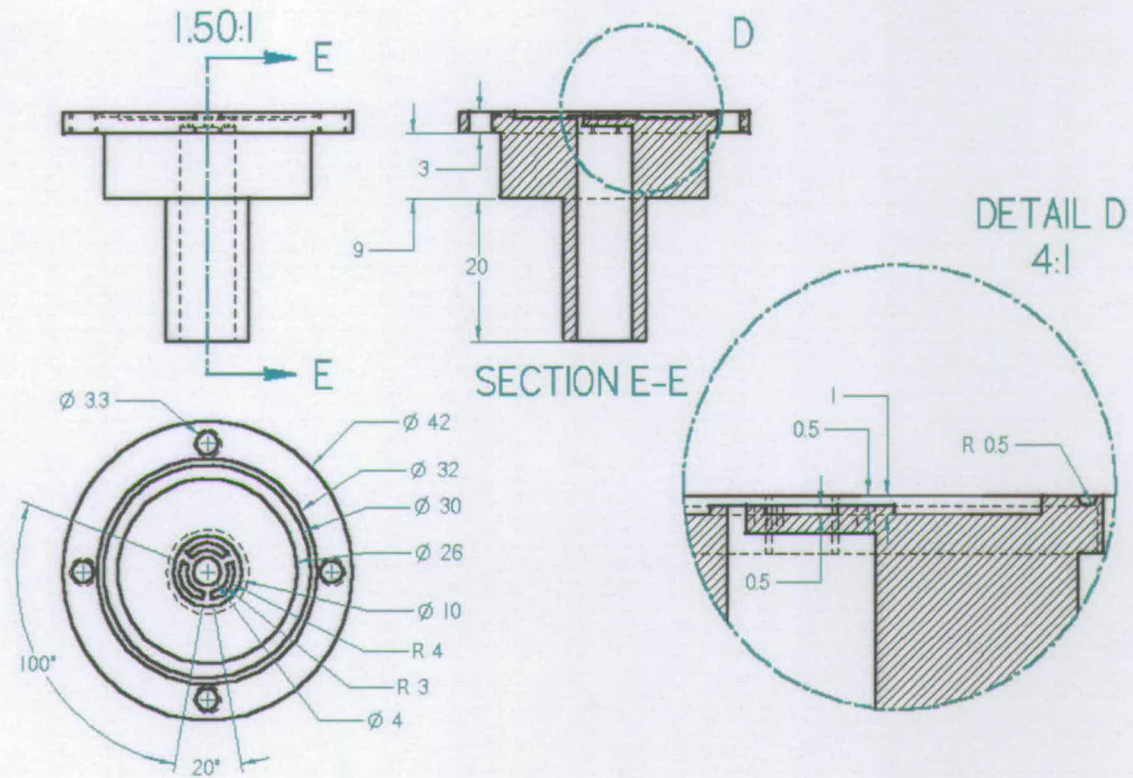


Figure C.2: Injector Valve Seat Component (Dimensions in mm)

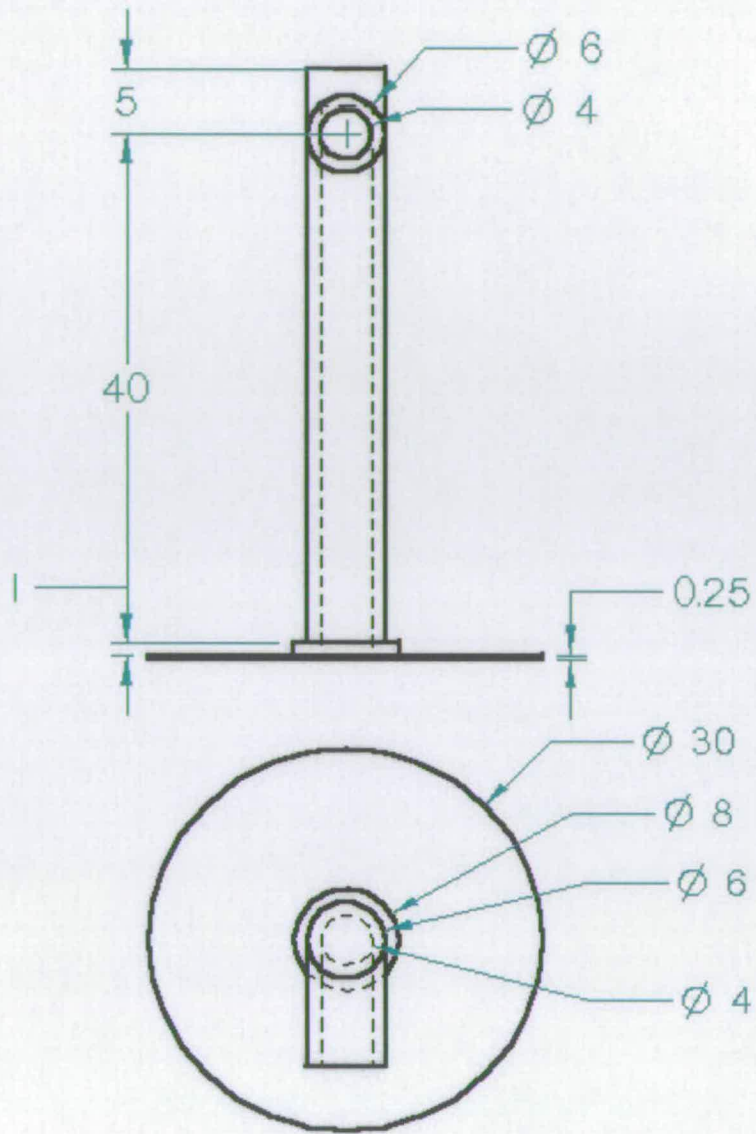


Figure C.3: Injector Diaphragm Component (Dimensions in mm)